ASSESSMENT OF THE KINETICS OF LOCAL PLASTIC DEFORMATION OF Zr-2.5%Nb CANDU PRESSURE TUBE MATERIAL

(Spine title: Local plastic deformation of Zr-2.5%Nb pressure tube material)

(Thesis format: Integrated Article)

by

Bipasha Bose

Graduate Program in Mechanical and Materials Engineering

A thesis submitted in partial fulfillment
of the requirements for the degree of
Doctor of Philosophy

The School of Graduate and Postdoctoral Studies
The University of Western Ontario
London, Ontario, Canada

© Bipasha Bose 2012

THE UNIVERSITY OF WESTERN ONTARIO
School of Graduate and Postdoctoral Studies

CERTIFICATE OF EXAMINATION

Supervisor

_____
Dr. Robert J. Klassen

Supervisory Committee

_____
Dr. J. T. Wood

_____
Dr. Andy X. Sun

Examiners

_____
Dr. Andy X. Sun

_____
Dr. Jun Yang

_____
Dr. Paul A. Charpentier

_____
Dr. Malcolm Griffiths

The thesis by

Bipasha Bose

entitled:

Assessment of the Kinetics of Local Plastic Deformation of Zr-2.5%Nb CANDU Pressure Tube Material

is accepted in partial fulfillment of the
requirements for the degree of
Doctor of Philosophy

_____
Date

_____
Chair of the Thesis Examination Board

Abstract

Constant-load pyramidal indentation creep tests and high precision micro-indentation strain rate change tests were performed to assess the effect of indentation depth, irradiation damage and temperature on the mechanical anisotropy and local plastic deformation parameters of the Zr-2.5%Nb CANDU pressure tube material. Polished samples aligned normal to the transverse (TN), axial (AN) and radial (RN) directions of the pressure tube were irradiated with 8.5 MeV Zr^+ ions to simulate the effect of neutron irradiation. Constant-load pyramidal indentation creep tests performed at 25ºC show that the average indentation stress, $\sigma_{ind_{t=0}}$, increases with decreasing indentation depth and increasing levels of irradiation. The ratio of $\sigma_{ind_{t=0}}$ on the TN plane relative to that on the AN and RN planes was 1.3 and 1.2 respectively before irradiation which reduced to 1.04 and 1.08 respectively after irradiation indicating a decrease in anisotropy as a result of irradiation hardening. The apparent activation energy, ΔG_0, of the obstacles that limit the rate of dislocation glide during indentation creep at 25°C does not change with indentation depth and direction but increases with increasing levels of irradiation damage. Samples irradiated at 300°C with 8.5 MeV Zr^+ ions show similar changes in $\sigma_{ind_{t=0}}$, anisotropy and ΔG_0 with increasing levels of irradiation. However the values are lower than those exposed to Zr^+ irradiation at 25°C indicating the effect of concurrent thermal annealing on the accumulation of irradiation damage. Micro-indentation creep tests performed on the non-irradiated samples over the temperature range from 25 to 400°C show that the ratio of $\sigma_{ind_{t=0}}$ in the transverse direction relative to that in the radial and axial directions decreased with increasing temperature. ΔG_0 increases with increasing temperature and is independent of indentation direction. Micro-indentation strain rate change tests show that the inverse apparent activation area of the deformation process followed a linear, Cottrell Stokes type, dependence upon the applied stress. The increase in the apparent activation work indicates that the irradiation induced damage act as strong obstacles to dislocation glide and thus increase both the magnitude and the strain rate sensitivity of the yield stress of the Zr-2.5%Nb alloy at 25°C.

Keywords

Zr^{+} ion irradiation; indentation; creep; strain rate changes; Zr-2.5%Nb CANDU pressure tube ; anisotropy.

Co-Authorship Statement

Chapters 3, 4, 5, and 6 of this thesis are versions of following published articles:

1. **B. Bose** and R. J. Klassen, Effect of irradiation hardening and indentation depth on the kinetics of micro-indentation deformation of Zr-2.5%Nb pressure tube material at 25^{o}C, Journal of Nuclear Materials, Volume 399, Issue 1 (2010), Pages 32-31

2. **B. Bose** and R. J. Klassen, Effect of Zr^{+} ion irradiation on the mechanical anisotropy of Zr-2.5%Nb pressure tube material, Journal of Nuclear Materials, Volume 405, Issue 2 (2010), Pages 138–143

3. **B. Bose** and R. J. Klassen, Assessment of the Effect of Irradiation Temperature on the Mechanical Anisotropy of the Zr^{+} Ion Irradiated Zr-2.5%Nb, Materials Research Society Symposium Proceedings, Volume 1298 (2011), Pages 73-78

4. **B. Bose** and R. J. Klassen, Temperature dependence of the anisotropic deformation of Zr-2.5%Nb pressure tube material during micro-indentation, Journal of Nuclear Materials, Volume 419, Issue 1-3 (2011), Pages 235–240

The research experiments were designed and executed by the candidate. The candidate also performed data analysis, wrote the initial drafts of the manuscripts and revised the final manuscripts. Suggestions for the interpretation of the data and the editing of the reported manuscripts were carried out by Dr. Robert J. Klassen.

A version of Chapter 7 is being prepared for journal submission. The research experiments were designed and performed by the candidate and professor B.J. Diak from Queen's University, Kingston, Ontario. The candidate also performed data analysis, wrote the first draft of the manuscript and revised the final manuscript. Dr. Robert J. Klassen contributed to the interpretation of data and helped in the development of the final version of the manuscript.

Acknowledgments

The work presented in this thesis would not have been possible without the help and cooperation of the people I would like to acknowledge here.

I would start by expressing my deep gratitude to my supervisor Professor Robert J. Klassen for his continuous guidance and immense support throughout my graduate studies at Western. Without him, it would have been impossible for me to accomplish the work I have done so far.

I would also like to thank Professor B.J. Diak of Queen's University, Kingston, Ontario for his help and effort regarding the micro-indentation strain rate change experiments.

Special notes of thanks are due to Mr. B. Leitch of the Atomic Energy of Canada Ltd (Chalk River Laboratories) for providing the Zr-2.5%Nb pressure tube material used in this study, Dr. T. Simpson of Western University's Nanofabrication Laboratory for preparing the TEM foils, Mr. Fred Pearson from Canadian Centre for Electron Microscopy, McMaster University for helping me with the transmission electron microscopy and Mr. Jack Hendrix of Western University's ion implantation facility for sample irradiation.

Last but not the least, I wish to thank the Natural Science and Engineering Research Council of Canada (NSERC) and the University Network of Excellence in Nuclear Engineering (UNENE) who provided financial support for this research.

Dedications

I dedicate this thesis to:

My parents, Biplab Bose and Supta Bose. Their dream and blessings have brought me to the doorstep of this greatest achievement.

My brother Barshan Bose and my parents-in-law Ashok Kanungo and Shila Kanungo for their continuous encouragement throughout my PhD studies.

My husband Mrinmoy Kanungo for always being there for me. This work would not have been possible without his continuous support, patience and encouragement.

My beloved daughter Onusha Bose Kanungo.

Table of Contents

CERTIFICATE OF EXAMINATION ii

Abstract iii

Co-Authorship Statement v

Acknowledgments vi

Dedications vii

Table of Contents viii

List of Tables xiii

List of Figures xiv

Chapter 1 1

1 Introduction 1

1.1 Zr–2.5%Nb pressure tube 1

1.2 Rationale for Research 2

1.3 Objectives 4

1.4 Benefits and Novelties of the Research 5

1.5 Structure of Thesis 7

1.6 References 8

Chapter 2 10

2 Review of the Relevant Literature 10

2.1 Fabrication Process of Zr-2.5%Nb pressure tubes 10

2.2 Zr and HCP Crystal structure 12

2.3 Anisotropy of the Zr–2.5%Nb pressure tube material 15

2.4 Effect of CANDU operating conditions on the properties of Zr–2.5%Nb pressure tube material 17

2.4.1 Irradiation Damage Production 18

2.4.2 Irradiation Hardening 23

2.4.3 Irradiation Growth 24
2.4.4 Thermal Creep 24
2.4.5 Irradiation Creep 30
2.5 Pyramidal Indentation Testing 34
2.5.1 The Pyramidal Indenter 35
2.5.2 The Indentation Creep Test Platform 37
2.5.3 Pyramidal Micro-Indentation Strain Rate Change Tests 43
2.6 Indentation testing of nuclear materials 46
2.7 Ion Irradiation 47
2.8 Conclusions 49
2.9 References 49
Chapter 3 55
3 Effect of ion irradiation and indentation depth on the kinetics of deformation during micro-indentation of Zr-2.5%Nb pressure tube material at 25^{o}C 55
3.1 Introduction 55
3.1.1 Indentation creep tests to simulate creep at scratches 56
3.1.2 Mechanism of creep deformation ahead of scratches in Zr-2.5%Nb pressure tubes 56
3.1.3 Indentation Size Effect 57
3.1.4 Ion irradiation to simulate neutron irradiation 58
3.2 Experimental procedure 58
3.2.1 Material 58
3.2.2 Zr^{+} ion irradiation 59
3.2.3 Micro-indentation creep tests 60
3.2.4 TEM investigations 61
3.3 Results and Discussion 62
3.4 Conclusions 72

3.5 Acknowledgements 74

3.6 References 74

Chapter 4 78

4 Effect of Zr^+ ion irradiation on the mechanical anisotropy of Zr-2.5%Nb pressure tube material 78

4.1 Introduction 78

4.2 Experimental Procedure 80

4.3 Results and Discussion 83

4.3.1 Mechanical anisotropy of the non-irradiated Zr-2.5%Nb 85

4.3.2 Mechanical anisotropy of Zr^+ ion-irradiated Zr-2.5%Nb 89

4.4 Conclusions 95

4.5 Acknowledgements 96

4.6 References 97

Chapter 5 100

5 Assessment of the Effect of Irradiation Temperature on the Mechanical Anisotropy of the Zr^+ Ion Irradiated Zr-2.5%Nb 100

5.1 Introduction 100

5.2 Experiment 101

5.3 Results & Discussion 102

5.4 Conclusions 108

5.5 Acknowledgements 110

5.6 References 110

Chapter 6 113

6 Temperature dependence of the anisotropic deformation of Zr-2.5%Nb pressure tube material during micro-indentation 113

6.1 Introduction 113

6.2 Experimental Procedure 115

6.3 Results 117

6.4 Discussion 120

6.4.1 Temperature dependence of the anisotropy of the initial indentation stress 121

6.4.2 Temperature dependence of the activation energy of indentation deformation 126

6.5 Conclusions 130

6.6 Acknowledgements 132

6.7 References 132

Chapter 7 135

7 Characterizing the deformation kinetics of Zr-2.5%Nb pressure tube material using micro-indentation strain rate change testing 135

7.1 Introduction 135

7.1.1 PSRC micro-indentation testing 136

7.2 Experimental procedure 139

7.2.1 Test material 139

7.2.2 Zr^{+} irradiation 139

7.2.3 PSRC micro-indentation tests 139

7.3 Results and Discussions 140

7.3.1 The strain rate sensitivity of σ_{ind} in the Zr-2.5%Nb alloy 143

7.3.2 Analysis of V' and $\Delta a'$ 145

7.3.3 Effect of indentation depth and Zr^{+} irradiation on the strength of the obstacles that limited dislocation glide during micro-indentation of Zr-2.5%Nb 147

7.4 Conclusions 149

7.5 Acknowledgements 150

7.6 References 150

Chapter 8 153

8 Conclusions and Future Scope 153

8.1 Conclusions 153

8.2 Scope for Future Work 157

Curriculum Vitae 158

List of Tables

Table 2.1: Chemical composition of Zr-2.5% Nb pressure tubes used in CANDU reactors (Adapted after [11]) 11

Table 2.2: Classification of common types of obstacles to dislocation glide according to their strength ΔG_0 [30] 30

Table 3.1: dpa levels at each of the initial indentation depth, h_0 and their corresponding final indentation depths, h_f for the two kinds of irradiated samples 72

Table 4.1: The ratio of $\sigma_{ind_{t=0}}$ on the TN plane relative to $\sigma_{ind_{t=0}}$ on the AN and RN planes before and after irradiation..... 86

Table 5.1: The ratio of $\sigma_{ind_{t=0}}$ on the TN plane relative to that on the AN and RN planes before and after irradiation..... 105

List of Figures

Figure 1.1: Schematic illustration of a CANDU fuel channel indicating the location of the pressure tube 2

Figure 2.1: Zr-Nb Equilibrium Phase diagram 11

Figure 2.2: hcp crystal structure of the α-Zr phase..... 12

Figure 2.3: Atomic arrangements in the hcp crystal structure 13

Figure 2.4: Some Important planes and directions in the hcp system 14

Figure 2.5: Schematic diagram of the orientation of Zr-crystal in 2.5%Nb pressure tube 16

Figure 2.6: The production of point defects by irradiation. (a) An energetic particle collides with one atom of the perfect crystal lattice (b) The atom is displaced to a non-equilibrium interstitial position (I), leaving a vacant lattice site (V) behind. 18

Figure 2.7: Schematic illustration of the collision sequence of the neutron producing the primary knock-on atom (P) which creates vacancies and interstitials 19

Figure 2.8: The final configuration of a cascade of crystal damage resulting from the interaction of one fast neutron with one atom, the primary knock-on atom, within a crystal. The damage cascade consists of a vacancy rich core and interstitial rich shell..... 20

Figure 2.9: Schematic representation of (a) the vacancy loop and (b) the interstitial loop…. 22

Figure 2.10: The change in yield stress as a function of neutron fluence..... 23

Figure 2.11: Schematic diagram of deformation mechanism map for pure Zr. Typically indentation creep occurs at $\tau/\mu \geq 0.01$ 26

Figure 2.12: Profile of resistance force (F) versus distance (x) for barriers opposing dislocation motion..... 28

Figure 2.13: Plastic strain produced by climb-plus-glide mechanism (a) a dislocation (moving left to right) is held up by an obstacle (b) climb has occurred by vacancy absorption and the dislocation raises to a new glide plane continuing deformation 32

Figure 2.14: Schematic illustration of the variation of creep rate with stress in Zr alloys 33

Figure 2.15: Schematic diagram of (a) a Berkovich tip and (b) an impression an indentation made by a Berkovich tip indented on a flat surface. 36

Figure 2.16: Schematic diagram of a NanoTest Platform assembly. 38

Figure 2.17: Schematic illustration of high temperature testing configuration. 39

Figure 2.18: Typical load-displacement curve. During the tests, the indentation load is increased to reach the desired h_0. The indentation load is then held constant for one hour (for room temperature test) or 300 seconds (for high temperature tests). The horizontal part of the curve, between h_0 and h_f, shows the amount of creep that occurs during the constant-load stage of the indentation test..... 40

Figure 2.19: Diagram of a typical indentation depth versus time plot obtained from a constant load indentation test. 41

Figure 2.20: Schematic diagram of a geometrically self-similar pyramidal indenter..... 42

Figure 2.21: Schematic illustration of the step ramp indentation testing method used to obtain instantaneous strain rate changes: (a) the desired inelastic strain rate change; (b) the theoretically predicted stress response to the rate change in (a) 45

Figure 2.22: SRIM outputs (a) collision sequences (b) target displacements..... 48

Figure 3.1: Calculated irradiation damage, in units of displacement per atom (dpa), resulting from 8.5 MeV Zr^+ ions versus depth in the irradiated Zr-2.5%Nb sample. One sample was exposed to a relatively low dosage of Zr^+ ions corresponding to about a maximum of 5 dpa while another group of sample was exposed to a higher dosage corresponding to a maximum of about 30 dpa at a depth of 2.0 to 2.5 μm. 60

Figure 3.2: Schematic illustration of the orientation of a TEM foil extracted, by FIB milling, from an as-crept indentation made in the Zr-2.5%Nb test material. The SEM image shows the extracted foil with the profile of the indentation clearly visible beneath the deposited Pt protective later. 61

Figure 3.3: Typical average indentation stress σ_{ind} versus time plots during the indentation creep tests performed on (a) Non-irradiated and (b) 30 dpa Zr^{+} irradiated Zr-2.5%Nb samples performed at different values of $h_{0.}$ Although the trend is similar for all samples, the indentation stress σ_{ind} values are higher for the irradiated samples. 63

Figure 3.4: Variation in initial indentation stress, i.e. indentation stress at the beginning of creep tests, $\sigma_{ind(t=0)}$ with initial indentation depth, h_0 for three different sample conditions (as received, 5 dpa and 30 dpa). $\sigma_{ind(t=0)}$ decreases with h_0 and increases with irradiation damage. 64

Figure 3.5: Indentation stress at the end of the one hour constant F creep tests $\sigma_{ind_{t=1hr}}$ versus final indentation depth, h_f plot for the three different sample conditions (as received, 5 dpa and 30 dpa). For all cases the 30 dpa Zr^{+} irradiated sample has the highest final indentation stress. The value of $\sigma_{ind_{t=1hr}}$ also decrease with increasing indentation depth..... 65

Figure 3.6: The rate of change of indentation stress, $\partial\sigma_{ind}(t)/\partial t$, i.e the slope of the curves in Figure 3.3, versus σ_{ind} for the three different sample conditions (as received, 5 dpa and 30 dpa). For all cases the shape of the curve is clearly dependent upon the level of ion irradiation and data from tests performed at different indentation depths lie on essentially the same curves. 66

Figure 3.7: TEM image of an as-crept indentation plastic zone in the non-irradiated Zr-2.5%Nb sample. A very high, but inhomogeneous, dislocation distribution exists everywhere in the sample (including far from the indentation). This dislocation distribution is therefore attributed to the 27% cold drawing stage of the pressure tube fabrication. 67

Figure 3.8: TEM image of the as-crept indentation plastic zone in a 30 dpa Zr^{+} irradiated Zr-2.5%Nb sample. The higher magnification inset displays large regions of mottled “salt and

pepper" contrast which was not observed in the non-irradiated sample (Figure 3.7) and is therefore attributed to diffraction contrast resulting from a uniform distribution of small dislocation loops resulting from the Zr^+ ion irradiation. The sizes of the dislocation loops at room temperature are expected to be less than 5nm [31]. 68

Figure 3.9: The activation energy ΔG_0 of the obstacles that limit the rate of indentation creep versus final indentation depth h_f. The error bars represent ± one standard deviation of the measured population (sample size between 7 and 10). ΔG_0 is essentially independent of h_f (within the variability of the measured ΔG_0) however its magnitude increases with increasing Zr^+ irradiation damage. 70

Figure 3.10: The activation energy ΔG_0 of the obstacles that limit the rate of indentation creep versus the calculated dpa at the final indentation depth h_f of each test (Table 4.1). ΔG_0 clearly increases in a nonlinear way with increasing degree of Zr^+ ion irradiation damage. . 71

Figure 4.1: (0001) basal pole figure of the extruded and cold drawn Zr-2.5%Nb CANDU pressure tube used in this study. This pole figure was supplied, along with the pressure tube test material, by the Atomic Energy of Canada Ltd. The letters A, T, and R refer to the Axial, Transverse, and Radial directions of the pressure tube. The quantities F_R, F_T, and F_A refer to the calculated basal pole fraction aligned in the radial, transverse and axial directions respectively. 80

Figure 4.2: Calculated irradiation damage, in units of displacement per atom (dpa), versus depth resulting from irradiation of a Zr-2.5%Nb substrate with 8.5 MeV Zr^+ ions. The samples in this study were exposed to a Zr^+ ion dosage corresponding to about a maximum damage of about 30 dpa at a depth of 2.0 to 2.5 μm. 81

Figure 4.3: Typical average indentation stress σ_{ind} versus time plots from constant-load indentation creep tests performed on the AN plane at different values of h_0 on: (a) non-irradiated, and (b) a Zr^+ ion-irradiated Zr-2.5%Nb. The trends shown in these figures are similar to those shown by the data from indentation tests performed on the RN and TN planes however the magnitude of σ_{ind} is different. 84

Figure 4.4: Variation in $\sigma_{ind(t=0)}$ with initial indentation depth, h_0 , for indentation tests performed on the AN, TN and RN planes of the non-irradiated Zr-2.5%Nb. 85

Figure 4.5: Schematic presentation of the orientation of the hcp unit cell of the majority of the α-phase grains in the Zr-2.5%Nb samples with respect to the indentation direction. The orientation of the prismatic and the pyramidal slip planes is shown. 87

Figure 4.6: The rate of change of indentation stress, $\partial\sigma_{ind}(t)/\partial t$, versus σ_{ind} for non-irradiated AN, TN and RN samples. For all cases data from tests performed at different indentation depths lie on essentially the same curves. However the shape of the TN curve is different from the other two curves indicating an apparent anisotropy in the thermal indentation creep mechanism. 88

Figure 4.7: Variation in $\sigma_{ind(t=0)}$ with initial indentation depth, h_0 for indentation tests performed on the AN, TN and RN planes of the Zr^+ ion-irradiated Zr-2.5%Nb. 89

Figure 4.8: Normalized change in the initial indentation stress $\hat{\sigma}_{ind}$ (Eq 4.3) plotted against the level of Zr^+ ion irradiation damage as expressed by displacements per atoms (dpa) for indentation tests performed on the AN, TN, and RN planes of the Zr-2.5%Nb test material. ..... .90

Figure 4.9: Normalized change in the initial indentation stress $\hat{\sigma}_{ind}$ (Eq. 4.3) plotted against the resolved basal pole fraction aligned in the direction of indentation for indentations made in Zr-2.5%Nb that had levels of Zr^+ ion irradiation damage ranging from 0.2 to 30 dpa. 91

Figure 4.10: The rate of change of indentation stress, $\partial\sigma_{ind}(t)/\partial t$, versus σ_{ind} for Zr^+ ion-irradiated AN, TN and RN samples. For all cases, the data from tests performed at different indentation depths lie on essentially the same curve. The shape of the curve is not significantly dependent upon indentation direction. This indicates the isotropy of the thermal indentation creep of the ion-irradiated material. 92

Figure 4.11: Activation energy ΔG_0 ,normalized with respect to the strain energy (μb^3) of a dislocation, plotted against the level of Zr^+ ion irradiation damage as expressed by

displacements per atoms (dpa) for indentation tests performed on the AN, TN, and RN planes of the Zr-2.5%Nb test material. 95

Figure 5.1: Dependence of the average initial indentation stress $\sigma_{ind(t=0)}$ upon initial indentation depth, h_0 , for tests performed on (a) the AN plane on samples that were either non-irradiated [13] or Zr^+ irradiated at 25°C [13] or 300°C and (b) on the AN, TN and RN planes of the Zr^+ ion-irradiated Zr-2.5%Nb at 300°C..... 104

Figure 5.2: Normalized change in the initial indentation stress $\Delta\hat{\sigma}_{ind}$ plotted against (a) the level of Zr^+ ion irradiation damage (dpa) resulting from Zr^+ irradiation at 25°C [13] and 300°C (b) resolved basal pole fraction aligned in the direction of indentation for indentations made in Zr-2.5%Nb that were Zr^+ ion irradiated at 25°C [13] and 300°C. 106

Figure 5.3: Apparent activation energy ΔG_0, normalized with respect to μb^3, plotted against the level of Zr^+ ion irradiation damage for samples irradiated at 25°C [13] and 300°C. 107

Figure 6.1: Orientation of the test specimens extracted from the Zr-2.5%Nb pressure tube. 116

Figure 6.2: Typical indentation force (*F*) vs. indentation depth (*h*) curves at different test temperature for indentations made on the TN plane of the Zr-2.5%Nb material. 117

Figure 6.3: (a) Indentation depth *h* versus time (*t*) over the 300 second constant-load stage of indentation tests performed on the TN plane of the Zr-2.5%Nb material at 25, 200, 300 and 400°C. (b) Plots of *h* versus *t* for all tests carried out at 400°C on the TN plane. 119

Figure 6.4: Typical decrease in average indentation stress (σ_{ind}) with time (*t*) for the same tests shown in Figure 6.3. 120

Figure 6.5: Initial indentation stress, $\sigma_{ind\,t=0}$, versus temperature for indentation tests performed on the AN, RN, an TN planes of the Zr-2.5%Nb pressure tube material. 122

Figure 6.6: Initial indentation stress ratios, $\sigma_{ind\,t=0}(TN)/\sigma_{ind\,t=0}(AN)$ and $\sigma_{ind\,t=0}(TN)/\sigma_{ind\,t=0}(RN)$ versus temperature. The shape of the curves indicates that the degree

of anisotropy of the flow stress of the Zr-2.5%Nb pressure tube material changes with temperature. 123

Figure 6.7: Previously published uniaxial yield stress data versus temperature for Zr and Zr-Nb alloys. Included in the plot are equivalent yield stress data calculated from the initial indentation stress data shown in Figure 6.6 with the equation $\sigma_{yield} \approx \sigma_{ind_{t=0}} / 3$. 124

Figure 6.8: Increase in the average ΔG_0 with temperature. This plot shows activation energies from previously published tests along with data from this investigation. 128

Figure 6.9: Average ΔG_0 versus the resolved basal pole fraction in the direction of indentation. ΔG_0 is independent of the basal pole fraction except at the highest temperature (400^{o}C) where ΔG_0 is significantly lowered when the basal pole fraction is large. 129

Figure 7.1: Typical indentation force F versus depth h plot from a PSRC micro-indentation test performed, at 25^{o}C, on the RN plane of a non-irradiated Zr-2.5%Nb sample. The small perturbation of the curve at h = 0.5, 1.0, 1.5, 2.0, 2.5, and 3.0 μm indicate where the strain rate changes occurred. 141

Figure 7.2: Average indentation stress σ_{ind} and plastic indentation depth $h_{plastic}$ versus time for a strain rate change performed at h = 1.0 μm on the sample shown in Fig. 7.1. The figure indicates that $h_{plastic}$ does not change appreciably during the strain rate change indicating that the strain rate was changed under essentially constant strain rate conditions. The change in indentation stress $\Delta\sigma_{ind}$ resulting from the factor of ten strain rate change is indicated on the figure. 142

Figure 7.3: Average indentation stress σ_{ind} plotted versus the indentation depth h for the non-irradiated and the Zr^+ irradiated Zr-2.5%Nb material. 143

Figure 7.4: Strain rate sensitivity m of σ_{ind}, determined from the constant microstructure strain rate change data, versus the indentation depth h for the non-irradiated and the Zr^+ irradiated Zr-2.5%Nb material. 144

Figure 7.5: Apparent activation volume V' (Eq. 7.8) versus the indentation depth h for the non-irradiated and the Zr^+ irradiated Zr-2.5%Nb material. 145

Figure 7.6: Haasen plot of the inverse apparent activation area, normalized with respect to the square of the Burgers vector, $b^2/\Delta a$ versus the equivalent indentation shear stress $\tau = \sigma_{ind}/3M$ for the non-irradiated and the Zr^+ irradiated Zr-2.5%Nb material. 147

Figure 7.7: Apparent activation work area $\Delta W'$, normalized with respect to kT, of the micro-indentation deformation process versus the indentation depth h for one indentation test, involving 6 indentation strain rate changes, on the non-irradiated and the Zr^+ irradiated Zr-2.5%Nb material. 148

Chapter 1

1 Introduction

Pressure tubes employed in the CANDU (Canadian Deuterium Uranium) nuclear reactor core are made of Zr-2.5%Nb alloy. Although these pressure tubes have performed satisfactorily during operation, they develop various microstructural changes (defects) due to exposure to different operating conditions, such as high stress, temperature and neutron irradiation. In this research, various micro- and nano-scale pyramidal indentation test techniques were applied to assess the local variations in the mechanical properties of the Zr-2.5%Nb pressure tube material with and without the presence of these microstructural changes.

1.1 Zr–2.5%Nb pressure tube

In CANDU nuclear reactors, cylindrical pressure tubes contain the uranium oxide fuel bundles and the heavy water (D_2O) primary coolant. These pressure tubes are of 6m length, 103.4mm inside diameter and 4.2mm wall thickness, and operate at about 10 MPa internal pressure, at a temperature ranging from about 250°C to about 310°C and in a fast neutron flux of up to about 4×10^{17} $n\cdot m^{-2}\cdot s^{-1}$ [1-3]. The ends of the pressure tubes are roll-joined to stainless steel end fittings. Calandria tubes, made of Zircaloy-2, are located concentric with the pressure tubes and insulate them from the surrounding cold D_2O moderator. Four central spacers supported by the calandria tube provide separation between the two tubes and partially support the pressure tube to prevent sagging (Figure 1.1).

Although the CANDU reactors were originally designed to use steel pressure tubes, the importance of superior neutron economy along with improved corrosion resistance, dimensional stability and strength led towards the development of zirconium alloys to be used as pressure tube material. Zircaloy-2 was the first zirconium alloy to be used as

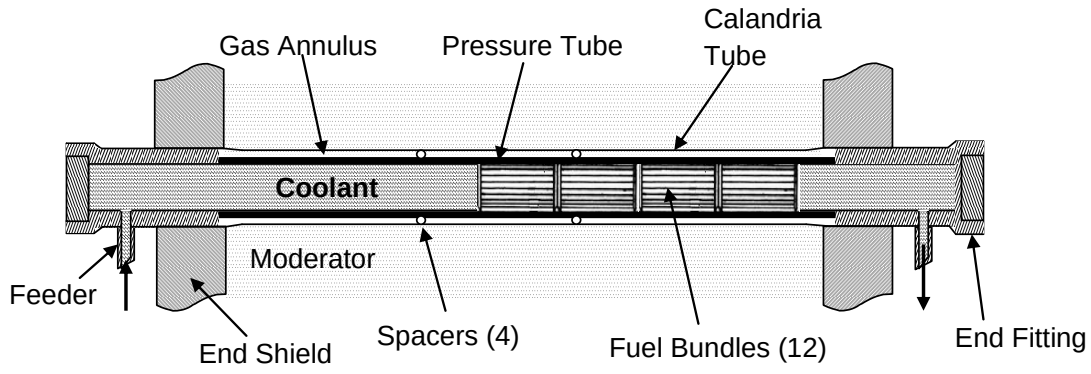

Figure 1.1: Schematic illustration of a CANDU fuel channel indicating the location of the pressure tube (Adapted after Plus et al. [1] and Ross-Ross et al.[2])

pressure tube material. However, further development has shown that the stronger Zr-2.5%Nb pressure tubes not only lowered the neutron absorption of the tube by allowing reduced wall thickness, but also provided lower hydrogen uptake, lower creep rate and made tube fabrication easier [4,5]. Thus, since about 1980, Zr-2.5%Nb pressure tubes have been used for the pressure tube alloy in CANDU nuclear reactors. Chapter 2 of this thesis contains further descriptions regarding these pressure tubes.

1.2 Rationale for Research

The pressure tubes can be subjected to a total fast neutron fluence of about 3×10^{26} $n\cdot m^{-2}$ over their 30 years expected service lifetime in a CANDU reactor core. This high level of neutron irradiation causes the Zr atoms of the pressure tube to undergo about 30 displacements per atom (dpa). These atomic displacements cause crystalline point defects to form and dislocation loops, such as small interstitial and vacancy loops, are produced from the condensation of the point defects [6-12]. These defects act as obstacle to the dislocation glide and thus cause hardening of the pressure tube. Other than irradiation

induced defects, scratches, usually caused by debris from the coolant entrapped between the fuel bundles and the pressure tube wall or by excessive rubbing of fuel bundle bearing pads against the pressure tube wall, can be produced. The local stress ahead of these scratches can be high enough to potentially result in premature failure of the tube [13]. During service, high local stress ahead of the scratches on the inside surface of the pressure tube can cause the precipitation of Zr-hydrides and thus the start of brittle fracture via a delayed hydride cracking process. It is often observed that brittle failure does not occur at these scratches and this puzzles researchers/engineers. They hypothesize that thermal creep in the region of the scratch causes it to blunt and thereby reduce the local stress ahead of the flaw. However, not much is known about the local thermal creep of Zr-2.5%Nb when it is with or without irradiation damage. It is therefore necessary to develop test techniques to predict the local plastic deformation parameters under the high stress state associated with the sharp scratches on the inside surface of these pressure tubes in order to make accurate flaw assessments. Also, a proper understanding for the effect of neutron irradiation hardening on the local thermal creep rate needs to be gained to accurately predict the deformation of this material in irradiated condition.

One characteristic feature of the indentation test results is the indentation size effect i.e. depth-dependence of the indentation hardness of metals below indentation depths of about 10 μm. Although the indentation depth dependence of hardness of relatively isotropic (FCC) metals has been studied widely, it has not been investigated in detail for mechanically anisotropic metals such as the highly textured Zr-2.5%Nb pressure tube alloy.

The mechanical properties of the Zr-2.5%Nb pressure tubes are highly anisotropic i.e., their properties differ in the three principal directions (axial, radial, transverse) of the tube. Generally, the mechanical properties of these tubes are determined by the conventional uniaxial or biaxial loading tests which allow tests only in the axial and transverse (circumferential) directions of the tube. As the thickness of these pressure tubes are only about 4 mm, it is impossible to make conventional uniaxial tensile test specimens aligned parallel to the radial (thickness) direction of the tube. Therefore, it is essential to develop a method for complete characterization of the mechanical anisotropy

of these pressure tubes. From the viewpoint of the nuclear industry, perhaps the most important issue related to the mechanical anisotropy of zirconium alloy pressure tubes is the effect that neutron irradiation has on the degree of the anisotropy. While it is well established that zirconium alloys undergo significant neutron irradiation hardening, the anisotropy of this hardening has not been studied in great detail.

Since the service temperature of CANDU pressure tubes is between 250^{o}C and 310^{o}C, it is also very important to assess the effect of high temperatures on the mechanical anisotropy of the Zr-2.5%Nb pressure tube material both during irradiation and in non-irradiated conditions.

1.3 Objectives

To address the aforementioned research needs, the primary theme of this research is to apply pyramidal indentation test techniques to study the kinetics of local plastic deformation of Zr-2.5%Nb CANDU pressure tube material both in the as-received condition and in conditions similar to those inside a nuclear reactor. The specific research objectives are to:

- Conduct one-hour constant-force pyramidal indentation creep tests at 25^{o}C to investigate:
  - The effect of indentation depth on the mechanism of indentation creep deformation.
  - The effect of Zr^{+} irradiation hardening (as a simulation of neutron irradiation hardening) on the mechanism of indentation creep deformation.
  - The effect of Zr^{+} irradiation damage on the directional anisotropy of the mechanical properties of Zr-2.5%Nb pressure tubes.
  - The effect of temperature during irradiation on the mechanical anisotropy of Zr-2.5%Nb pressure tube material that was irradiated with Zr^{+} ions at 300^{o}C.

- Apply constant-force pyramidal micro-indentation tests to assess the temperature dependence of the anisotropy of the plastic deformation parameters of non-irradiated Zr-2.5%Nb pressure tube material over the temperature range from 25 to 400^{o}C.

- Perform micro-indentation strain rate change tests at 25^{o}C both in irradiated and as-received conditions to determine the strain rate sensitivity of the flow stress of Zr-2.5%Nb pressure tube materials under essentially constant structure conditions and find out the apparent activation area of the dislocation/obstacle interactions that control the plastic indentation deformation process.

1.4 Benefits and Novelties of the Research

The use of pyramidal indentation test techniques to assess the plastic deformation properties of Zr-2.5%Nb pressure tube alloy as described in this research is novel and has potential applications to the solution of various complex problems.

As scratches on the inside surface of CANDU pressure tubes often have geometrical similarities, for example similar depth and sharpness, to the pyramidal indentations, the indentation creep tests can be used to simulate the creep deformation around the scratches. This will provide important information for understanding the fundamentals of the indentation creep process and establishing basic kinetic parameters that can be used in expressions describing the creep rate of material around those scratches. As most of the indentation creep investigations reported so far were performed on relatively isotropic materials, findings from this investigation will provide new information on the deformation parameters of mechanically anisotropic materials, such as the extruded and cold-drawn Zr-2.5%Nb pressure tube alloy used in this research.

The indentation testing technique has high spatial resolution which allows tests on wide ranges of sample dimensions with minimal sample preparation. Thus, this testing technique is potentially very useful to make a complete assessment of the directional anisotropy of the mechanical properties of Zr-2.5%Nb pressure tubes which is not

possible with the conventional uniaxial tests due to the practical difficulty of preparing and testing small specimens cut from the 4 mm thick tubes.

Another novelty of this work is the use of Zr^+ irradiation of the Zr-2.5%Nb pressure tube material to simulate the microstructural damage resulting from neutron irradiation. Previous studies have shown that heavy ion bombardment can be used to create crystallographic damage consisting of dislocation loops similar in size and nature to that produced by neutron irradiation of metals [14, 15]. The benefit of using Zr^+ irradiation for this research is the production of defects without causing significant chemical composition change to the test material which also stays non-radioactive after irradiation. Another benefit is the production of damage in very fast rate. It takes about 1.5 to 2 days for Zr^+ to produce 30dpa of damage to the top several micron thick layer of Zr-2.5%Nb material, whereas neutron irradiation takes about 30 years to produce the same amount of damage. In summary, the benefits of using Zr^+ irradiation are the production of damage at a quicker rate without significantly changing the composition of the base metal and keeping the sample non-radioactive.

This research provides useful information regarding the suitability of indentation test techniques for measuring local mechanical properties of Zr-2.5%Nb CANDU pressure tubes as well as other mechanically anisotropic metals. The test data will provide direct information on the plastic flow properties of Zr-2.5%Nb pressure tube material in the three principal directions of the tube (i.e. the axial, radial and transverse directions) at as-received, irradiated and high temperature conditions that could help in the development of models addressing local stress relaxation at the base of the defects in pressure tubes.

The results of this research can ultimately be used to prescribe more timely pressure tube replacement strategies for CANDU reactors providing a way to improve the economy of the reactor by reducing the possibility for unnecessary pressure tube removal and increase the safety of reactor personnel by limiting unnecessary radiation exposure. In the long term, specialized indentation based testing techniques can be developed based on the testing methodologies applied in this research. These methodologies are potentially

useful to a very wide range of engineering applications, thus benefiting the materials science and engineering community.

1.5 Structure of Thesis

The thesis has been written following the guidelines of the Faculty of Graduate and Postdoctoral Studies at the University of Western Ontario adopting an integrated-article format. It contains 8 chapters, 6 of which contain detailed description of different investigations carried out in this research.

Chapter 2 of this thesis contains a review of relevant published literature on Zr and HCP crystal structures, fabrication, properties and in-service performance of Zr–2.5%Nb pressure tube material, and the theory of deformation mechanisms. It also comprises description of the instrumented indentation test techniques and the testing equipments used for the experiments described in the subsequent chapters. Descriptions of Zr^+ irradiation and indentation based test results of various nuclear materials are also included in this chapter.

Chapter 3 discusses the effect of indentation depth and ion irradiation hardening (as a simulation of neutron irradiation hardening) on the mechanism of indentation creep deformation of the Zr-2.5%Nb pressure tube material. A version this chapter was published in the Journal of Nuclear Materials [16]. Chapter 4 includes investigations regarding the mechanical anisotropy of non-irradiated and Zr^+ ion irradiated pressure tube material. A version of this chapter was also published in the Journal of Nuclear Materials [17] and part of it was presented in NuMat 2010: the Nuclear Materials Conference in Karlsruhe, Germany. In Chapter 5, the effect of irradiation temperature on the mechanical anisotropy of the Zr^+ ion irradiated Zr-2.5%Nb was assessed. Part of this chapter was presented at 2010 MRS Fall Meeting in Boston, MA, USA and was published in Materials Research Society Symposium Proceedings [18]. The effect of temperature on the anisotropic deformation of Zr-2.5%Nb pressure tube material during micro-indentation is described in Chapter 6 and a version of it was published in the

Journal of Nuclear Materials [19]. Chapter 7 describes investigations regarding micro-indentation strain rate change tests. A version of this chapter is being prepared for journal submission. Finally, general and specific conclusions drawn from the research study along with recommendations for future research are presented in Chapter 8.

1.6 References

[1] M.P. Puls, Nuclear Engineering and Design, v. 171 (1997), p. 137

[2] P.A. Ross-Ross, W. Evans, W.J. Langford, Presented at the III Inter-American Conference on Materials Technology, Rio de Janeiro, Brazil, AECL-4262 (August 14-17, 1972), p. 1

[3] W. Evans, P.A. Ross-Ross, J.E. LeSurf, H.E. Thexton, AECL-3982, Paper no. A/CONF.49/A/159 (1971), p. 1

[4] E.F. Ibrahim, B.A. Cheadle, Canadian Metallurgical Quarterly, v. 24 (1985), p. 273

[5] A. Salinas-Rodriguez, M.G. Akben, J.J. Jonas, E.F. Ibrahim, Canadian Metallurgical Quarterly, v. 24 (1985), p. 259

[6] R.A. Holt, M . Griffiths, R.W. Gilbert, Journal of Nuclear Materials, v. 149 (1987), p. 51

[7] M. Griffiths, R.W. Gilbert, V. Fidleris, R.P. Tucker, R.B. Adamson, Journal of Nuclear Materials, v. 150 (1987), p. 159

[8] M. Griffiths, R.W. Gilbert, C.E. Colemab, Journal of Nuclear Materials, v. 159 (1988), p. 405

[9] M. Griffiths, Journal of Nuclear Materials, v. 205 (1993), p. 225

[10] M. Griffiths, Journal of ASTM International, v. 5 (2008), p. 1

[11] E. Kohn, M.G. Wright, AECL, Whiteshell Nuclear Research Establishment, Pinawa, Manitoba, AECL-5810 (1977), p. 1

[12] Griffiths M, Journal of Nuclear Materials, v. 159 (1988), p. 190

[13] N. Christodoulou, P.A. Turner, C.N. Tomé, C.K. Chow, R.J. Klassen, Metallurgical and Materials Transactions A, v. 33A (2002), p. 1103

[14] C. Heintze, C. Recknagel, F. Bergner, M. Hernández-Mayoral, A. Kolitsch, Nucl. Instruments and Methods in Phys. Res. B, v. 267 (2009), p. 1505

[15] X.T. Zu, M. Atzmon, L.M. Wang, L.P. You, F.R. Wan, G.S. Was, R.B. Adamson, J. of ASTM intl., v. 1(2004), p.741

[16] B. Bose, R.J. Klassen, J. of Nucl. Mat., v. 399 (2010), p. 32

[17] B. Bose, R.J. Klassen, J. of Nucl. Mat., v. 405(2010), p. 138

[18] B. Bose, R.J. Klassen, MRS Proceedings, v. 1298 (2011), p. 73

[19] B. Bose, R.J. Klassen, J. of Nucl. Mat., v. 419 (2011), p. 235

Chapter 2

2 Review of the Relevant Literature

This chapter provides a critical overview of the published literature that is relevant to the objectives of this research. The chapter provides useful information on areas related to fabrication and properties of Zr-2.5%Nb pressure tube material, Zr and hcp crystal structures, effects of CANDU reactor operating conditions on the properties of the pressure tubes, mechanisms of time-dependent creep deformation that are active in this pressure tube material, indentation test techniques, and the process of Zr^+ ion irradiation.

2.1 Fabrication Process of Zr-2.5%Nb pressure tubes

The Zr-2.5%Nb pressure tubes are fabricated by extrusion at around 827°C typically with an 11:1 extrusion ratio followed by cold drawing to about 25-27% and then stress relieving at 400°C for 24 hours [1,2]. The extrusion temperature corresponds to the (α+β)-phase field in the Zr-Nb equilibrium phase diagram (Figure 2.1). The resulting grain structure of the extruded tube consists of elongated hexagonal closed packed (hcp) α-zirconium grains supersaturated with Nb (0.5-1 wt%) and networks of metastable body centered cubic (bcc) β-zirconium containing about 20 wt% Nb. Subsequently, the metastable β-phase partially decomposes and forms a metastable Nb-depleted hcp ω-phase precipitate in the remaining Nb enriched (about 40 wt%) bcc β-phase during the stress relief treatment at 400°C [3-9].

Due to the extrusion process the α-grains are found elongated in the axial direction of the tube and thinner in the radial and transverse directions. The average grain size is about usually 0.2, 1 and 5 μm in the radial, hoop and axial directions respectively [2]. A typical chemical composition of the Zr-2.5% Nb pressure tube is given in Table 2.1.

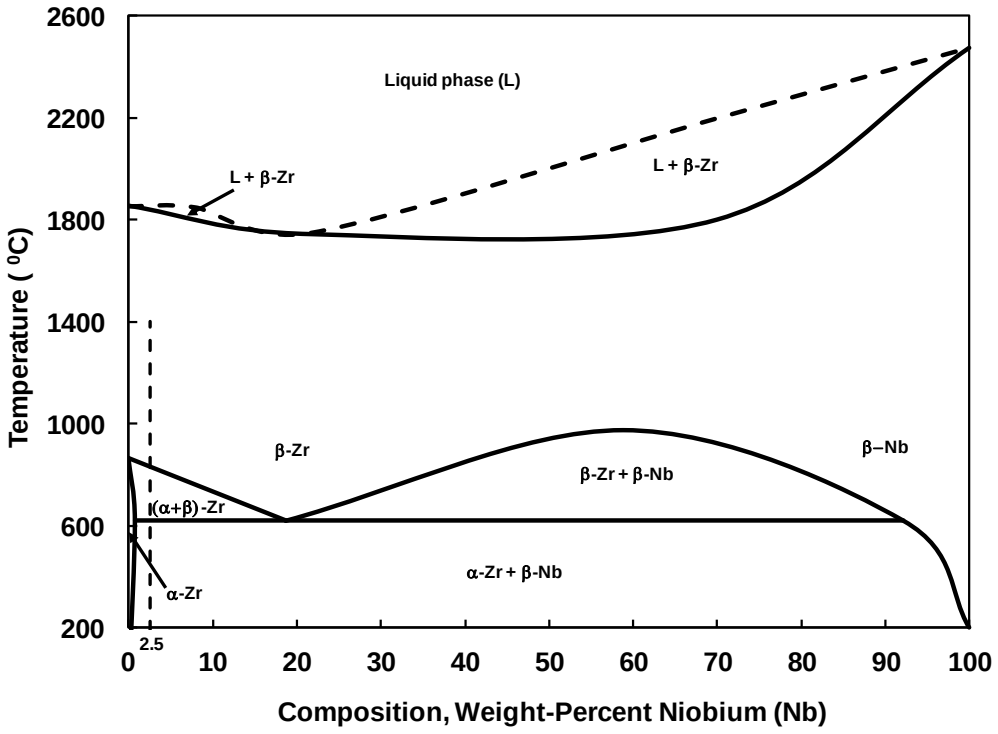

Figure 2.1: Zr-Nb Equilibrium Phase diagram (Adapted after [6, 9, 10]).

Table 2.1: Chemical composition of Zr-2.5% Nb pressure tubes used in CANDU reactors (Adapted after [11])

Element	Composition range of current tubes
Niobium (Nb)	2.4 - 2.8 wt%
Oxygen (O)	900-1300 ppm
Nitrogen (N)	<65 ppm
Hydrogen (H)	<5 ppm
Iron (Fe)	<1300 ppm

2.2 Zr and HCP Crystal structure

Pure zirconium exhibits two distinct types of crystal structures. For temperatures up to 862°C, the equilibrium phase is α-Zr which has a hexagonal close-packed (hcp) crystal structure. For temperature above 862°C up to the melting temperature (1845°C), the material is in the β-Zr phase which has a body-centered cubic (bcc) crystal structure (Figure 2.1). The crystallography of the α-Zr will be discussed in this section since α-Zr is the main constituent of the microstructure of the Zr-2.5%Nb pressure tube material while under normal operating conditions in a CANDU nuclear reactor and, therefore, the mechanical properties of the α-Zr phase have a strong influence on the plasticity and the creep behaviour of the pressure tubes.

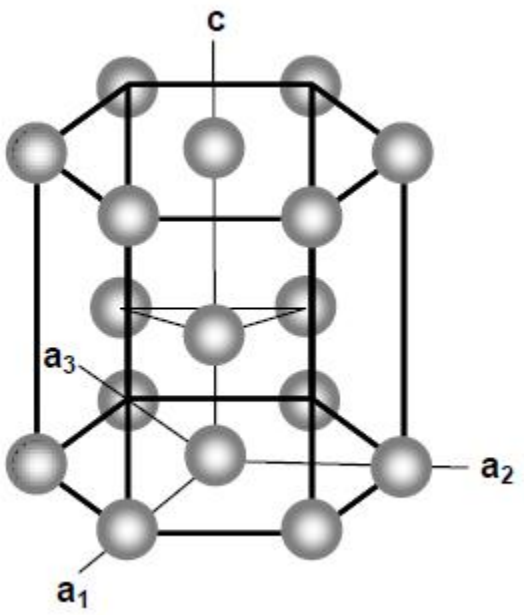

Figure 2.2: hcp crystal structure of the α-Zr phase.

The positions of the atoms in the hcp unit cell of the α-Zr phase are shown in Figure 2.2. The cell geometry is described by four axes. Three of the axes are coplanar with a_1, a_2 and a_3 oriented 120° to one another. The fourth axis, referred to as the c-axis, is perpendicular to the basal plane containing a_1, a_2 and a_3. In the hcp unit cell the lengths

a_1 , a_2 , a_3 are equal. At room temperature the measured values of ‘c’ and ‘a’ for the α-Zr phase of Zr-2.5%Nb are 5.147 and 3.323 Å respectively [12].

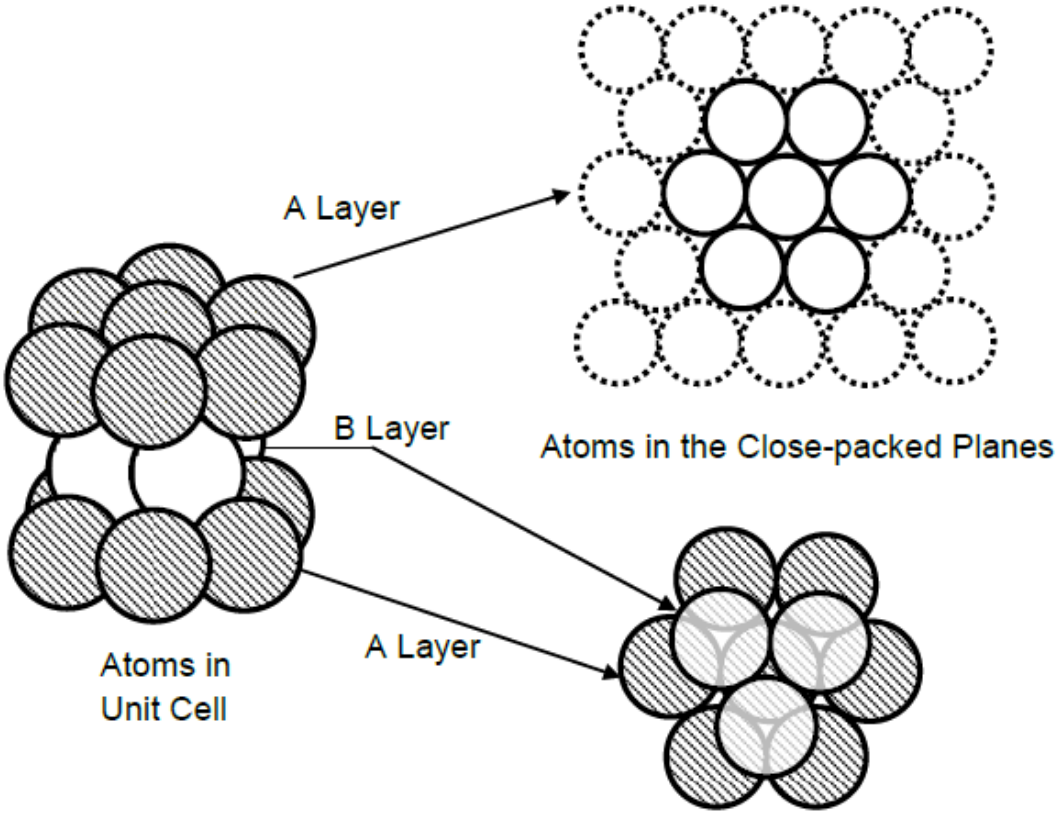

Figure 2.3: Atomic arrangements in the hcp crystal structure (Adapted after [12])

The hcp structure is mechanically anisotropic i.e. the mechanical strength, strain-hardening capacity, creep resistance and ductility are different when the material is loaded along the c-axis than when it is loaded along one of the a-axes. For an ideal hcp structure where the atoms have equal affinity for one another, the ratio c/a would be 1.633. The mechanical anisotropy of Zr is enhanced by a deviation from this ideal ratio c/a. The c/a ratio for Zr is 1.593, which is significantly less than the ideal ratio and this deviation affects the deformation behaviour of Zr.

The stacking sequence of close packed atom planes necessary to create the hcp structure is shown in Figure 2.3. These planes are stacked one on top of another following an A-B-A-B-A… sequence. It is this stacking sequence that give rise to the marked anisotropic properties of the Zr single crystal.

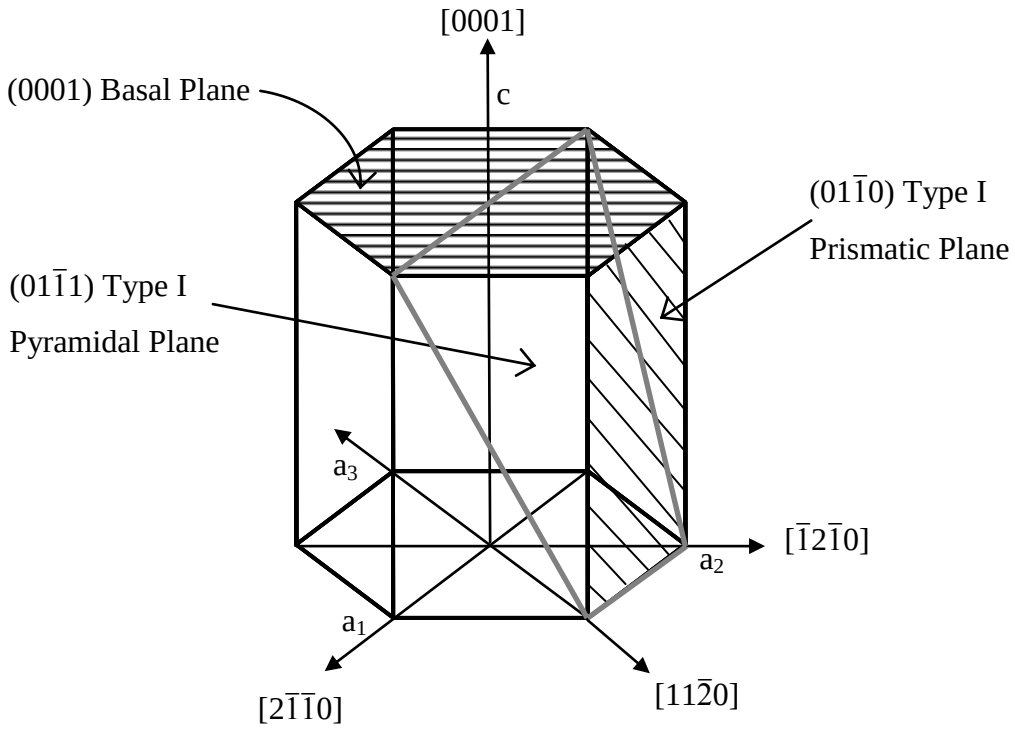

Figure 2.4: Some Important planes and directions in the hcp system

Some of the planes in the hexagonal crystal structure are particularly significant to the plastic deformation process and are given special names according to the {hklm} Miller index notation:

Basal Planes	{0001}
Type I prismatic planes	{10$\bar{1}$0}
Type II prismatic planes	{11$\bar{2}$0}

Type I pyramidal planes $\{10\bar{1}1\}$

Type II pyramidal planes $\{10\bar{2}2\}$

These significant crystal planes, and several significant crystal directions are shown superimposed upon an hcp unit cell in Figure 2.4. According to Miller index notation, planes and directions with common indices are orthogonal.

Since plastic deformation occurs in the Zr-2.5%Nb alloy by the mechanism of dislocation slip upon specific planes, and specific direction on those planes, we can define specific {hklm}<hklm> slip systems that are active. The prismatic slip system $\{10\bar{1}0\}<11\bar{2}0>$ is the dominating slip system in the Zr-2.5%Nb alloy. The limited number of available prismatic slip planes means that other dislocation slip systems, of the basal and pyramidal type, must be also active to accommodate plastic deformation in some loading directions [38]. It has been observed that the active slip system during tension and compression along the a-axes is the prismatic slip system whereas pyramidal slip i.e. $\{10\bar{1}1\}<\bar{1}\bar{1}23>$ slip dominates during tension or compression along c-axis [12, 14-17]. The limited number of slip systems and the asymmetry of the deformation process are both related to the mechanical anisotropy of the Zr-2.5%Nb material.

2.3 Anisotropy of the Zr–2.5%Nb pressure tube material

The mechanical anisotropy displayed by the Zr-2.5%Nb pressure tubes is due both to the inherent anisotropic properties of the hcp crystal structure of zirconium and the strong crystallographic textures that results from the process of tube fabrication [1-3,6,7,13]

As a result of the thermo-mechanical extrusion and cold drawing fabrication process, as described in section 2.1, the majority of the α-phase grains in these pressure tubes are textured with their <1000> c-axis aligned in the circumferential (transverse) direction and the $<10\bar{1}0>$ and $<11\bar{2}0>$ in the axial and the radial (thickness) directions of the tube respectively [4,18] as shown in Figure 2.5.

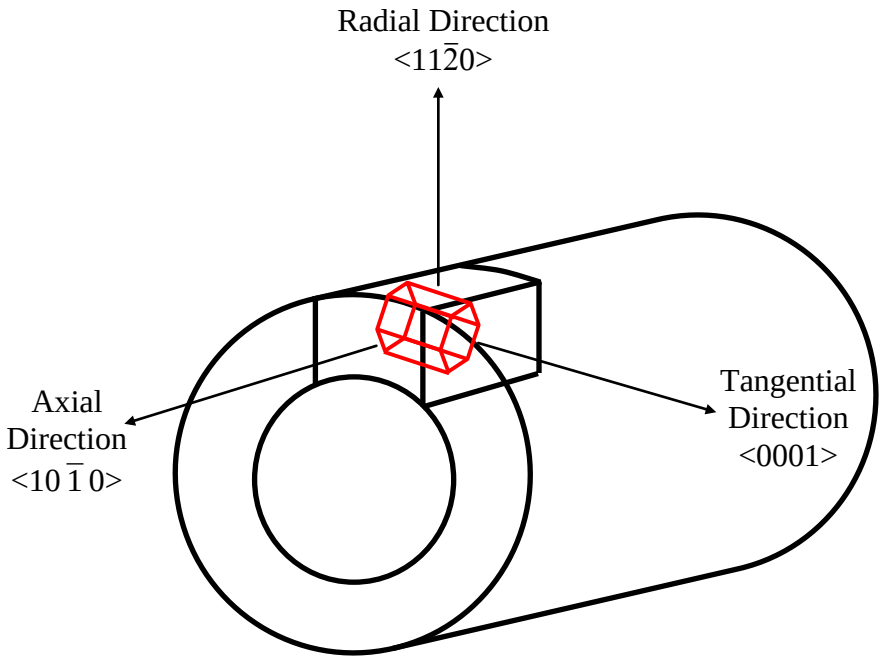

Figure 2.5: Schematic diagram of the orientation of Zr-crystal in 2.5%Nb pressure tube

As indicated in section 2.2, deformation occurs by pyramidal slip along the c-axis. The pyramidal slip plane $\{10\bar{1}1\}$ requires the motion of dislocations with large Burgers vectors, containing both c and a components, we refer to these as (c+a) Burgers vectors. Research has shown that pyramidal slip involving the glide of dislocations with (c+a) Burgers vector requires the application of multiple times higher critical resolved shear stress than that required for prismatic slip of Zr. [15]. Thus, the flow stress of the of Zr–2.5%Nb pressure tube material is highest in the transverse direction of the pressure tube.

This anisotropic behaviour of the pressure tube material also affects the tubes performance inside the nuclear reactor. A description of the response of this material under operating conditions is discussed next.

2.4 Effect of CANDU operating conditions on the properties of Zr–2.5%Nb pressure tube material

During in-reactor operation, the dimension of the CANDU pressure tubes changes due to the effects of temperature, neutron irradiation and stress. The dimensional changes in the pressure tubes during service are [11,19]:

i) Diametral expansion: The diameter of the pressure tube increases with time. This happens mainly due to irradiation creep under the action of the hoop stress resulting from the pressurized D_2O coolant. The contribution from thermal creep and irradiation growth is small at least in the central region of the pressure tube where the neutron flux, and hence the radiation effects, is very large. However, it was found that irradiation growth has a negative component which is beneficial as it tends to decrease the total amount of diametral expansion.

ii) Axial elongation: The pressure tube elongates due to a combination of irradiation creep and irradiation growth. This happens due to the anisotropic crystal structure of Zr and the pronounced crystallographic texture produced during fabrication. The elongation rate increases with accumulated fast neutron fluence.

iii) Sag: The pressure tube undergoes sag mainly by irradiation creep from the weight of the fuel bundles and the heavy water.

iv) Wall thinning: As creep and growth occurs at constant volume, the increase in diameter and length result in a reduction in the wall thickness of the pressure tube.

The dimensional changes of the pressure tube is considered to be the contribution of three mechanisms associated with the neutron irradiation and temperature [11]:

Irradiation growth: The change in shape due to irradiation under zero applied stress at constant volume.

Thermal creep: The change in shape at a constant volume due to the effect of temperature and stress in the absence of a fast neutron flux.

Irradiation creep: The additional change in shape due to irradiation and applied stress at constant volume.

For practical purposes, the total in-reactor deformation rate is often expreesed as the sum of these three terms. Of these three, irradiation growth is considered to be driven by the diffusional anisotropy difference (DAD) which will be described in section 2.4.3. The actual mechanism of irradiation creep and the transition between the thermal creep and irradiation creep are not clearly understood. However, what is known of these mechanisms is described in the following sections.

2.4.1 Irradiation Damage Production

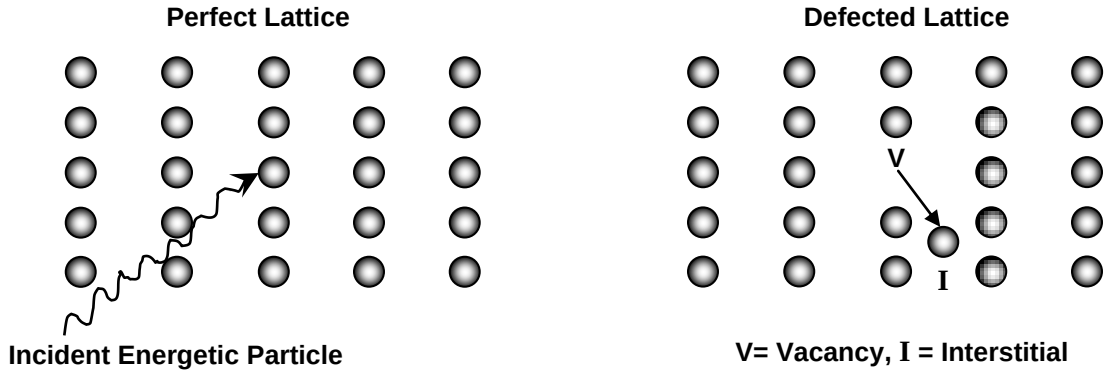

Figure 2.6: The production of point defects by irradiation. (a) An energetic particle collides with one atom of the perfect crystal lattice (b) The atom is displaced to a non-equilibrium interstitial position (I), leaving a vacant lattice site (V) behind. (Adapted after [19])

Fast neutron ($E_{neutron} \geq 1.0$ MeV) irradiation causes atomic displacements to occur in Zr and an irradiation affected microstructure evolves. This microstructure dramatically affects the mechanical properties of the material. Two kinds of crystallographic point defects are created when high energy neutrons interact with, and displace, atoms in a Zr crystal. The displaced atom occupies an interstitial site in the crystal and leaves behind a vacancy (Figure 2.6).

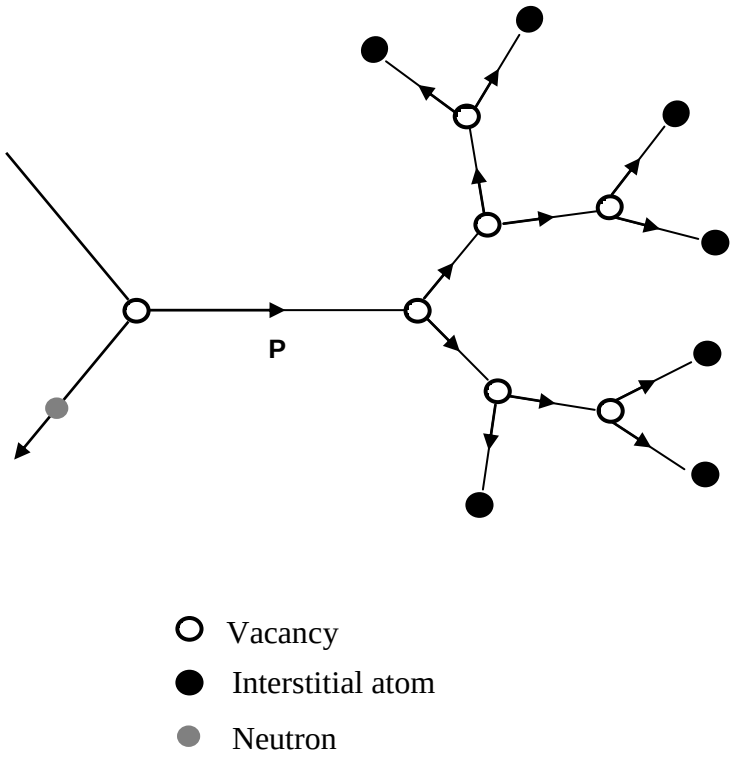

Figure 2.7: Schematic illustration of the collision sequence of the neutron producing the primary knock-on atom (P) which creates vacancies and interstitials (Adapted after [19])

In pressure tubes, a fast neutron is capable of producing a large number of vacancy-interstitial pairs, grouped into high density clusters or cascades. Once an energetic neutron has displaced one Zr atom (the primary knock-on atom), sufficient energy is usually transferred to that atom such that it can interact with other Zr atoms and displaces

many more atoms in a sequential process. Figure 2.7 provides a schematic illustration of such a multi-collision process.

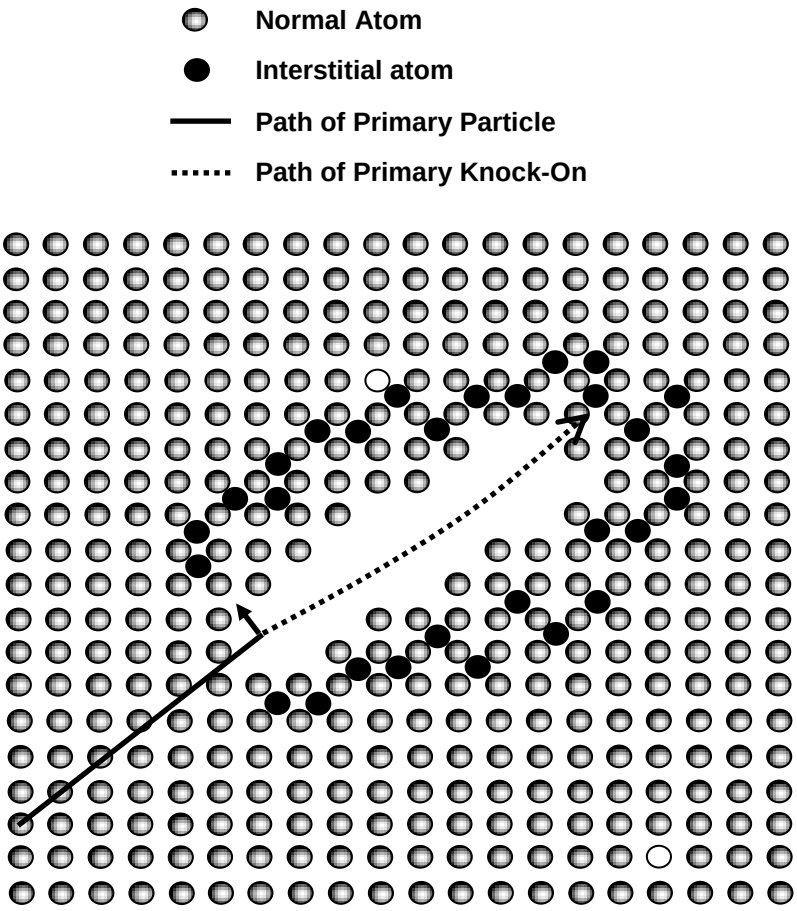

Figure 2.8: The final configuration of a cascade of crystal damage resulting from the interaction of one fast neutron with one atom, the primary knock-on atom, within a crystal. The damage cascade consists of a vacancy rich core and interstitial rich shell. (Adapted after [19])

After a very short period (several nano-seconds) during which the kinetic energy of the displaced atoms is dissipated, the core of the cascade contains a high concentration of vacancies surrounded by an interstitial- rich "shell" (Zr atoms in interstitial sites are known as self interstitial atoms or SIAs) as shown in Figure 2.8. The size of the

displacement cascade is primarily a function of the energy of the primary knock-on atom. The more energetic the atom is the larger the cascade it will produce and thus more atoms are displaced.

The amount of neutron irradiation received by a material is often expressed as neutron fluence in units of neutrons per square meter. However, for damage analysis, a more useful method is to represent the amount of radiation damage by a parameter related to the number of point defects produced. The parameter determines the number of atomic displacements per atom (dpa). In a typical CANDU reactor, 30 years (the design lifetime) irradiation produces about 30 dpa damage in the central, high neutron flux, region of the pressure tubes [11].

A large number of vacancies and interstitials within the cascade recombine in a very short time periods ($\sim 10^{-11}$ s). This is referred to as athermal recombination. The surviving fraction (~0.1) after the mutual annihilation, are free to disperse and diffuse through the crystal until they are also annihilated by further recombination or by absorption at other types of crystal defects (such as dislocations or grain boundaries). Thus, there is a balance established between point defect production and annihilation that results in a dynamic equilibrium concentration of vacancies and interstitials throughout the crystal lattice. This concentration is higher than the normal thermal equilibrium concentration and the resulting supersaturation provides the main driving force for the diffusive migration of the point defects towards the major absorption sites, such as dislocations. [11] This point defect absorption processes are believed to be the primary processes which drives the mechanism of irradiation creep.

The residual interstitials and vacancies agglomerate with similar point defects or with impurity or solute atoms in the matrix. Such agglomeration processes can lead to a number of microstructural features or extended defects which evolve during irradiation these includes point defect clusters, dislocation loops, precipitates and voids. As precipitation and voids occur to a negligible extent in the Zr-2.5%Nb alloy, these phenomena won't be discussed here.

Vacancy and Interstitial clusters form as a direct consequence of the formation of displacement cascades (Figure 2.8). If the cascades grow large enough they can transform into a higher order structure such as dislocation loops. The presence of these clusters can inhibit dislocation motion and thus strengthen the material [12].

Dislocation loops can form as a consequence of the agglomeration of vacancy or interstitial clusters into planner arrays. Vacancy type dislocation loops form as a result of the collapse of the vacancy rich zones resulting from the displacement cascade (Figure 2.9 (a)). The coalescence of vacancies on an atomic plane corresponds to a disk of atoms removed from that plane. As a result the adjacent atomic planes collapse inward and thus contraction strain is produced as indicated by the arrows in Figure 2.9(a).

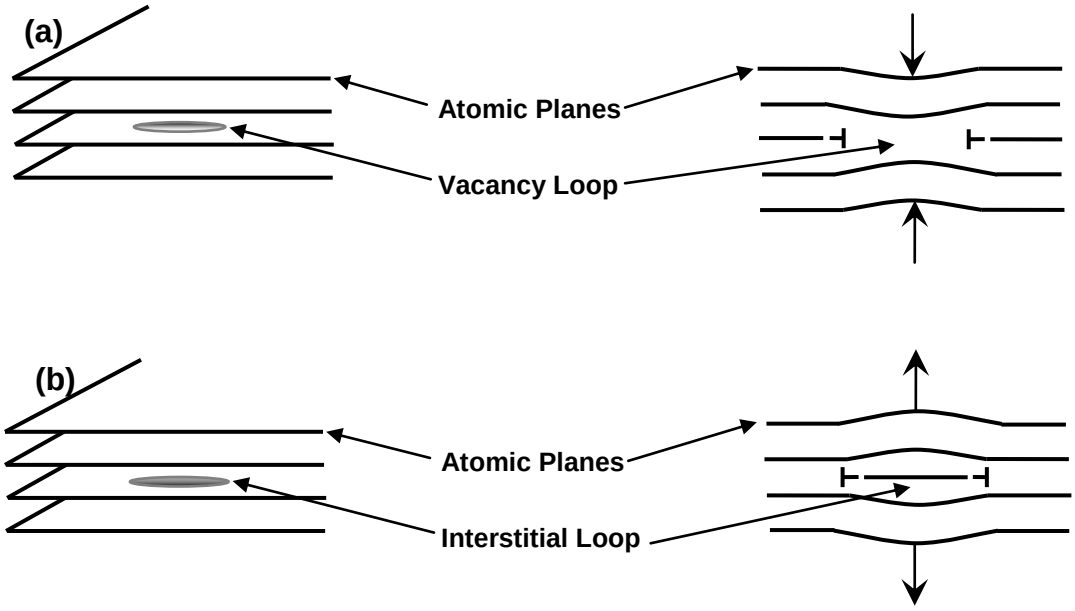

Figure 2.9: Schematic representation of (a) the vacancy loop and (b) the interstitial loop. (Adapted After [12])

Interstitial loops are formed in a similar manner. The coalescence of interstitials between atomic planes produces an extra atomic layer which results in an elongation of the lattice as indicated by the arrows in Figure 2.9(b).

Both the vacancy and interstitial dislocation loop shown in Figure 2.9 are sessile (i.e. they cannot move by dislocation glide). These loops therefore represent very effective obstacles to dislocation motion.

2.4.2 Irradiation Hardening

Research has shown that the yield stress of neutron irradiated Zr alloys follows a power law relationship with neutron fluence [12]. This is shown schematically in Figure 2.10. Chapter 3 of this thesis presents indentation test results showing similar dependence of indentation stress upon Zr-2.5%Nb material that is irradiated to various fluences of Zr^{+} ions.

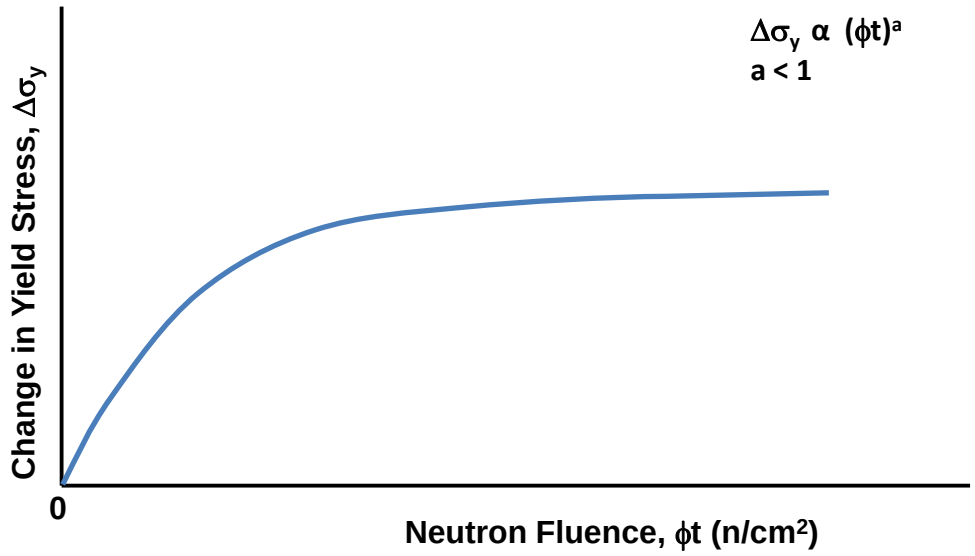

Figure 2.10: The change in yield stress as a function of neutron fluence (Adapted After [12])

It has been also found that the degree of irradiation hardening is influenced by the irradiation temperature. In general, the degree of irradiation hardening at a given level of neutron fluence decreases with increasing irradiation temperature. This is considered to be a result of accelerated thermally-activated recombination of interstitials and vacancies and increased diffusion of point defects to sinks with increasing temperature i.e. the damage production competes with damage recovery at elevated temperatures [12,20]. The results reported in Chapter 5 also shows similar decrease in irradiation hardening of Zr-2.5%Nb with increasing Zr^{+} irradiation temperature.

2.4.3 Irradiation Growth

Irradiation growth is the shape change, at constant volume that occurs during irradiation of Zr alloys in the absence of an applied stress [21,22]. Woo and Goesele [23,24] proposed that vacancies and interstitials exhibit anisotropic diffusion in Zr. The interstitials diffuse faster along the basal planes (i.e., in the <a> directions), whereas vacancies diffuse faster in the <c> direction. Previous investigations have shown that the anisotropic diffusion of vacancies and interstitials cause irradiation growth to occur by elongation along the a-axes and by contraction along the c-axis [11,19,24]. Holt et al found that the magnitude of growth in the transverse direction of a Zr-2.5%Nb pressure tube is approximately half of that in the axial direction [11]. As the volume is expected to remain constant during growth, the growth in the radial direction should be the negative sum of the growths in the axial and transverse directions meaning the amount of growth will be somewhere in between the axial and hoop directions. Models developed by Woo and others [11,25-27] have also predicted the same.

2.4.4 Thermal Creep

Thermal creep is the deformation process that describes the change in shape at a constant volume due to the effect of temperature and applied stress in the absence of neutron irradiation. The various mechanisms of thermal creep is a vast subject however, a very

brief discussion relating specifically to thermal creep of Zr-2.5%Nb pressure tubing during service in a CANDU reactor core is included in this segment.

Christodoulou et al. [2] showed that, in the absence of irradiation, thermal creep strain is anisotropic and is higher, for a given level of applied stress, in the <a> direction than in the <c> direction in the hcp crystal lattice. It was also found that pre-irradiation reduced the thermal creep rate due to irradiation hardening.

While the creep deformation of the central regions of the CANDU pressure tube is governed primarily by the large irradiation creep rate, owing to the high neutron flux, thermal creep contributes significantly to the creep deformation of the ends of the pressure tubes where the fast neutron flux is insufficient to promote significant irradiation creep but, still, is large enough to produce an irradiation hardened material. Also, thermal creep may contribute significantly to the strain in the vicinity of cracks or sharp flaws in the pressure tube. In this research indentation creep tests are performed to simulate the creep deformation around such cracks.

What follows is a description of the mechanism of high-stress thermal creep, during indentation, and the resulting equations that predict the creep rate.

2.4.4.1 Indentation Creep Mechanism and Rate Equations

Indentation tests offer a simple and direct method for investigating the mechanical properties and time-dependent flow (creep) of materials. To determine the creep properties, the indenter maintains a load over a period of time under well controlled constant temperature conditions and changes in indentation size are monitored (a more detailed description of the experimental procedure is given in section 2.6). A general description of the principal mechanism used to predict the rate of time-dependent plastic deformation during indentation is discussed in this section.

Figure 2.11 shows a deformation mechanism map for pure zirconium and depicts the stress and temperature fields over which different deformation mechanisms are prominent.

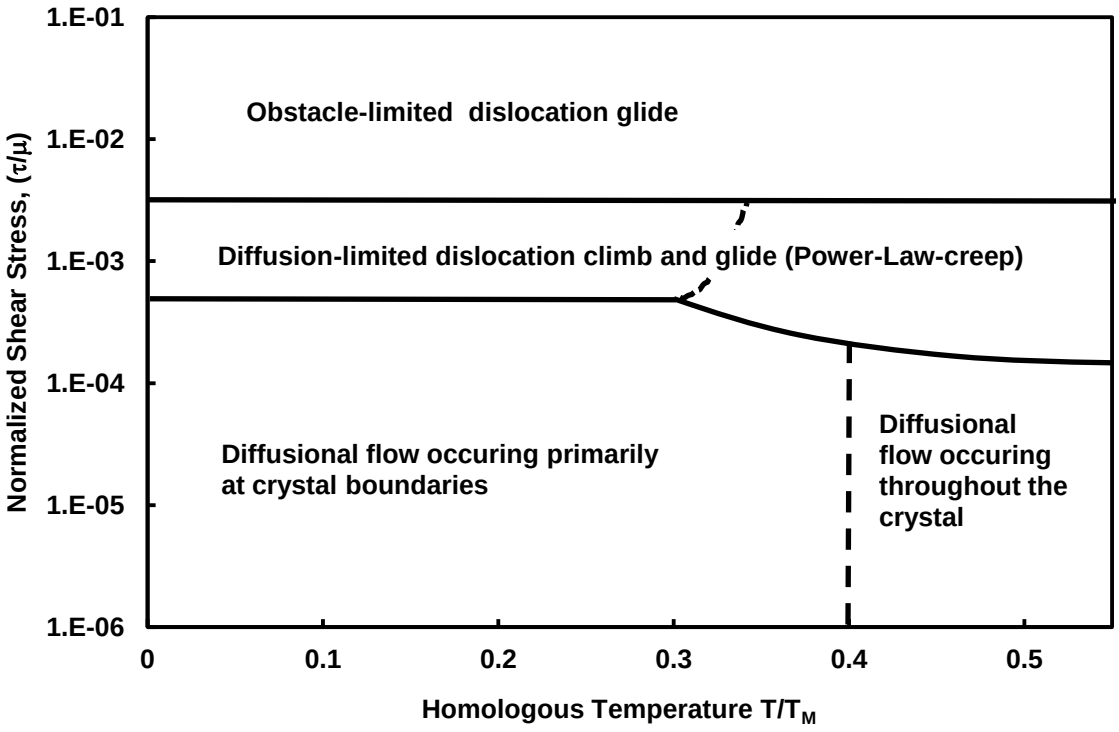

Figure 2.11: Schematic diagram of deformation mechanism map for pure Zr. Typically indentation creep occurs at $\tau/\mu \geq 0.01$. (Adapted after [28,29])

Li et al. [28] first established that the primary mechanism causing thermal creep during an indentation test at all temperatures is the obstacle-limited dislocation glide. They analyzed all the possible mechanisms, plasticity (obstacle-limited dislocation glide), power-law-creep (diffusion assisted dislocation climb plus glide), power law breakdown, recovery (dislocation climb) and diffusional creep, which may contribute to indentation creep at different temperatures (from room temperature to melting) and found that time-dependent obstacle-limited dislocation glide is the dominating creep deformation

mechanism. The high stress involved in indentation creep is responsible for the dominance of this deformation mechanism at all temperatures.

In the plastically deformed zone beneath the indenter the dislocation density is very high and the triaxial stress state is very large. Dislocations gliding under the resulting high shear stress meet obstacles and the motion of the dislocations is limited by the strength of these obstacles. These obstacles may be other dislocations, irradiation induced defects, solute atoms, second phase precipitates or grain boundaries. When mobile dislocations, having a population (i.e. dislocation density) ρ_m , move through a field of obstacles with an average velocity $\bar{\upsilon}$, they produce a shear strain rate in the crystal of [30]:

$$\dot{\gamma} = \rho_m b \bar{\upsilon} \tag{2.1}$$

Where, b is the magnitude of the Burger's vector of the dislocation. The velocity $\bar{\upsilon}$ is almost entirely determined by the waiting time of the dislocations at the obstacles.

At steady state, ρ_m is a function of stress and temperature only and can be approximated to be the result of an ideal array of edge dislocations as

$$\rho_m = \alpha \left(\frac{\tau}{\mu b} \right)^2 \tag{2.2}$$

Where, τ is shear stress, α is a constant of order unity and μ is the elastic shear modulus of the material [31].

Let us consider a straight dislocation of length ℓ gliding under an applied force $\tau b \ell$ in the direction x. If the dislocation encounters obstacles, each of which is capable of producing a resisting force F that is larger than $\tau b \ell$, the dislocation will stop at a position x_1, as shown schematically in Figure 2.12. To move towards a position, x_2, the dislocation will have to overcome the obstacle. The total area beneath the force versus distance curve illustrated in Figure 2.12 is the total energy (ΔG_0) required for a dislocation to move past the obstacle. Part of this energy comes from mechanical work done by the applied force and can be expressed as $\tau V'$, where, $V' = b\ell(x_2 - x_1)$ is referred to as the activation volume.

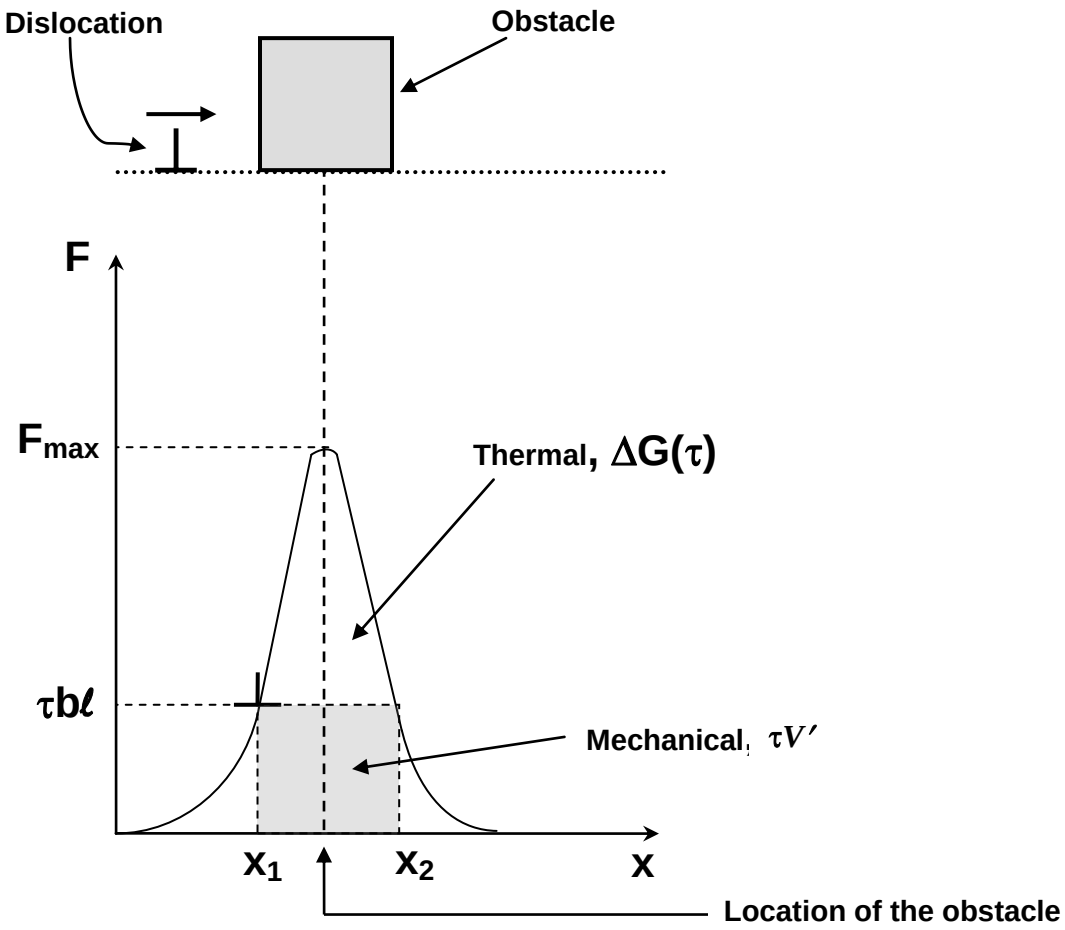

Figure 2.12: Profile of resistance force (*F*) versus distance (*x*) for barriers opposing dislocation motion.

V' is often expressed in terms of activation area, Δa, the area of the slip plane swept by the dislocation during its activation, times the Burger's vector, *b*. Activation area is essentially the product of ℓ and the activation distance (which is related to the obstacle size), d and, in this case, d= x_2- x_1. The mechanical contribution, $\tau V'$, is not large enough to push the dislocation past the obstacle. So, the remainder of the energy must be provided by thermal fluctuations of the atoms in the immediate vicinity of the

dislocation/obstacle interface. The thermal energy $\Delta G(\tau)$ which must be supplied can be expressed as

$$\Delta G(\tau) = \Delta G_0 - \tau V' \tag{2.3}$$

The probability of thermal vibrations producing the thermal activation energy $\Delta G(\tau)$ at temperature T is represented by the Arrhenius function $exp(-\Delta G(\tau)/kT)$, where k is the Boltzmann constant [32]. So, the mean velocity of the dislocations, effectively vibrating at a frequency ν, and having a thermal activation energy $\Delta G(\tau)$ can be expressed by the kinetic equation [30],

$$\bar{\upsilon} = \beta b\nu \, exp - \frac{\Delta G(\tau)}{kT} \tag{2.4}$$

Where, β is a dimensional constant, b is the magnitude of Burger's vector and ν is the frequency of atomic vibration at 0ºK (the Debye frequency with a value of $10^{12}s^{-1}$).

Considering all shapes and distribution of obstacles, Kocks et al. [33] proposed the following general equation which shows the dependence of $\Delta G(\tau)$ upon τ

$$\Delta G(\tau) = \Delta G_0 \left[1 - \left(\frac{\tau}{\hat{\tau}} \right)^p \right]^q \tag{2.5}$$

Where, $\hat{\tau}$ is the ''athermal'' flow strength of the material at 0ºK and p,q are the constants that define the shape of the force/distance curve (Figure 2.12) for the obstacle. The value of p and q are usually bounded by $0 \leq p \leq 1$, $1 \leq q \leq 2$ [30].

The thermal activation energy, ΔG_0, characterizes the strength of a single obstacle. Frost and Ashby [30] classified common types of obstacles to dislocation glide in terms of their strength (Table 2.1).

Table 2.2: Classification of common types of obstacles to dislocation glide according to their strength ΔG_0 [30]

Obstacle strength	ΔG_0	Examples
Strong	$2\ \mu b^3$	Dispersions: large or strong precipitates
Medium	$0.2\text{-}1.0\ \mu b^3$	Forest dislocations, small or weak precipitates
Weak	$<0.2\ \mu b^3$	Lattice resistance, solid solution hardening

Combining equations 2.1, 2.2, 2.4 and 2.5 leads to the following constitutive equation that predicts the shear strain rate as a function of the applied shear stress and temperature for plastic deformation occurring by the mechanism of obstacle controlled dislocation glide [30]:

$$\dot{\gamma} = \dot{\gamma}_p \left(\frac{\tau}{\mu}\right)^2 \exp\left\{-\frac{\Delta G_0}{kT}\left(1-\left(\frac{\tau}{\hat{\tau}}\right)^p\right)^q\right\} \tag{2.6}$$

Where, $\dot{\gamma}_p$ is a constant approximately equal to 10^{11} s^{-1}, k is Boltzmann's constant (= 1.38 $\times$ 10^{23} J/K).

2.4.5 Irradiation Creep

It is well established (as discussed in the previous sections) that irradiation produces a number of extended defects which can both inhibit dislocation motion causing irradiation hardening as well as dimensional changes even in the absence of stress. In addition, a large number of free point defects are produced over and above the population which normally exists in thermal equilibrium. It is believed that, the net fluxes of these free

point defects to certain selected sites (probably dislocation loops) in the material leads to accelerated creep rates.

There are divided opinions about the basic physical processes responsible for irradiation creep in Zr alloys. Some of the current irradiation creep mechanisms will be briefly discussed here. The mechanisms are grouped into three categories: irradiation-retarded, irradiation-enhanced and irradiation-induced creep.

Irradiation retarded creep mechanism refers to the reduction of thermal creep rates due to irradiation hardening [12]. Irradiation-induced defects such as vacancy and interstitial clusters, dislocation loops and damaged or depleted zones due to displacement cascades are all present in the irradiated microstructure. Since many of these defects, such as the dislocation loops, are sessile, they do not contribute to accelerating the creep rate rather they only slow the creep rate by acting as immobile obstacles to dislocation glide.

Irradiation-induced creep mechanisms are those which operate in addition to thermal creep mechanisms. Two of the proposed general mechanisms that cause irradiation creep are referred to as yielding creep and creep by Stress Induced Preferred Absorption (SIPA).

The yielding creep mechanism [12] assumes that in the absence of stress, individual grains of polycrystalline Zr alloy will attempt to change shape by the irradiation growth mechanism as described previously. This growth-induced expansion and contraction of an individual grain will be resisted by the neighbouring grains. The resulting inter-granular stress can be relieved by plastic yielding or creep and the superposition of an applied stress would bias this plastic deformation in the direction of applied stress. Continued growth therefore also causes continued creep deformation.

In the SIPA mechanism it is assumed that a bias of the point defect diffusion to a dislocation is a function of the orientation of the burgers vector with respect to the applied stress. Dislocations having Burgers vectors aligned parallel to an applied tensile stress experience a net flux of interstitials and those aligned with an applied compressive stress experience a net flux of vacancies. It is believed that the anisotropy of point defect

migration is also stress dependent. This is referred as SIPA_DAD or elasto-diffusion (ED) [11,12].

Irradiation-enhanced creep mechanisms are those which promote an acceleration of normally operating thermal creep mechanisms [12]. Similar to the irradiation-induced creep mechanisms, the irradiation-enhanced creep mechanisms are several. The most favoured irradiation-enhanced-creep mechanism is an extension of the dislocation creep model of thermal creep (section 2.4.4) where now because of the constant irradiation activated production of point defects dislocations are able to bypass the obstacles by climb due to the absorption of vacancies. A schematic representation of climb assisted glide mechanism is shown in Figure 2.13.

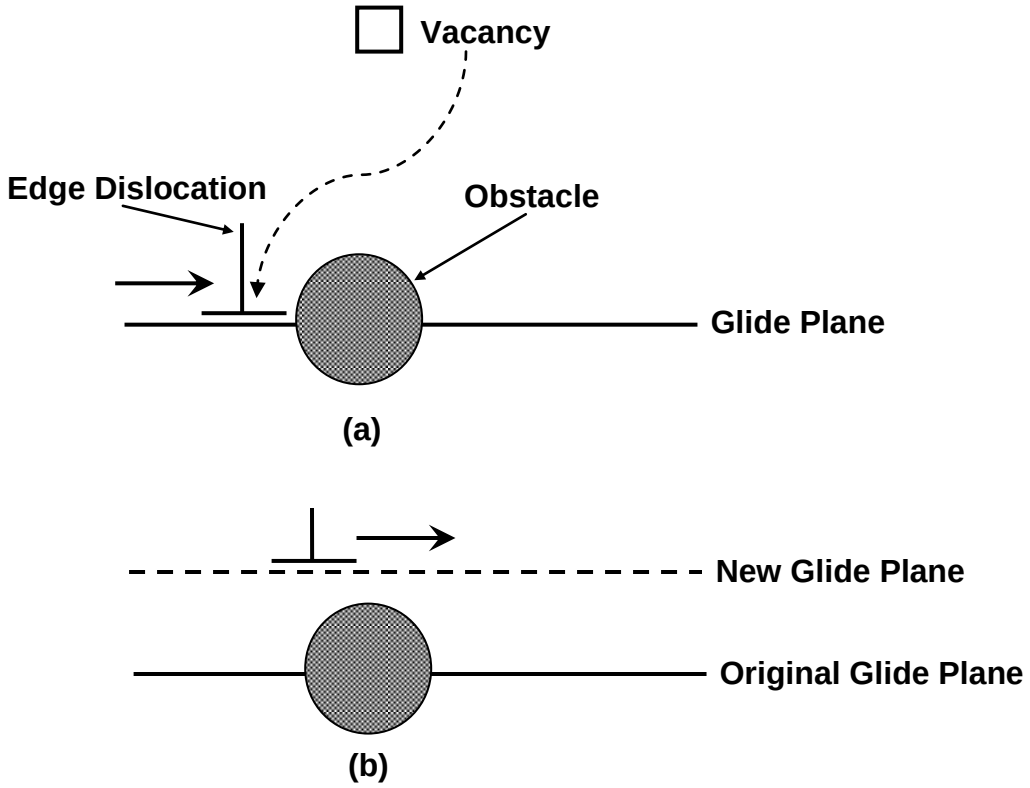

Figure 2.13: Plastic strain produced by climb-plus-glide mechanism (a) a dislocation (moving left to right) is held up by an obstacle (b) climb has occurred by vacancy absorption and the dislocation raises to a new glide plane continuing deformation (Adapted After [19])

The stress dependence of irradiation creep in Zr alloys has been investigated by several researchers [34-36].

Figure 2.14 shows a schematic illustration of the stress dependence of the creep rate of Zr-2.5%Nb alloy for thermal creep, irradiation creep and post-irradiation creep in the LWR temperature regime.

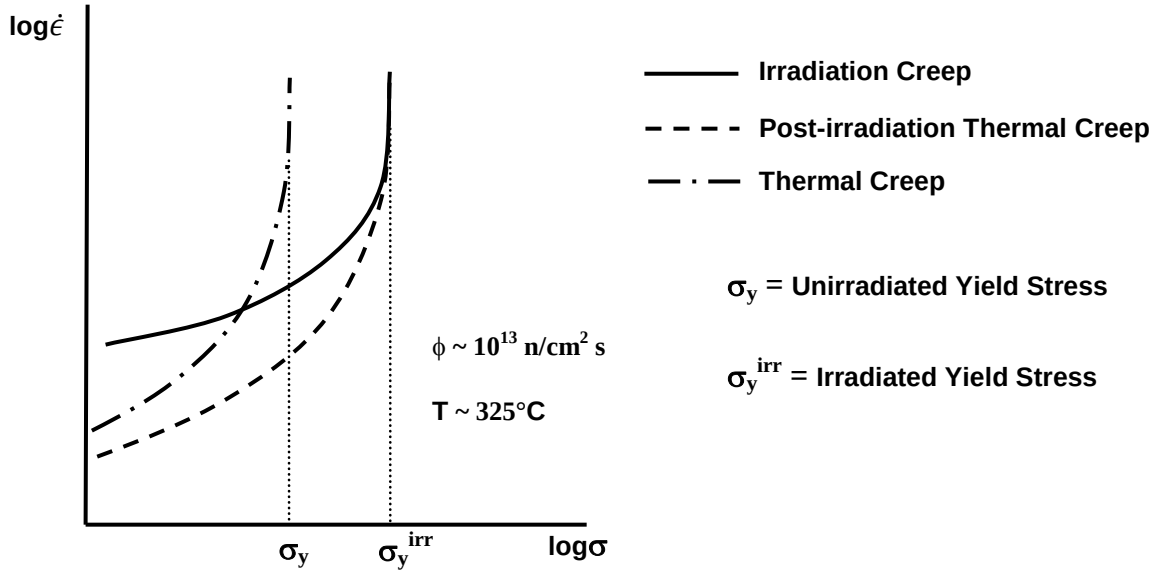

Figure 2.14: Schematic illustration of the variation of creep rate with stress in Zr alloys (Adapted after [12])

Figure 2.14 indicates that as the applied stress approaches the flow stress of the material, the creep rates increases to very large values. Due to irradiation hardening, the post-irradiation thermal creep curve is shifted to the right. Irradiation increases the creep rate over the post-irradiation creep rate for the entire stress range. However, the enhancement is negligible at high stresses, and the amount of enhancement increases with decreasing stress. At very low stresses the irradiation deformation rate is almost stress independent as the deformation proceeds predominantly as a result of concurrent creep deformation associated with grain to grain variation in the rate of irradiation growth [12].

Fidleris [37,38] suggests that the temperature dependence of in-reactor creep is always smaller than out-of-reactor creep except at high temperatures where thermal creep dominates in-reactor behaviour. Moreover, except at these higher temperatures, the in-reactor creep rate is always greater than the thermal creep rate.

The flux dependence of irradiation creep has been assumed to follow a power law relationship [12]

$$\dot{\epsilon}_{irr} = C\phi^{p} \tag{2.7}$$

Where, ϕ is the neutron flux (generally, $E_{neutron} \geq 1.0$ MeV) and *C, p* are constants for a given sets of conditions.

2.5 Pyramidal Indentation Testing

Pyramidal indentation testing offers a method for measuring, with micrometer scale spatial resolution, the local variations in the mechanical properties of a material. In the case of Zr-2.5% pressure tubes this type of testing allows us to choose samples from any direction of the pressure tube to assess the degree of mechanical anisotropy and, also, to assess the effect of irradiation on mechanical properties of the material.

Indentation testing involves pressing a small, rigid, indenter against a flat surface of the test material. If the shape of the indenter is known, the projected area of the indentation on the sample surface can be calculated from the indentation depth. The applied indentation force divided by this projected area is the average indentation stress which is related to the flow stress of the test material.

Section 2.5.1 describes the geometry of the Berkovich indenter that was used in this investigation along with the equations describing the indentation contact area and the average indentation stress. A description of the various components of the Micro-Materials Micro-/Nano-test platform used to perform the indentation creep tests described in Chapters 4 to 6 is included in Section 2.5.2. The section also includes the methods used to analyze the indentation force and depth data resulting from constant load

indentation creep tests. Finally, a description of the indentation strain rate change test is given in Section 2.5.3.

2.5.1 The Pyramidal Indenter

Indentation tests in this research were all performed using a Berkovich indenter which is a three-sided pyramid usually constructed from a diamond crystal by a grinding operation. The main requirements for a suitable indenter for a indentation test are low friction with the indented material, no plastic deformation, smooth surface and high elastic modulus. Choosing diamond for the indenter tip satisfies these requirements. Another main requirement is a very precise indenter point. The three-sided geometry of a Berkovich indenter ensures that a sharp pointed tip can be made. The Berkovich indenter has a much sharper tip than a four-sided Vickers indenters since the edges of a three-sided pyramid can be constructed more easily to meet at a single point rather than the inevitable line that occurs when constructing a four-sided Vickers pyramidal indenter. [39].

The Berkovich indenter geometry is shown in Figure 2.15. It has a triangular base with three triangular faces inclined at an angle of 65.27° with respect to the vertical axis (Figure 2.15 (a)). The radius of the tip of the pyramid is typically less than 100nm [40]. The impression made by a Berkovich indenter appears as an equilateral triangle (Fig. 2.15 (b)). The projected area, A, of the triangle is related to the indentation depth h, and the face angle θ by the following equation:

$$A = 3\sqrt{3}\, h^2 \tan^2\theta \tag{2.8}$$

Since $\theta = 65.27°$, A is expressed in terms of h as

$$A = 24.5\, h^2 \tag{2.9}$$

The mean indentation contact pressure or stress is expressed as:

$$\sigma_{ind} = \frac{Indentation\ Force}{24.5h^2} \tag{2.10}$$

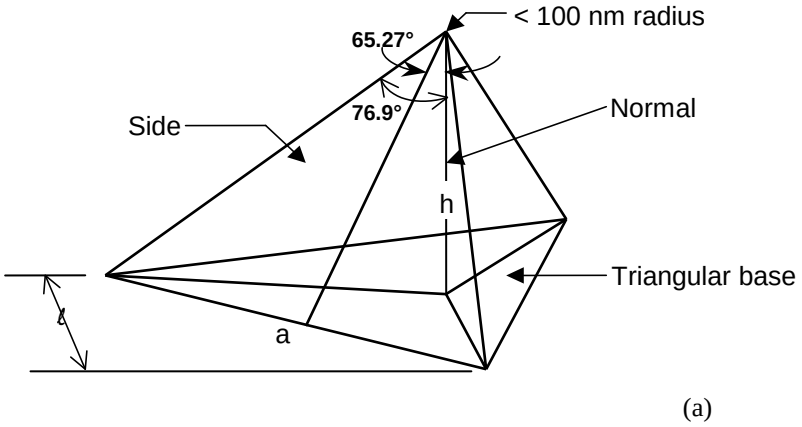

(a)

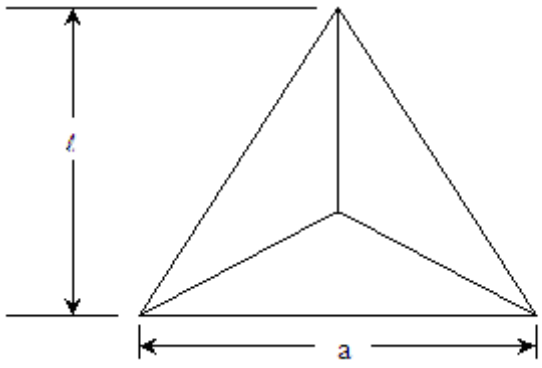

(b)

Figure 2.15: Schematic diagram of (a) a Berkovich tip and (b) an impression an indentation made by a Berkovich tip indented on a flat surface (Adapter after [40]).

2.5.2 The Indentation Creep Test Platform

If a constant force indentation test is performed for an extended period of time the indentation depth will increase with time as the indenter sinks into the test material through a process of time-dependent "creep" deformation. By monitoring the rate at which the indentation depth increases the local time-dependent flow properties of small volumes of the test material can be studied. This is the objective of the studies presented in this thesis.

All the indentation creep tests in this study were performed using a computer controlled indentation-testing platform made by Micro Materials Ltd., Wrexham, UK. Figure 2.16 shows a schematic diagram of this instrument [Original design - University of Lancaster, UK, Newey, Wilkins and Pollock, J Phys E, 1982, pp119-122]. The heart of the instrument is a ceramic pendulum that is mounted vertically. A copper wire is coiled and wrapped around an aluminum core attached to the upper end of the pendulum. The pendulum rotates about a pivot located at its mid-height. The bottom end of the pendulum contains the holder upon which a diamond Berkovich indenter is attached. When electric current is supplied to the coil, the core is magnetized and is attracted to the nearby permanent magnet. This causes the pendulum to rotate and the indenter to move toward the sample. A parallel plate capacitor located behind the indenter measures the movement of the indenter. A computer control system is interfaced with the indenter and controls the indentation process by controlling the electrical current fed to the coil. The indentation force is a function of the magnitude of this current. The indentation depth is related to the capacitance measured across the parallel capacitor plates. Both the relationships between indentation force and coil current and indenter displacement and capacitance are determined by calibration tests performed frequently during the course of indentation testing.

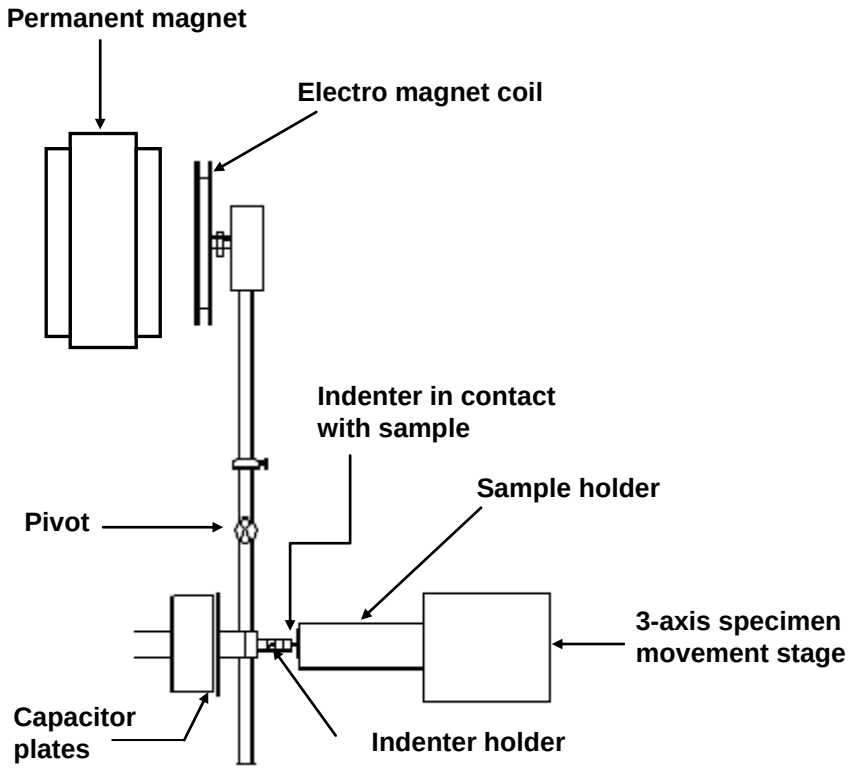

Figure 2.16: Schematic diagram of a NanoTest Platform assembly.

The instrument consist of two pendulums: a low load (0.1-500 mN) "NanoTest" pendulum for performing nano-indentation tests and a high load (0.1-20 N) "MicroTest" pendulum for performing deeper micro-indentation tests. A three-axes mechanical translation stage is used to position the sample, with a spatial resolution of about ±1μm. The indentation displacement range for nano-indentations is about 7μm with a precision less than ±0.2 nm. For the micro-indentation the displacement range is 50μm with lower associated precision. Software is used to control all indentation tests. It allows positioning the sample stage, finding the sample surface, specifying different parameters such as loading and unloading rates, indentation depth, and length of time etc.

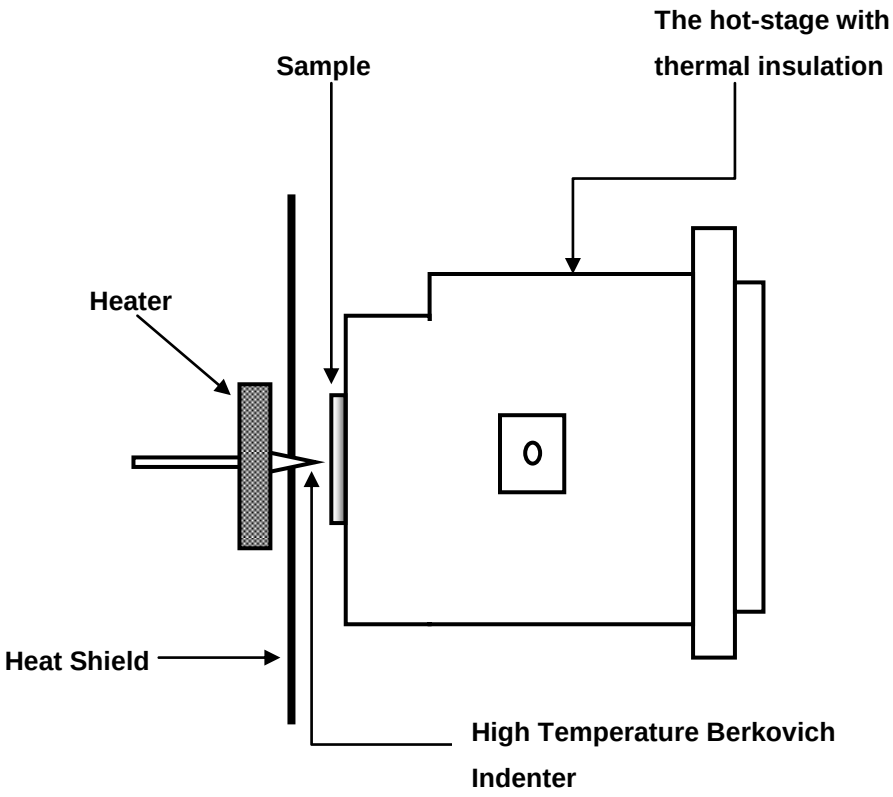

Figure 2.17: Schematic illustration of high temperature testing configuration.

High temperature constant-force indentation creep tests (chapter 6) were performed using the "MicroTest" indentation pendulum. A dual heating stage was employed to simultaneously heat the indenter and the sample to minimize the thermal drift during the indentation test (Figure 2.17). Both heaters were controlled with separate PID (proportional–integral–derivative) temperature controllers. An aluminium shield was used to prevent any thermal interference with the ambient electronics and depth sensing equipment.

2.5.2.1 Indentation Creep Tests

In this thesis all the indentation creep investigations described in chapter 3 to chapter 5 were performed using the "NanoTest" indentation pendulum and those in chapter 6 were performed using the "MicroTest" pendulum. During constant load indentation creep test the indentation load was kept constant for one hour when the indentation tests are performed at room temperature tests and for 300 seconds when the tests were performed at higher temperature (200, 300, 400 °C). The results were corrected, using the NanoTest software, for both thermal drift and elastic compliance of the indentation testing assembly.

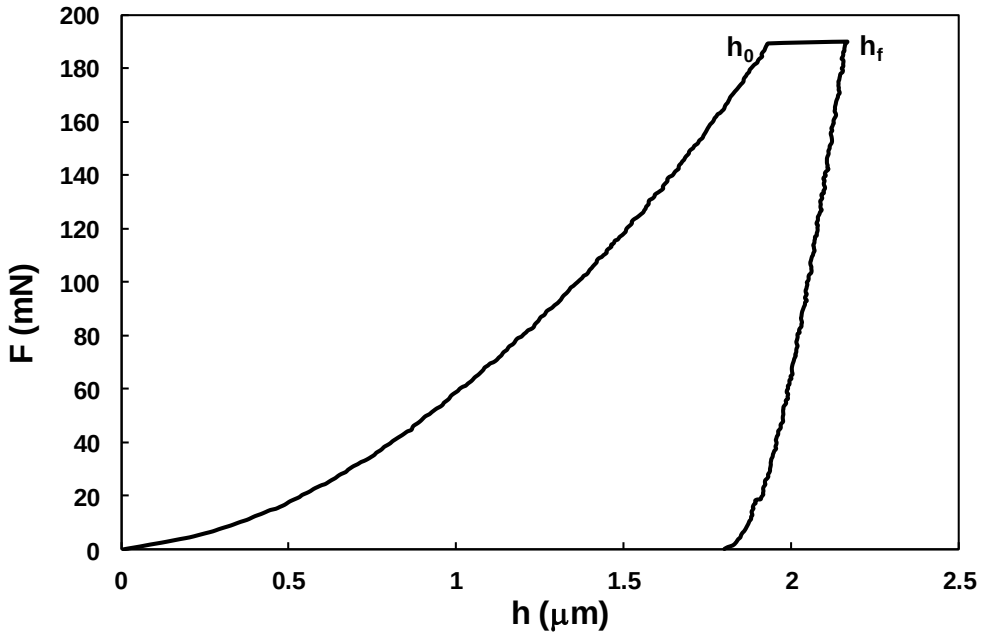

Figure 2.18: Typical load-displacement curve. During the tests, the indentation load is increased to reach the desired h_0. The indentation load is then held constant for one hour (for room temperature test) or 300 seconds (for high temperature tests). The horizontal part of the curve, between h_0 and h_f, shows the amount of creep that occurs during the constant-load stage of the indentation test.

Force, displacement and time are measured continuously throughout a test performed with the indentation tester. An indentation creep test gives a curve that shows the relationship between Force, *F* and indentation depth, *h*. The measured *h* includes contributions from both the elastic and plastic deformation of the indented material. A typical indentation force versus depth curve for a constant load pyramidal indentation test is shown in Figure 2.18.

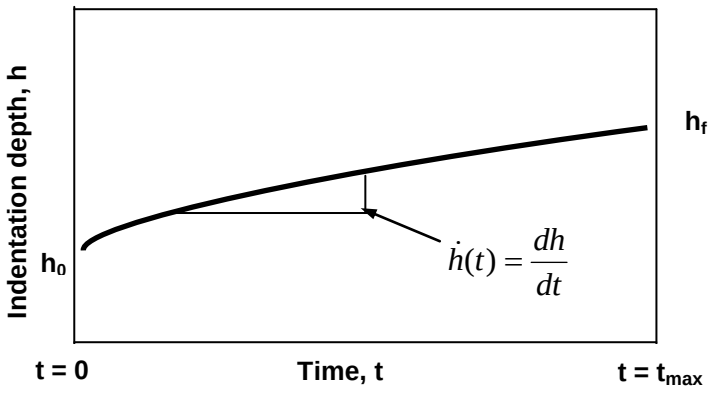

Figure 2.19: Diagram of a typical indentation depth versus time plot obtained from a constant load indentation test.

Constant-load indentation tests are performed by loading a specimen to a predetermined load to reach the required indentation depth and then keeping the load constant for a prescribed length of time. Figure 2.19 shows a plot of a typical indentation depth versus time curve.

For a pyramidal indentation the ratio D/h (Figure 2.20) is always constant regardless of the magnitude of *h*. As the average indentation strain is a function of D/h, it remains constant, regardless of indentation depth, due to the self-similar geometry of the Berkovich indenter. However, the local indentation strain rate anywhere within the plastic zone changes with time. Indentation strain rate is therefore a ratio of the

indentation velocity, $\dot{h}(t)$, to the instantaneous indentation depth, *h(t)* and can be expressed as

$$\dot{\varepsilon}_{ind} = K\frac{\dot{h}(t)}{h(t)} \tag{2.11}$$

where the constant K is related to both of the geometry of the indenter and the work hardening property of the indented material [41]. In most cases, researchers use K=1 and refer to $\dot{\varepsilon}_{ind}$ as the "nominal" indentation strain rate.

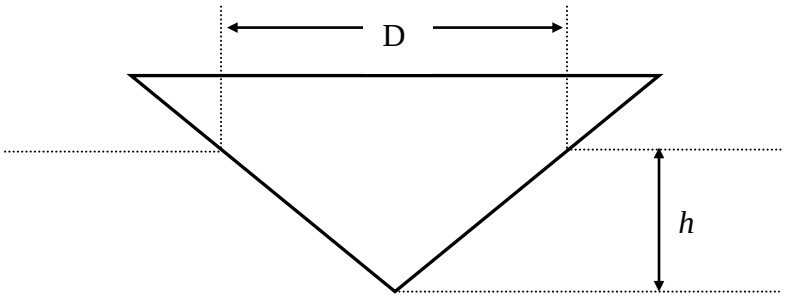

Figure 2.20: Schematic diagram of a geometrically self-similar pyramidal indenter.

When the indentation depth, *h*, is large (more than 10 micrometers), the indentation stress, σ_{ind}, measured by geometrically self-similar Berkovich indentation is essentially independent of h. This is not the case in this investigation where $h \leq 10\mu m$. The σ_{ind} values measured by indentation test increase with decreasing *h*. This is known as the indentation size effect [42] and has been studied extensively [42-50] with various mechanisms being proposed to explain the phenomenon. The most accepted mechanism applies the strain gradient plasticity theory [42-44] to suggest that large numbers of geometrically necessary dislocations resulting from the presence of a substantial strain gradient around the shallow indentations causes enhanced hardening which causes the

observed increase in σ_{ind} [51]. A description of this phenomenon is also included in Chapter 3.

2.5.3 Pyramidal Micro-Indentation Strain Rate Change Tests

Micro-indentation tests incorporating rapid changes in the indentation velocity were developed to directly measure the strain rate sensitivity of the flow stress of materials and, thus, to deduce parameters like the apparent activation work, $\Delta W'$ and activation volume, V', of the subsequent deformation process [52]. The use of a piezoelectric displacement actuator, located behind the sample, allows one to invoke high precision instantaneous indentation strain rate changes such that significant changes in the dislocation density of the deformed structure beneath the indenter do not have time to occur [53]. This sudden change in indentation strain rate leads to a corresponding sudden change in the yield stress of the indented material. By measuring this change in yield stress, which has occurred under essentially constant microstructure, one is able to deduce parameters describing the operative mechanism of time-dependent obstacle-limited dislocation glide.

The following simplified rate equation describing thermally activated obstacle limited dislocation glide deformation process can be expressed by simplifying equation 2.6 as [33]

$$\dot{\gamma} = \dot{\gamma}_0 \, exp\left(-\frac{\Delta G}{kT}\right) \tag{2.12}$$

This equation can then be re-expressed in terms of normal strain rate and stress as

$$\dot{\varepsilon}_{in} = \dot{\varepsilon}_0 exp - \left(\frac{\Delta G_0 - \sigma V'}{kT}\right) \tag{2.13}$$

where $\dot{\varepsilon}_{in}$ is the inelastic, or plastic, strain rate, $\dot{\varepsilon}_0$ is the product of the population density of dislocation sources and their frequency of vibration, σ is the applied stress causing plastic flow [52].

Taking the derivative of $\ln\dot{\varepsilon}_{in}$ with respect to σ yields:

$$\left.\frac{\partial ln\dot{\varepsilon}_{in}}{\partial\sigma}\right|_{T,\Sigma} = \frac{V'}{kT} - \frac{1}{kT}\left.\frac{\partial\Delta G_0}{\partial\sigma}\right|_{T,\Sigma} + \left.\frac{\partial \ln(\dot{\varepsilon}_0)}{\partial\sigma}\right|_{T,\Sigma} \tag{2.14}$$

Where the differentiation is performed under constant T and constant dislocation structure, Σ condition. The strain rate change measurement based on this partial differentiation can only be experimentally performed if the elastic displacement transients of the load frame and specimen are eliminated from the rate change [52].

If the microstructure of the indented material, as indicated by the parameter Σ in equation 2.14 remains constant, all parameters related to the microstructure, i.e. the total activation energy of the obstacle, ΔG_0, the pre-exponential term $\dot{\varepsilon}_0$ can be assumed constant and the apparent activation volume V' of the deformation process can be determined using the simplified differential form

$$\frac{V'}{kT} = \left.\frac{\partial ln\dot{\varepsilon}_{in}}{\partial\sigma}\right|_{T,\Sigma} \tag{2.15}$$

For indentation testing, the measured indentation stress (equation 2.10) is approximately equivalent to $3\sigma_y$ [54] and the strain rate is equivalent to $\frac{\dot{h}}{h}$ (equation 2.11). So equation 2.15 can be re-written as:

$$V' = 3kT\frac{\Delta ln(\dot{h}/h)}{\Delta\sigma_{ind}} \tag{2.16}$$

Equation 2.14 applies only to the plastic strain rate, $\dot{\varepsilon}_p = \dot{\varepsilon}_T - \dot{\varepsilon}_E$, where $\dot{\varepsilon}_T$ is the total strain rate and $\dot{\varepsilon}_E = \frac{\dot{\sigma}}{E}$ is the elastic strain rate and E is the elastic modulus. When the inelastic strain rate is reduced significantly, by a factor of 1/10, the yield stress of the indented material will be lowered and hence the indentation stress will also be reduced by an amount $\Delta\sigma_{ind}$. Figure 2.21, taken from Newson et al. [55], illustrates schematically how an instantaneous indentation strain rate change can be executed. Figure 2.21(a) shows the desired plastic strain rate change. A drop in indentation stress, $\Delta\sigma_{ind}$,

associated with the change in inelastic strain rate is expected, as shown in Figure 2.21(b). Once $\Delta\sigma_{ind}$ has been recorded it is possible to use equations 2.15 and 2.16 to determine the deformation parameter V' and strain rate sensitivity of the indented material.

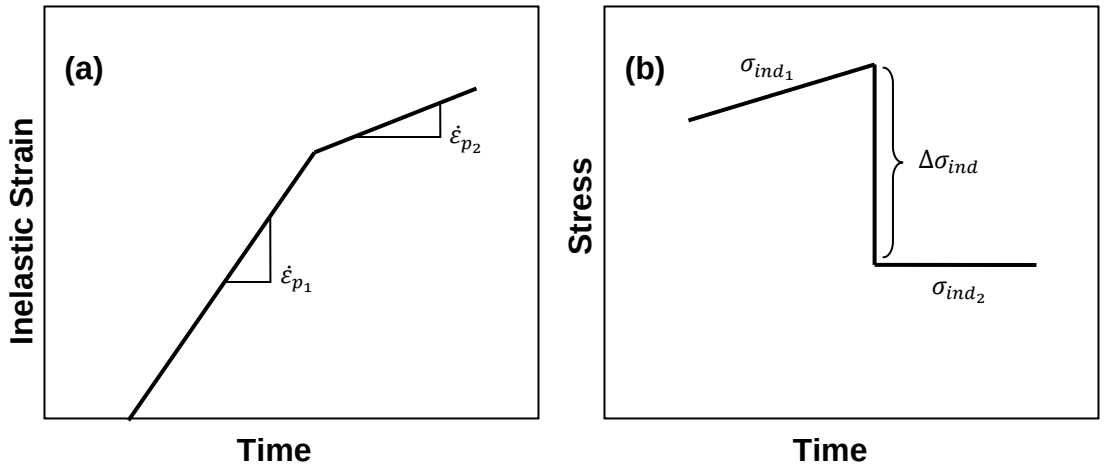

Figure 2.21: Schematic illustration of the step ramp indentation testing method used to obtain instantaneous strain rate changes: (a) the desired inelastic strain rate change; (b) the theoretically predicted stress response to the rate change in (a) (Adapted After [55])

2.5.3.1 The Testing Equipment

The instantaneous strain rate change micro-indentation tests were performed with a custom built, computer-controlled micro-indenter located in the laboratory of Professor B.J. Diak at Queen's University in Kingston Ontario. The indenter is developed with the displacement controlled to ±0.5nm with a piezoelectric actuator incorporating a capacitance displacement sensor and a semiconductor load cell [55]. Indentations are made with a Berkovich diamond tip indenter operating at a controlled displacement rate of 0.05μm/s. The load cell has a capacity of ±50 g with a resolution near ±0.2mg. The indentation depth and load are recorded at every 0.02 s over the duration of the test. Each test consists of performing an indentation at a displacement rate of 0.05 μm/s while

recording the indentation load and depth at intervals of 0.02s. Periodically the displacement rate is suddenly dropped by a factor of 10 and the subsequent change in indentation load is recorded such that $\Delta\sigma_{ind}$ can be determined. Further description of this procedure and its application to characterize the Zr-2.5%Nb CANDU pressure tube material is included in Chapter 7.

2.6 Indentation testing of nuclear materials

Pyramidal indentation tests have been performed extensively in the past on a variety of nuclear materials, such as zirconium hydrides, stainless steel fuel pins and Zircaloys [56-59]. Kuroda et al. [56] performed nanoindentation tests on zirconium hydrides and observed that the hardness increased with decreasing indentation depth in a manner similar to the much reported indentation size effect discussed in section 2.5.2.1. Kutty et al. [57-59] performed constant load indentation creep tests on Zircaloy welds, stainless steel end-plug welds and Ti modified stainless steel cladding at various temperatures. They analyzed the indentation creep data to differentiate between the creep properties of the weldments and the base metal based on their different microstructures [59]. These investigations show that pyramidal indentation creep tests are highly suitable, and have sufficient resolution, to determine the deformation properties of nuclear materials based on their local microstructure. Robertson et al. [60] performed indentation tests on ion-irradiated stainless steel sample and measured parameters like hardness and elastic modulus. Although they didn't perform any creep test, this investigation is a good example of performing indentation test on ion-irradiated material to investigate the effect of irradiation on the mechanism of plastic deformation. This approach is similar to that reported in Chapters 3-5 and 7. They also performed Transmission Electron Microscopy (TEM) studies to get the microstructural information in the plastic regime. TEM observations in conjunction with micro-indentations were also carried out in some other investigations to correlate indentation hardness to the dislocation distribution around indentation [61,62]. In chapter 3 of this thesis similar TEM observations are carried out to

characterize the dislocation structure around the indentations made in as-received and ion-irradiated Zr-2.5%Nb pressure tube material.

Typically, anisotropy parameters related to extruded and cold-drawn Zr-2.5%Nb pressure tubing are evaluated from stress and strain data obtained from uni-axial and/or bi-axial loaded specimens [63-75]. Murty and others [76,77] developed flat punch impression test methods and ball indentation test methods to determine these anisotropy parameters relatively more directly from yield and flow stresses along the three principal directions of textured Zircaloy pressure tubes. They reported that the direction parallel to the c-axis is the strongest while the other two directions are of roughly equal strength [77]. Investigations also found that neutron irradiation of Zr-based alloys leads to modifications of the mechanical anisotropy. Mahmood et al. [78] performed flat-punch impression tests and observed an increase in the mechanical strength and a decrease in the mechanical anisotropy of Zircaloy "TREX" material after irradiation. Nakatsuka et al [79,80] performed Knoop hardness tests on Zircaloy cladding and found a reduction in plastic anisotropy. They suggested that neutron irradiation strongly affects deformation by prismatic slip when compared with other deformation modes and this causes the observed decrease in the anisotropy of the yield stress. However, no such test were carried out so far to experimentally determine the effect of irradiation on the mechanical anisotropy parameters of Zr-2.5%Nb pressure tube materials.

2.7 Ion Irradiation

Zr^{+} irradiation for this research was performed using 1.7 million volt (MV) high current tandem ion accelerator located at Western University ion implantation facility. Ion beams of almost any non-radioactive element can be generated by the ion sources of this accelerator. In the implantation chamber (where the samples are irradiated), substrates can be mounted on a nickel block which can be heated or cooled to any temperature in the range -195 to 600°C. The temperature is monitored by 3 thermocouples imbedded in the nickel block. In this research, the irradiations were performed in a vacuum (10^{-11} Pa)

with the sample attached to a water-cooled holder in order to minimize the extent of irradiation-induced heating.

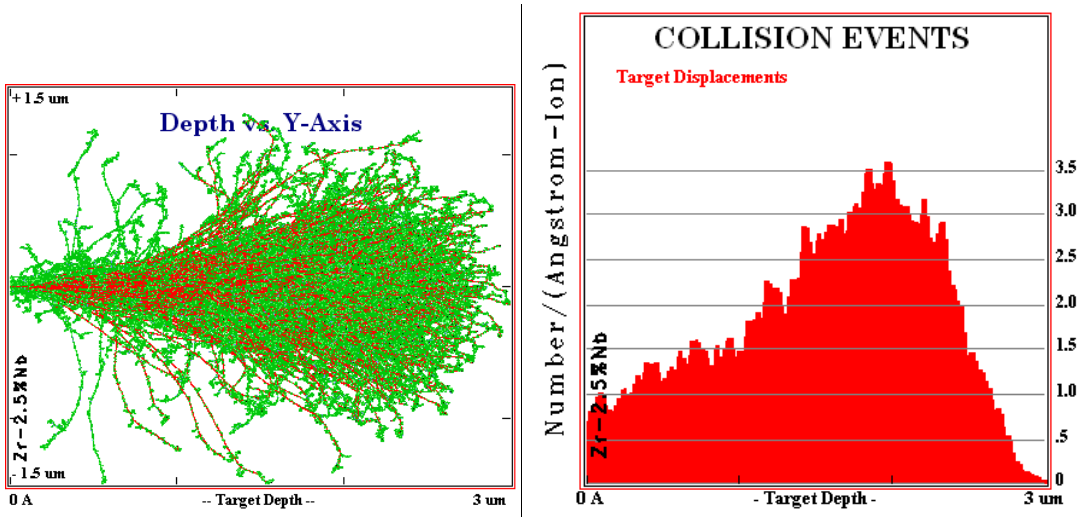

Figure 2.22: SRIM outputs (a) collision sequences (b) target displacements.

In this research the samples taken from Zr-2.5%Nb pressure tubes were irradiated with 8.5 MeV Zr^{+} ions to a fluence of $7.07x10^{15}$ ions/cm^2. SRIM software indicate that the maximum interaction of the Zr^{+} ions with the Zr-2.5%Nb alloy occurs at a depth between 2.0 and 2.5 μm. This software calculates the stopping and range of ions in materials and uses Monte Carlo simulation technique to model how far into a metal an ion (of a specific kinetic energy) travels before it stops and calculates the interaction of the ions with material. This software gives the number of atomic displacements created per ion depending on the energy of the ions (8.5 MeV for this research) and the properties of the target material. From this information it is possible to calculate the ion irradiation fluence required to produce a certain level of irradiation damage, and corresponding dpa (displacements of atoms), at specific depth within the target material. Figure 2.22 (a) shows the collision sequences of a 8.5 MeV Zr+ ion in a Zr-2.5%Nb target and Figure

2.22(b) shows the target displacements, which is the number of atoms knocked from their lattice site as calculated by the SRIM software.

2.8 Conclusions

The primary objective of this research is to apply pyramidal indentation test techniques to assess the effect of indentation depth, Zr^{+} irradiation damage and temperature on the mechanical anisotropy and local plastic deformation parameters of the Zr-2.5%Nb CANDU pressure tube material. Descriptions of the theories, mechanisms and techniques which were applied to achieve the objective were discussed in this chapter. The following chapters include detailed descriptions of all the investigations carried out for this research.

2.9 References

[1] V. Perovic, , G.C. Weatherly, R.G. Fleck, Canadian Metallurgical Quarterly, v. 24 (1985), p. 253

[2] N. Christodoulou, P.A. Turner, C.N. Tomé, C.K. Chow, R.J. Klassen, Metallurgical and Materials Transactions A, v. 33A (2002), p. 1103

[3] R.A. Holt, A.R. Causey, M. Griffiths, E.T.C. Ho, Zirconium in the nuclear industry: Twelfth International Symposium, ASTM, ASTM STP 1354 (2000), p. 86

[4] M. Griffiths, J.F. Mecke, J.E. Winegar, Zirconium in the nuclear industry: Eleventh International Symposium, ASTM, ASTM STP 1295 (1996), p 580

[5] C.E. Coleman, A.R. Causey, V. Fidleris, AECL, Chalk River Nuclear Laboratories, Chalk River, Ontario, AECL-5042 (1975), p. 1

[6] B. Lustman, F. Kerze Jr, The Metallurgy of Zirconium, McGraw-Hill (1955), p. 466

[7] M. Griffith, C.K. Chow, C.E. Coleman, R.A. Holt, S. Sagat, V.F. Urbanic, Effects of Radiation on Materials, 16th Interational Symposium., ASTM, ASTM STP 1175 (1996), p. 1077

[8] V. Perovic, A. Perovic, G.C. Weatherly, L.M. Brown, G.R. Purdy, R.G. Fleck, R.A. Holt, Journal of Nuclear Materials, v. 205(1993), p.251

[9] R.S.W. Shewfelt, L.W. Lyall, D.P. Godin, Journal of Nuclear Materials, v. 125 (1984), p. 228

[10] H. Okamoto, Journal of Phase Equilibria, v. 13 (1992), p.577

[11] R.A. Holt, J. of Nucl. Mat., v. 372 (2008), p. 182

[12] D.G. Franklin, G.E. Lucas, A.L. Bement, Creep of Zirconium Alloys in Nuclear Reactors, ASTM Special Technical Publication 815 (1983), p. 1

[13] W. Evans, P.A. Ross-Ross, J.E. LeSurf, H.E. Thexton, AECL-3982, Paper no. A/CONF.49/A/159 (1971), p. 1

[14] R.A. Holt, M. Griffiths, R.W. Gilbert, J. of Nucl. Mat., v. 149 (1987), p. 51

[15] A. Akhtar, J. of Nucl. Mat., v. 47 (1973), p. 79

[16] E. Tenckhoff, J of ASTM Int., v. 2 (2005), p. 119

[17] A. Salinas-Rodriguez., M.G. Akben, J.J. Jonas, E.F. Ibrahim, Canadian Metallurgical Quarterly, v. 24 (1985), p. 259

[18] M. Griffiths, C.K. Chow, C.E. Coleman, R.A. Holt, S. Sagat, V.P. Urbanic, AECL Repot Series, AECL-10844 (1993), p. 1

[19] R. Dutton, AECL Report Series, AECL-10158, COG -90-49 (1990), p. 1

[20] L.M. Howe, AECL Report Series, AECL-1484 (1962), p.1

[21] A.R. Causey, C.H. Woo, R.A. Holt, J. of Nucl. Mat., v. 159 (1988), p. 225

[22] V. Fidleris, J. of Nucl. Mat., v. 159 (1988), p. 22

[23] C.H. Woo, U.M. Gosele, J. of Nucl. Mat., v. 119 (1983), p. 219

[24] C.H. Woo, J. of Nucl. Mat., v. 159 (1988), p. 237

[25] C.H. Woo, Proceedings of the international conference: Materials for Nuclear Reactor Core Applications, v.1 (1987), p.65

[26] R.A. Holt, J. of Nucl. Mat., v. 159 (1988), p. 310

[27] R.A. Holt, A.R. Causey, J. of Nucl. Mat., v. 335 (2004), p. 529

[28] W.B. Li, J.L. Henshall, R.M. Hooper, K.E. Easterling, Acta Metal. Mater., v. 39 (1991), p. 3099

[29] P.M. Sargent, M.F. Ashby, Scr. Mater., v. 16 (1982), p. 1415

[30] H. J. Frost and M. F. Ashby, Deformation-Mechanism Maps, Pergamon Press, Oxford (1982)

[31] Argon A.S., *Scripta Met*., v.4 (1970), p.1001

[32] Hull D., Bacon D.J., "*Introduction to dislocations*", Fourth edition (2005), Elsevier Butterworth-Heinemann, Oxford (England)

[33] U.F. Kocks, A.S. Argon, M.F. Ashby, Prog. Mat. Sci., v. 19 (1975), p. 1

[34] V. Fidleris, J. of Nucl. Mat., v. 36 (1970), p. 343

[35] E.R. Gilbert, B. Mastel, Trans. American Nucl. Soc., v. 12(1969), p. 132

[36] E.R. Gilbert, NE.E. Harding, Irradiation Effects in Structural Alloys for Thermal and Fast Reactors, ASTM, STP 457 (1969), p. 17.

[37] V. Fidleris, J. of Nucl. Mat., v. 36 (1970), p. 343

[38] V. Fidleris, Atomic Energy Review., v. 13 (1975), p. 51

[39] AC Fischer-Cripps, "*Nanoindentation*" (2nd edition), Springer (2004), New York, p. 27

[40] B. Bhushan, B.K. Gupta, "Handbbok of Hard Coatings - Deposition Technologies, Properties and Applications", (Bunshah R.F. Ed), Noyes Publications (2001), New Jersey, USA, p. 550

[41] K. L. Johnson, J. Mech. Phys. Solids, v. 18 (1970), p. 115

[42] N.A. Fleck, G.M. Mullar, M.F. Ashby, J.W. Hutchinson, Acta Metall. Mater., v.42 (1994), p. 475

[43] W.J. Poole, M.F. Ashby, N.A. Fleck, Scripta Metall. Mater. v.34 (1996), p. 559

[44] W. D. Nix, H. Gao, J. Mech. Phys. Solids, v. 46 (1998), p. 411

[45] V. Bhakhri and R. J. Klassen, J. Mater. Sci., v. 41 (2006), p. 2249

[46] A. A. Elmustafa, D.S. Stone, Materials Letters, v. 57 (2003), p. 1072

[47] A. A. Elmustafa, D.S. Stone, Mater. Sci. Eng, A, v. 358 (2003), p. 1

[48] A. A. Elmustafa, D.S. Stone, J. Mech. Phys. Solids, v. 51 (2003), p.357

[49] B. Bose and R. J. Klassen, Mat. Sci. and Eng. A., v. 500 (2009), p.164

[50] V. Bhakhri and R. J. Klassen, Scripta Mater., v. 55 (2006), p. 395

[51] M.F. Ashby, Phil. Mag., v. 21 (1970), p. 399

[52] B.J. Diak, K.R. Upadhyaya, S. Saimoto, Prog. Mater. Sci., v. 43 (1998), p. 223

[53] S. Saimoto, M.S. Duesbery, Acta Metall., v. 32(1984), p. 147

[54] D. Tabor, Microindentation Techniques in Material Science and Engineering (edited by P.J. Blau and B. R. Lawn),

[55] W.R. Newson, B.J. Diak, S. Saimoto, Thin Films: Stresses and Mechanical Properties VI, MRS Publications,Warrendale, PA, USA, v. 436 (1997), p. 359

[56] M. Kuroda, D. Setoyama, M. Uno, S. Yamanaka, Journal of Alloys and Compounds, v. 368 (2004), p. 211

[57] T.R.G. Kutty, C. Ganguly, J. of Nucl. Mat., v. 182(1991), p. 258

[58] T.R.G. Kutty, C. Ganguly, J. of Nucl. Mat., v. 27(1992), p. 908

[59] T.R.G. Kutty, C. Ganguly, J. of Nucl. Mat., v. 207(1993), p. 345

[60] C. Robertson, S. Poissonnet, L. Boulanger, J. of Mat. Research, v.13 (1998), p. 2123

[61] W. Zielinski, H. Huang, W.W. Gerberich, J. of Mat. Research, v.8 (1993), p. 1300

[62] W. Zielinski, H. Huang, S.K. Venkataraman, W.W. Gerberich, Phil. Mag., v.72 (1995), p. 1221

[63] P.A. Ross-Ross, V. Fidleris, D.E. Fraser, Canadian Metallurgical Quarterly, v. 11 (1972), p. 101

[64] P.A. Ross-Ross, W. Evans, W.J. Langford, Atomic Energy of Canada Ltd Research Report, AECL-4262 (1972), p. 1

[65] A.R. Causey, V. Fidleris, S.R. MacEwen, C.W. Schulte, Influence of Radiation on Material Properties: 13th Intl. Symp. (1987), p. 54

[66] A.R. Causey, A.G. Norsworthy, C.W. Schultes, Can. Metall. Quart., v. 24 (1984), p. 207

[67] N. Christodoulou, P.A. Turner., E.T.C. Ho, C.K. Chow, M.R. Levi, Metall. and Mat. Trans. A., v. 31A (2000), p. 409

[68] N. Christodoulou, A.R. Causey, r.a. Holt, C.N. Tomé, N. Badie, R.J. Klassen, R. Sauvé, C.H. Woo, Zirconium in the nuclear industry: Eleventh Int. Symp.(1996), p. 518

[69] B.S. Rodchenkov, A.N. Semenov, Nucl. Eng. And Design, v. 235 (2005), p. 2009

[70] E.F. Ibrahim, J. of Nucl. Mat., v. 101 (1981), p. 1

[71] E.F. Ibrahim, R.A. Holt, J. of Nucl. Mat., v. 91 (1980), p. 311

[72] R.A. Holt, N. Christodoulou, A.R. Causey, J. of Nucl. Mat., v. 317 (2003), p. 256

[73] D.D. Himbeault, C.K. Chow, M.P. Plus, Metall. And Mater. Trans. A, v. 25 (1994), p. 135

[74] R.A. Holt, G.A. Bickel, N. Christodoulou, J. of Nucl. Mat., v. 373 (2008), p. 130

[75] K.L. Murty, Mat. Sci. and Eng., v. 70 (1985), p.169

[76] K.L. Murty, S. Hussien, Y.H. Jung, Scripta Metallurgica, v. 19 (1985), p. 1985

[77] M.D. Mathew, K.L. Murti, Proceedings of the 10^{th} Intl. Conf. on Nucl. Engg, ICONE 10 (2002), p. 227

[78] S.T. Mahmood, S.A. Hussien, P.S. Godavarti, K.L. Murty, Effects of Radiation on Materials: 15^{th} Int. Symp., ASTM, STP 1125 (1992), p. 337

[79] M. Nakatsuka, M. Nagai, J. of Nucl. Sci. And Tech., v. 24 (1987), p. 832

[80] M. Nakatsuka, M. Nagai, J. of Nucl. Sci. And Tech., v. 24 (1987), p. 906

Chapter 3

3 Effect of ion irradiation and indentation depth on the kinetics of deformation during micro-indentation of Zr-2.5%Nb pressure tube material at 25°C*

This chapter provides descriptions of the foremost series of investigations where the indentation depth dependence of the deformation parameters of Zr-2.5%Nb pressure tube material was determined and the effect of irradiation on these parameters was studied by performing one hour constant load indentation creep tests at 25°C.

3.1 Introduction

Zr-2.5%Nb pressure tubes have proven to be very reliable components of the fuel-channel assemblies of CANDU (CANadian Deuterium Uranium) nuclear reactors however the inside surface of these tubes can become scratched during service and the local stress ahead of these scratches can be high enough to require the early removal of a pressure tube from the reactor core. It is therefore necessary to be able to predict the local creep rate ahead of sharp scratches on the inside surface of these pressure tubes in order to make accurate flaw assessments. While the thermal creep characteristics of Zr-2.5%Nb pressure tube material at low applied stress levels have been reported [1,2] the creep rate under high magnitude multi-axial stress conditions and the effect of neutron irradiation hardening on the thermal creep rate has not been thoroughly studied. The research presented in this paper uses pyramidal micro-indentation creep tests performed at 25°C to simulate the creep rate ahead of a scratch on the inside surface of a Zr-2.5%Nb

---

* A version of this chapter was published in the Journal of Nuclear Materials, Volume 399, Issue 1, 1 April 2010, Pages 32–37.

CANDU pressure tube. The effect of indentation depth and ion irradiation hardening (as a simulation of neutron irradiation hardening) on the mechanism of indentation creep deformation is investigated. Some important underlying principles pertaining to this investigation are described below.

3.1.1 Indentation creep tests to simulate creep at scratches

Scratches on the inside surface of CANDU pressure tubes, arising from refueling operations and rubbing between fuel bundle bearing pads and the inside wall of the pressure tube, often have similar depth and sharpness to pyramidal micro-indentations. Pyramidal micro-indentation creep tests therefore offer a way to simulate the creep deformation around such scratches. Constant-force micro- and nano-indentation creep tests have been used to study the kinetics of plastic deformation of a variety of materials [3-9] and the results of such tests are usually interpreted in terms of deformation occurring by a mechanism of dislocation glide limited by discrete obstacles distributed throughout the microstructure [10, 11]. Most of the published indentation creep investigations were performed on relatively isotropic material (i.e. fcc metals). The kinetics of high-stress low-temperature indentation creep of mechanically anisotropic materials, such as the extruded and cold-drawn Zr-2.5%Nb pressure tube alloy, has not been reported. This information is not only important for understanding the fundamentals of the indentation creep process but is also important for establishing basic kinetic parameters that can be used in expressions describing the creep rate of material around scratches that have geometrical similarities to pyramidal indentations.

3.1.2 Mechanism of creep deformation ahead of scratches in Zr-2.5%Nb pressure tubes

The combination of very high equivalent stress at the tip of a crack, or surface flaw, in a Zr-2.5%Nb pressure tube and the fact that the service temperature of the tube is low relative to the solidus temperature (T/T_{melt}= 0.14 to 0.17) suggests that thermal creep

ahead of the sharp scratches occurs by a mechanism of dislocation glide at a rate limited by the interaction of the gliding dislocations with discrete obstacles in the microstructure. When deformation occurs by such a mechanism the shear strain rate $\dot{\gamma}$ can be expressed in terms of the yield shear stress τ_{yield}, the effective shear stress τ_{eff} driving the creep process, and the absolute temperature T as [10]

$$\dot{\gamma} = \dot{\gamma}_p \left(\frac{\tau_{yield}}{\mu} \right)^2 e^{-\frac{\Delta G(\tau_{eff})}{kT}} \tag{3.1}$$

Where $\dot{\gamma}_p$ is a constant (approximately equal to10^{11} s^{-1} [10]), μ is the elastic shear modulus, k is Boltzmann's constant and $\Delta G(\tau_{eff})$ is the thermal energy required for a dislocation, subjected to τ_{eff}, to overcome the discrete obstacles. The following general expression for $\Delta G(\tau_{eff})$ has been proposed [10, 11]

$$\Delta G(\tau_{eff}) = \Delta G_0 \left[1 - \left(\frac{\tau_{eff}}{\hat{\tau}} \right)^p \right]^q \tag{3.2}$$

In this equation ΔG_0 is the activation energy of the discrete obstacles, $\hat{\tau}$ is the athermal flow strength of the material, *p* and *q* are constants. ΔG_0 and the constants *p* and *q* are characteristic of the particular dislocation-obstacle interaction that governs the creep rate and, in the case of Zr-2.5%Nb pressure tubes, may depend upon temperature, indentation depth, and the degree of neutron irradiation hardening. The study described in this paper addresses the dependence of ΔG_0 upon indentation depth and ion irradiation.

3.1.3 Indentation Size Effect

The indentation hardness of metals decreases with increasing indentation depth from 0.1 to about 10 μm. The hardness then remains relatively constant with further increasing depth. This depth dependence of the indentation hardness is widely thought to result from

the fact that a higher local dislocation density is necessary to accommodate the larger plastic strain gradients associated with sub-micrometer deep indentations [12-17]. While the indentation depth dependence of hardness has been studied extensively for relatively isotropic fcc metals, it has not been thoroughly investigated for mechanically anisotropic metals such as the highly textured Zr-2.5%Nb pressure tube alloy. In this study we perform indentation tests at depths from 0.1 to 2.0 μm to assess the indentation size effect on the indentation stress of the extruded and cold-drawn Zr-2.5%Nb pressure tube alloy before and after one hour indentation creep testing. In so doing we hope to gain insight into the indentation depth dependence of the kinetics of dislocation motion in this material when subjected to high-level multi-axial indentation stress for an extended time at 25^{o}C.

3.1.4 Ion irradiation to simulate neutron irradiation

The role of neutron irradiation as a source for the production of point defects and nanometer-scale dislocation loops and the result of these defects on increasing the yield stress of the Zr-2.5%Nb alloy is well documented [18-26]. The use of proton- and electron-irradiation to simulate the microstructural damage resulting from neutron irradiation is also widely reported [27-31]. Previous research has shown that heavy ion bombardment of metals results in the creation of crystallographic damage consisting of dislocation loops similar in size and character to that produced, at a slower rate, by neutron irradiation [32, 33]. In this study we use Zr^{+} irradiation of the Zr-2.5%Nb to simulate the microstructural damage resulting from neutron irradiation without causing significant compositional change to the test material.

3.2 Experimental procedure

3.2.1 Material

Rectangular samples, 8.5 mm long, 8.5 mm wide and 4.0 mm thick, were cut from a non-irradiated Zr-2.5%Nb CANDU pressure tube. The general chemical composition of this

alloy is: 2.5 – 2.7 wt% Nb, 1100-1200 ppm O, ~ 1000 ppm Fe, < 55 ppm N, < 16 ppm H, and balance Zr [34]. The tube was fabricated by 11:1 extrusion of an annular billet at 720^{o}C followed by 27% cold-drawing at room temperature followed by a 24 hour stress relief autoclave treatment at 400^{o}C [1,35]. The microstructure of the tube consists of hcp α-Zr grains, elongated in the axial direction of the tube, interspersed by a thin discontinuous layer of Nb-rich bcc β precipitates. The α grains have average dimensions of about 0.2, 1.0 and 5.0 μm in the radial, hoop and axial directions of the pressure tube respectively. The α grains are textured with the majority of the basal plane normals aligned along the hoop direction of the tube [36]. The Radial-Normal (RN) surface, relative to the radial direction of the pressure tube, of each sample was prepared by mechanical grinding and polishing followed by chemical polishing. The average roughness of the final polished surface was about ± 8 nm as measured with atomic force microscopy. The RN plane was chosen as the surface upon which to perform the micro-indentation creep tests since it is the same orientation as the inside surface of a Zr-2.5%Nb pressure tube and, therefore, the same surface that becomes scratched during service.

3.2.2 Zr^{+} ion irradiation

Some of the polished samples were exposed to 8.5 MeV Zr^{+} ions to introduce irradiation damage to the material. The ion irradiation was performed in vacuum in the Tandetron 1.7 MV tandem ion accelerator at the University of Western Ontario (London, ON). Monte Carlo simulations carried out with the SRIM software indicate that the maximum interaction of the Zr^{+} ions with the Zr 2.5%Nb alloy occurs at a depth between 2.0 and 2.5 μm (Figure 3.1). One group of samples was exposed to a relatively low dosage of Zr^{+} ions, corresponding to a maximum of about 5 displacements per atom (dpa) at a depth of between 2.0 and 2.5 μm while another group of samples was exposed to a higher dosage corresponding to a maximum damage of about 30 dpa.

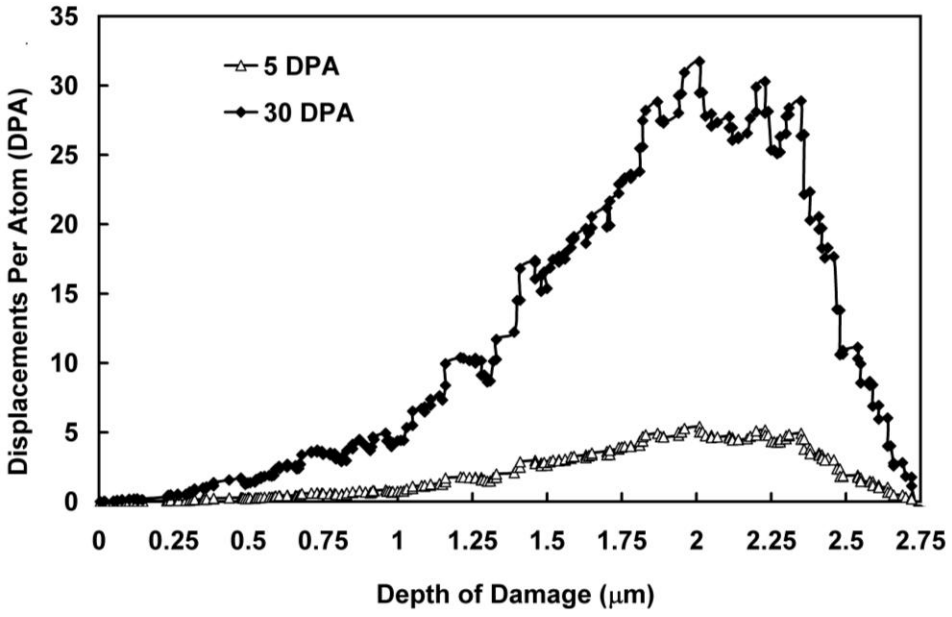

Figure 3.1: Calculated irradiation damage, in units of displacement per atom (dpa), resulting from 8.5 MeV Zr^+ ions versus depth in the irradiated Zr-2.5%Nb sample. One sample was exposed to a relatively low dosage of Zr^+ ions corresponding to about a maximum of 5 dpa while another group of sample was exposed to a higher dosage corresponding to a maximum of about 30 dpa at a depth of 2.0 to 2.5 μm.

3.2.3 Micro-indentation creep tests

Constant-force Berkovich indentation creep tests were performed at 25°C on the polished RN surface of the Zr-2.5%Nb samples using an instrumented nano-/micro-indentation testing platform made by Micro Materials ltd (Wrexham, UK). Indentation creep tests were carried out at initial indentation depths of h_0 = 0.1, 0.5, 1.0 and 2.0 μm for both the non-irradiated and the ion-irradiated samples. For each test the indentation force (F) was slowly applied until the desired h_0 was reached. F was then held constant for one hour while the indentation depth h was continuously recorded. Between **7** and 10 indentation creep tests were performed at each h_0 on the non-irradiated, the 5 dpa, and the 30 dpa Zr^+ irradiated samples.

3.2.4 TEM investigations

Electron transparent foils, of about 500 nm thicknesses, were extracted by focused ion beam (FIB) milling from within the indentation plastic zone of 500 nm deep crept indentations from the non-irradiated and the ion-irradiated samples (Figure 3.2). The FIB milling was performed using a LEO XB1540 dual beam FIB/SEM with 30 keV Ga^+ ions of 1nA current. The final 100-150 nm thickness was slowly removed with a Ga^+ ion current of 50pA. Parallel beam transmission electron microscopy (TEM) was performed on the samples with a PHILIPS CM12 microscope operating at 120 kV.

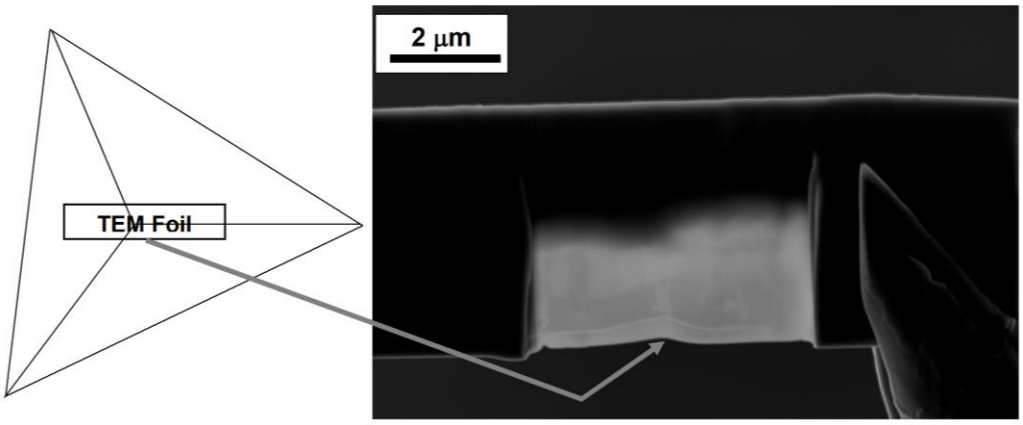

Figure 3.2: Schematic illustration of the orientation of a TEM foil extracted, by FIB milling, from an as-crept indentation made in the Zr-2.5%Nb test material. The SEM image shows the extracted foil with the profile of the indentation clearly visible beneath the deposited Pt protective later.

3.3 Results and Discussion

The average indentation stress σ_{ind} was calculated as:

$$\sigma_{ind} = \frac{F}{24.5Ch^2} \tag{3.3}$$

Where, $24.5h^2$ is the projected area of an ideal Berkovich indentation and C is a constant that accounts for the effect of sink-in and pile-up on the projected indentation area. C was obtained from SEM measurement of the projected area of indentations of various depths.

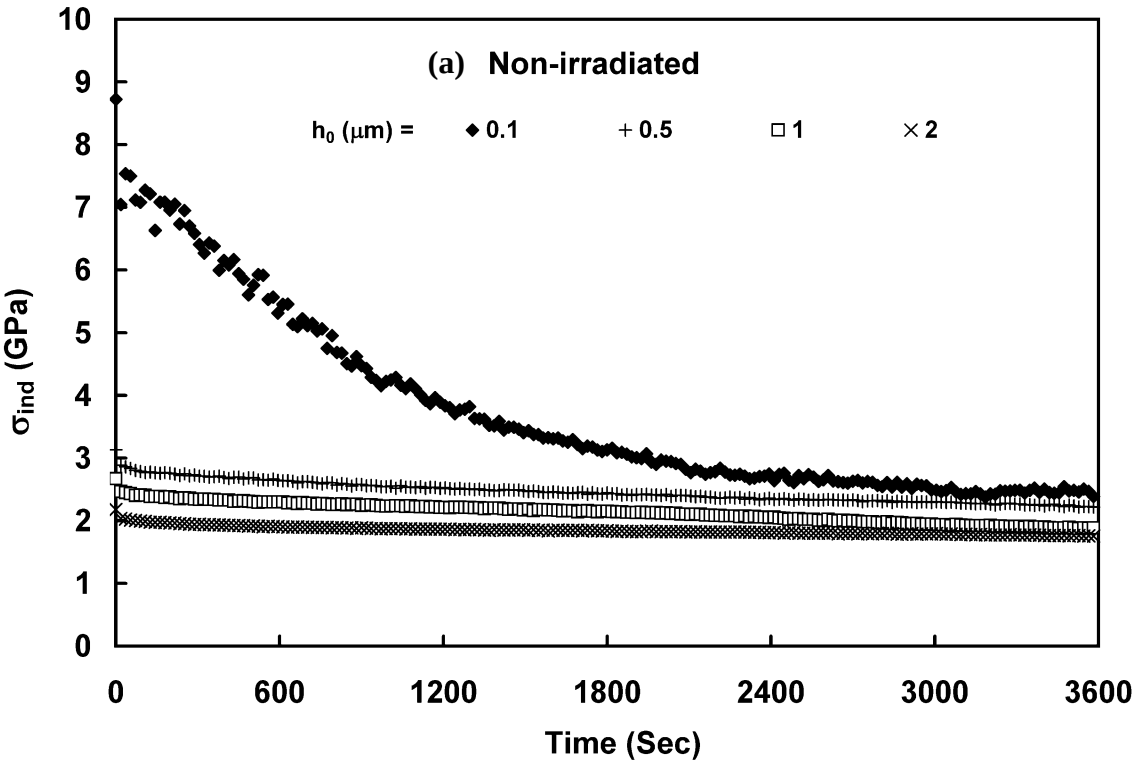

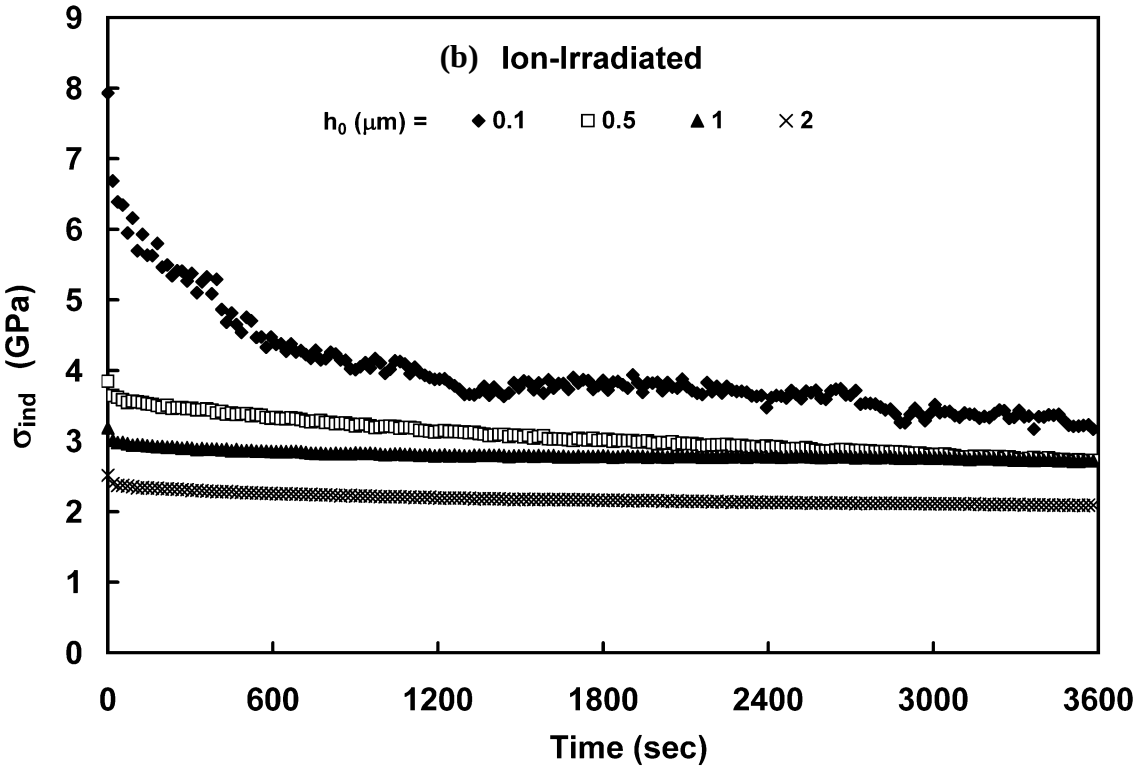

Figure 3.3: Typical average indentation stress σ_{ind} versus time plots during the indentation creep tests performed on (a) Non-irradiated and (b) 30 dpa Zr^{+} irradiated Zr-2.5%Nb samples performed at different values of h_0. Although the trend is similar for all samples, the indentation stress σ_{ind} values are higher for the irradiated samples.

The average indentation strain rate $\dot{\varepsilon}_{ind}$ is related to the instantaneous indentation depth h and indentation velocity $\dot{h}$ as:

$$\dot{\varepsilon}_{ind} = k\left(\frac{\dot{h}}{h}\right) \tag{3.4}$$

where k is a material constant that, due to the geometrical self-similarity of the pyramidal indentation, is independent of h over the depth range considered in this study. Since k

remains constant, we set it equal unity and refer to $\dot{\varepsilon}_{ind}$ as the apparent average indentation strain rate.

During the constant-*F* stage of the micro-indentation tests, *h* increases with time due to creep deformation and this result in decreasing σ_{ind} (Figure 3.3 (a,b)). In Figure 3.4 the initial indentation stress $\sigma_{ind_{t=0}}$ is plotted versus the initial indentation depth h_0, prior to creep testing. Power-law functions of indentation depth fitted to the data show that $\sigma_{ind_{t=0}}$ of the Zr-2.5%Nb material in this study is a function of both the indentation depth and the level of Zr^+ ion irradiation.

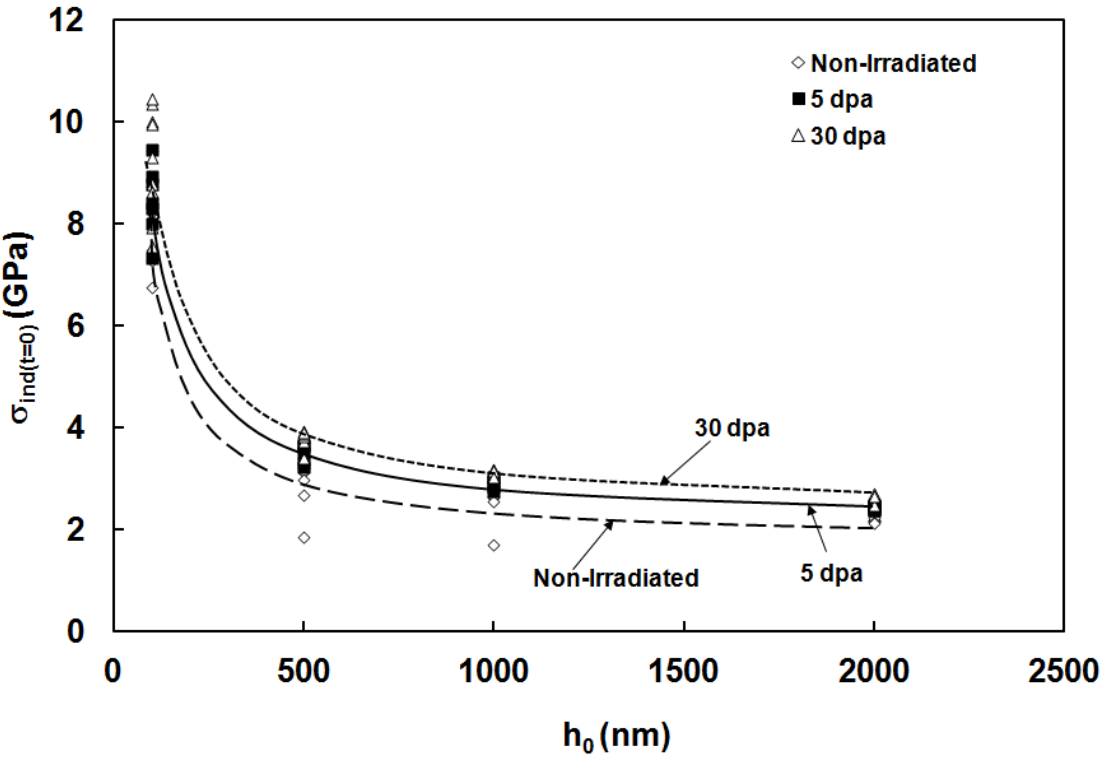

Figure 3.4: Variation in initial indentation stress, i.e. indentation stress at the beginning of creep tests, $\sigma_{ind(t=0)}$ with initial indentation depth, h_0 for three different sample conditions (as received, 5 dpa and 30 dpa). $\sigma_{ind(t=0)}$ decreases with h_0 and increases with irradiation damage.

Since the strain gradient in the indentation plastic zone increases inversely with the indent size (section 3.3), σ_{ind} often reaches a magnitude of a few percent of the Young's modulus, i.e. almost the ideal strength of the indented material, when the indentation depth is less than one micrometer. David Tabor has shown that for deep indentations, where indentation size effects are not a factor, σ_{ind} is a function of the uniaxial yield stress for most materials ($\sigma_{ind} \approx 3\sigma_{yield}$ [37]). Using this empirical correlation, $\sigma_{ind_{t=0}}$ from the deepest indentations in our study (depth 2 μm) corresponds to a uniaxial yield stress that is similar in magnitude to the reported value for the cold-worked Zr-2.5%Nb pressure tube alloy [38-40].

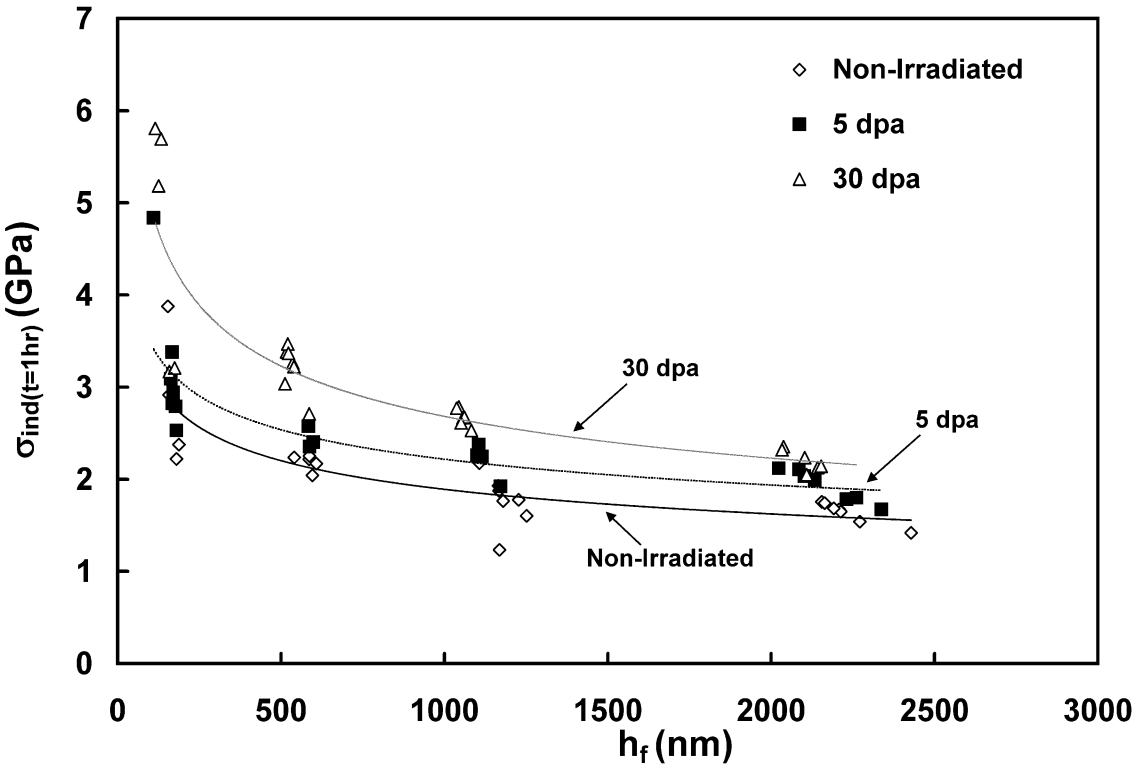

Figure 3.5: Indentation stress at the end of the one hour constant *F* creep tests $\sigma_{ind_{t=1hr}}$ versus final indentation depth, h_f plot for the three different sample conditions (as received, 5 dpa and 30 dpa). For all cases the 30 dpa Zr^+ irradiated sample has the highest final indentation stress. The value of $\sigma_{ind_{t=1hr}}$ also decrease with increasing indentation depth.

In Figure 3.5 the indentation stress at the end of the constant-*F* stage, $\sigma_{ind_{t=1hr}}$ is plotted against the final indentation depth h_f. The plot shows that σ_{ind} at the end of the creep tests, i.e. after significant creep deformation has occurred, still displays dependence upon indentation depth and upon the level of Zr^+ ion irradiation. This suggests that, even after 1 hr recovery under constant *F* conditions, the dislocation density is still higher for the shallow indentation compared to the deep indentation.

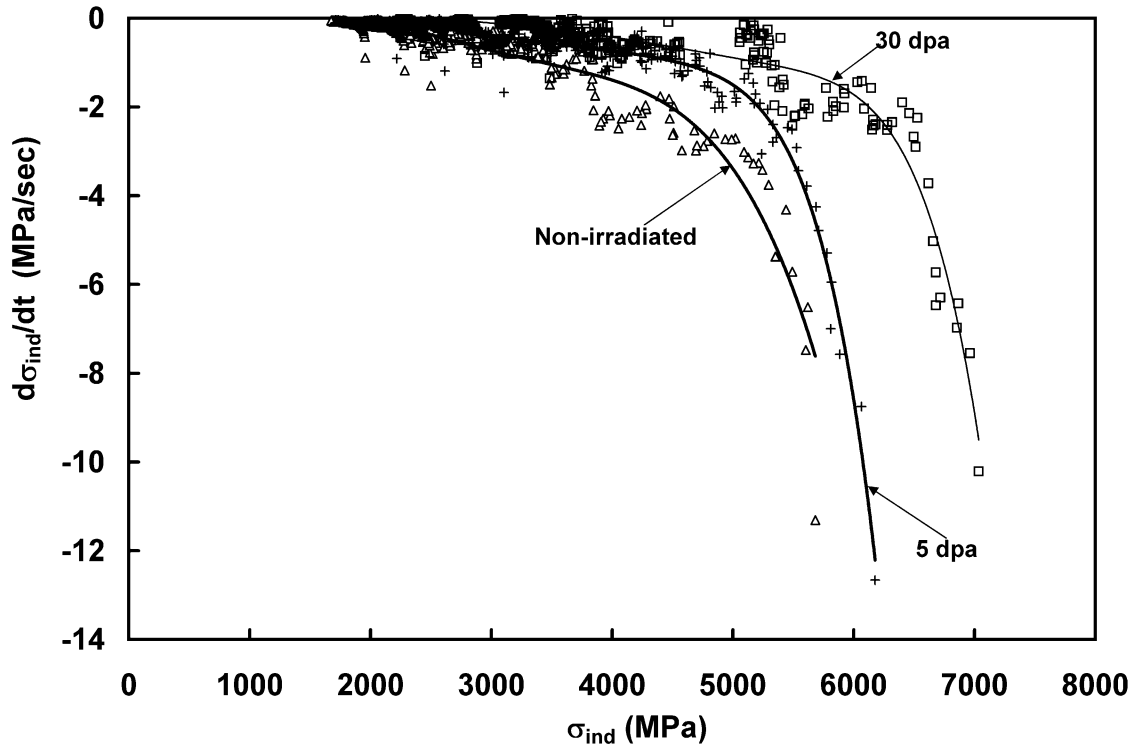

Figure 3.6: The rate of change of indentation stress, $\partial\sigma_{ind}(t)/\partial t$, i.e the slope of the curves in Figure 3.3, versus σ_{ind} for the three different sample conditions (as received, 5 dpa and 30 dpa). For all cases the shape of the curve is clearly dependent upon the level of ion irradiation and data from tests performed at different indentation depths lie on essentially the same curves.

Figure 3.6 shows a plot of the rate of change of indentation stress, $\partial\sigma_{ind}(t)/\partial t$, i.e the slope of the curves in Figure 3.3, versus σ_{ind}. While the shape of the curves is clearly dependent upon the level of ion irradiation, the data from tests performed at different indentation depths lie on essentially the same curve. This indicates that while the indentation creep behaviour of the material depends upon the level of ion irradiation it is not dependent upon indentation depth over the depth range considered in this study (0.1 μm < *h* < 2.0 μm).

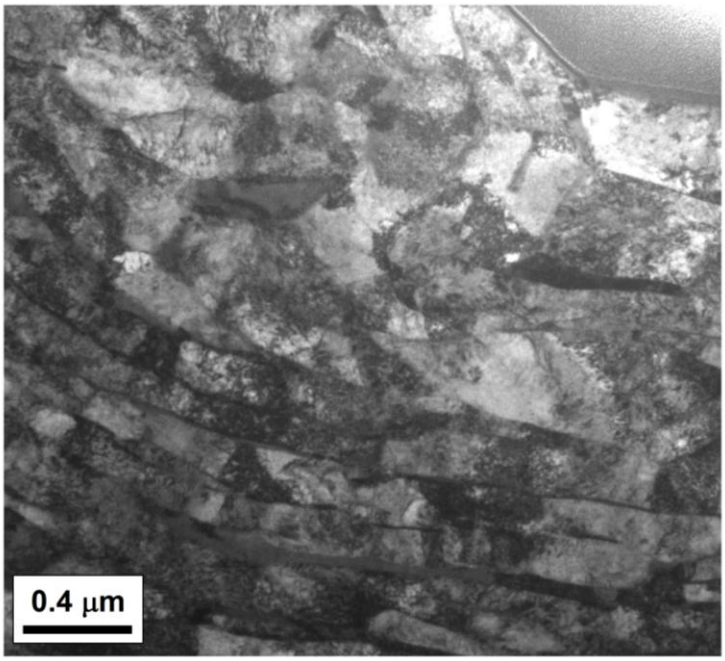

Figure 3.7: TEM image of an as-crept indentation plastic zone in the non-irradiated Zr-2.5%Nb sample. A very high, but inhomogeneous, dislocation distribution exists everywhere in the sample (including far from the indentation). This dislocation distribution is therefore attributed to the 27% cold drawing stage of the pressure tube fabrication.

Figures 3.7 and 3.8 show TEM images of the indentation plastic zone of a non-irradiated and a 30 dpa ion irradiated sample. Both samples display elongated α phase grains with high dislocation density that is characteristic of the extrusion/cold-drawing fabrication route of the test material. However, the ion irradiated sample also displays large regions of mottled "salt and pepper" contrast. Previous investigations have shown that small, less than 5 nm diameter, dislocation loops formed in Zr-2.5%Nb as a result of proton irradiation at 77^{o}C [31]. The mottled contrast displayed in Figure 3.8 is very likely to be diffraction contrast resulting from a uniform distribution of small dislocation loops resulting from the Zr^{+} ion irradiation.

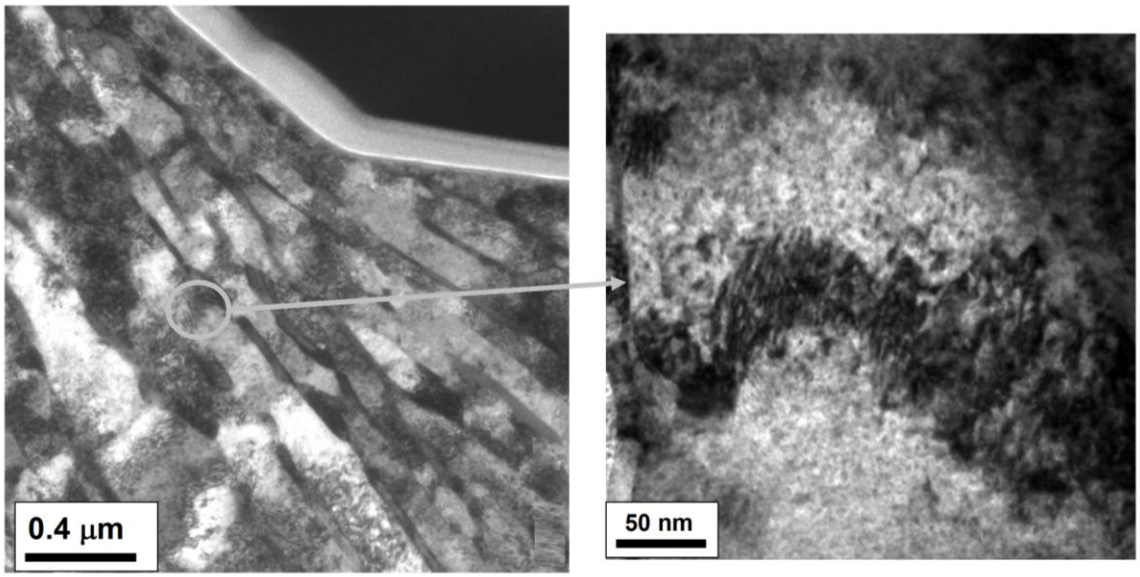

Figure 3.8: TEM image of the as-crept indentation plastic zone in a 30 dpa Zr^{+} irradiated Zr-2.5%Nb sample. The higher magnification inset displays large regions of mottled "salt and pepper" contrast which was not observed in the non-irradiated sample (Figure 3.7) and is therefore attributed to diffraction contrast resulting from a uniform distribution of small dislocation loops resulting from the Zr^{+} ion irradiation. The sizes of the dislocation loops at room temperature are expected to be less than 5nm [31].

The one hour constant-force indentation creep tests provide data from which σ_{ind} and $\dot{\varepsilon}_{ind}$ can be calculated as a function of time using Equations 3.3 and 3.4. We have used these data to determine the following expressions for the equivalent indentation shear stress τ_{ind}, the equivalent effective indentation shear stress τ_{eff} and the apparent equivalent indentation shear strain rate $\dot{\gamma}_{ind}$ [11]:

$$\tau_{ind} = \frac{\sigma_{ind}}{3\sqrt{3}} \qquad \tau_{eff} = \frac{\sigma_{ind} - \sigma_{ind\,t=1hr}}{3\sqrt{3}} \text{ and } \dot{\gamma}_{ind} = \sqrt{3}\dot{\varepsilon}_{ind} = \frac{\sqrt{3}\dot{h}}{h} \tag{3.5}$$

$\Delta G(\tau_{eff})$, the thermal energy required for a dislocation subjected to a shear stress τ_{eff} to overcome an obstacle of strength ΔG_0, was calculated by fitting Equation 3.1 to the τ_{ind}, τ_{eff} and $\dot{\gamma}_{ind}$ data.

The activation energy ΔG_0 of the obstacles that limit the dislocation glide, and hence the indentation creep rate, was determined by extrapolating the $\Delta G(\tau_{eff})$ versus τ_{eff} trends obtained from each indentation creep test to $\tau_{eff} = 0$. Figure 3.9 shows ΔG_0 plotted as a function of final indentation depth h_f. ΔG_0 does not change with indentation depth for the non-irradiated sample. This is in agreement with what has been previously reported for ΔG_0 of Au and Al alloys during indentation creep at 25^{o}C [5, 6].

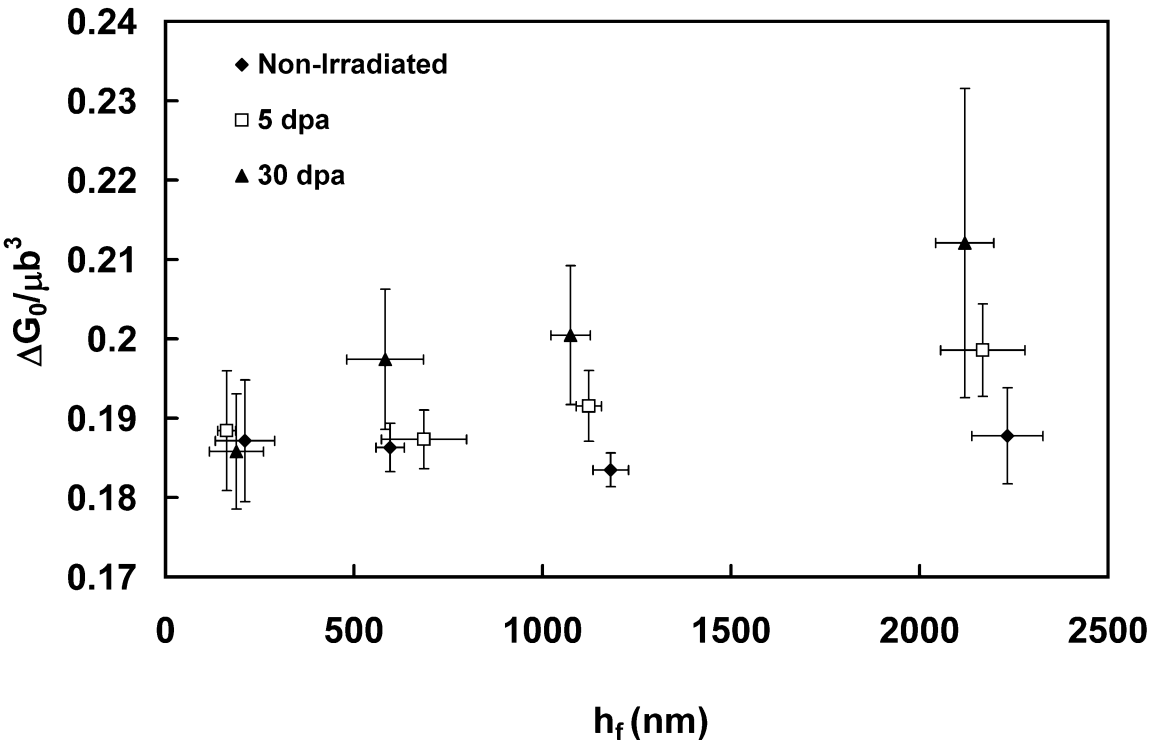

Figure 3.9: The activation energy ΔG_0 of the obstacles that limit the rate of indentation creep versus final indentation depth h_f. The error bars represent ± one standard deviation of the measured population (sample size between 7 and 10). ΔG_0 is essentially independent of h_f (within the variability of the measured ΔG_0) however its magnitude increases with increasing Zr^+ irradiation damage.

If one considers the data from a specific indentation depth, ΔG_0 increases with increasing ion irradiation damage. The dependence of ΔG_0 upon irradiation damage is shown clearly in Figure 3.10 where the average ΔG_0 data from all the tests performed on the Zr^+ ion irradiated material are plotted versus the calculated dpa level corresponding to the final indentation depth h_f (Table 3.1).

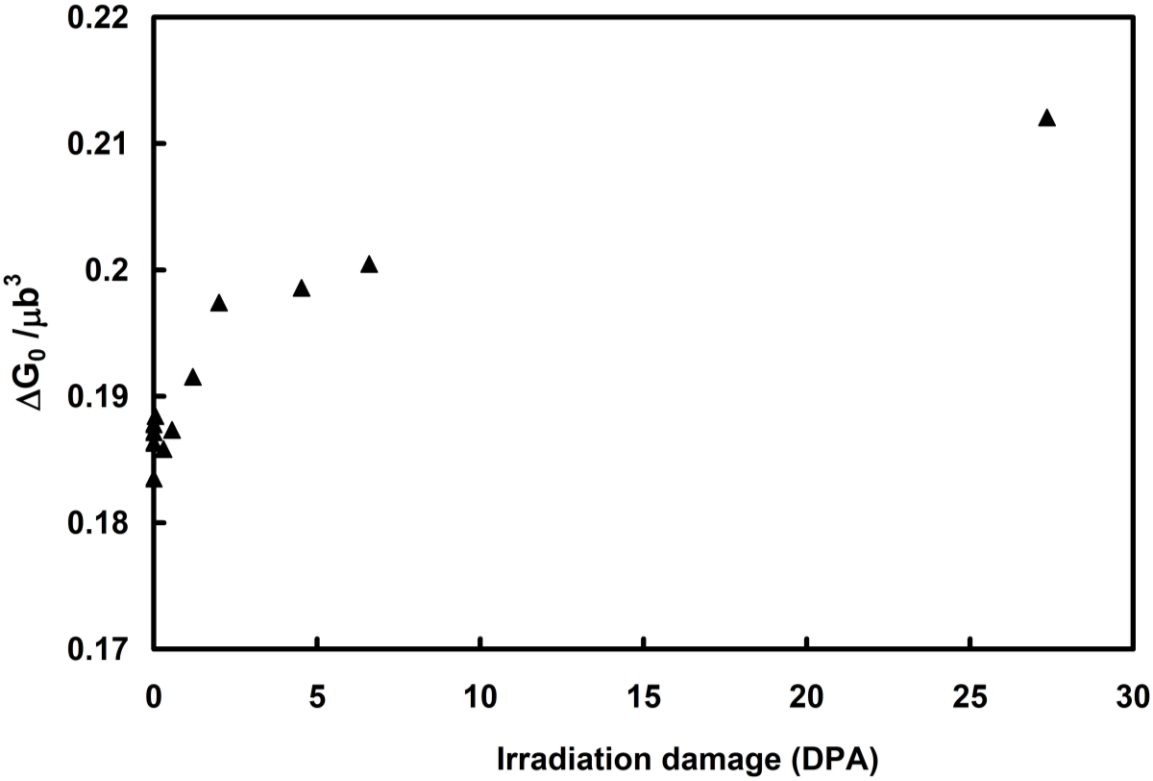

Figure 3.10: The activation energy ΔG_0 of the obstacles that limit the rate of indentation creep versus the calculated dpa at the final indentation depth h_f of each test (Table 3.1). ΔG_0 clearly increases in a nonlinear way with increasing degree of Zr^+ ion irradiation damage.

The TEM observations (Figures 3.7 and 3.8) suggest that the increase in the measured ΔG_0 is related to the small dislocation loops that result in the mottled dark-light contrast in Figure 3.8. It should be noted that ΔG_0 is between 0.185 and 0.215 μb^3. This is of magnitude similar to what is expected for the free energy of "intermediate strength" obstacles to dislocation glide such as dislocation/dislocation interactions [10].

Table 3.1: dpa levels at each of the initial indentation depth, h_0 and their corresponding final indentation depths, h_f for the two kinds of irradiated samples

h_0 (μm)	Calculated dpa at h_0 (5 dpa Zr^+ irradiated sample)	Calculated dpa at h_0 (30 dpa Zr^+ irradiated sample)	5 dpa Zr^+ irradiated sample		30 dpa Zr^+ irradiated sample	
			Avg. h_f (μm)	Approx. dpa at h_f	Avg. h_f (μm)	Approx. dpa at h_f
0.10	0.03	0.18	0.16	0.05	0.19	0.30
0.50	0.23	1.35	0.69	0.56	0.58	2.00
1.00	0.75	4.42	1.12	1.20	1.07	6.60
2.00	5.35	31.35	2.17	4.53	2.12	27.36

3.4 Conclusions

This paper presents the data from a study that uses pyramidal micro-indentation creep tests performed at 25°C on non-irradiated and Zr^+ ion-irradiated Zr-2.5%Nb pressure tube material to simulate the low-temperature creep deformation that drives the time-dependent blunting of scratches in CANDU reactor pressure tubes. The primary findings of this study are:

The indentation hardness (as indicated by the initial average indentation stress $\sigma_{ind\,t=0}$) increased with decreasing indentation depth and increasing levels of Zr^+ ion irradiation. The depth dependence of the indentation stress is consistent with that predicted by the theories that attribute this to the increased density of geometrically necessary dislocations around sub-micrometer deep indentations.

TEM images of the indentation plastic zone in non-irradiated and ion-irradiated samples indicate that the Zr^+ ion irradiation induces regions of mottled contrast, typical of a uniform distribution of nanometer sized dislocation loops, within the microstructure. This is similar to what results from neutron irradiation. We conclude therefore that Zr^+ ion irradiation is an effective way to simulate the crystallographic damage resulting from neutron irradiation in Zr-2.5%Nb.

The activation energy ΔG_0 of the obstacles that limit the rate of dislocation glide during indentation creep was assessed from the measured indentation stress and strain rates. ΔG_0 does not change with indentation depth for the non-irradiated sample and this is in agreement with what was previously reported for ΔG_0 of other ductile metals at 25^oC. ΔG_0 does however increase with increasing levels of Zr^+ ion damage and shows a non-linear relationship with dpa resulting from Zr^+ ion irradiation. The magnitude of the measured ΔG_0 is between 0.185 and 0.215 μb^3. This is similar to what is expected for the free energy of "intermediate strength" obstacles to dislocation glide such as dislocation/dislocation interactions. This suggests that the small dislocation loops shown in the TEM images of indentations made in the irradiated samples become the rate-limiting feature controlling the low temperature creep around scratches in Zr-2.5%Nb pressure tube material.

It should be noted that this study has investigated the effect of prior irradiation hardening on the kinetics of thermal creep deformation occurring, in Zr-2.5%Nb, at very high stress and very low temperature. The resulting data on the effect of irradiation damage on σ_{ind} and ΔG_0 are particularly important for arriving at conservative predictions of the rate of crack tip blunting of scratches in the outboard region of a CANDU pressure tube. This research does not consider the effect of temperature and neutron flux on σ_{ind} or ΔG_0.

3.5 Acknowledgements

The authors wish to thank the Natural Science and Engineering Research Council of Canada (NSERC) and the University Network of Excellence in Nuclear Engineering (UNENE) who provided financial support for this research. The assistance of Dr. T. Simpson of the University of Western Ontario Nanofabrication Laboratory in preparing the TEM foils using focused ion beam milling is gratefully acknowledged. Finally, a special note of thanks to Mr. B. Leitch of the Atomic Energy of Canada Ltd (Chalk River Laboratories) for providing the Zr-2.5%Nb pressure tube material used in this study and providing his continuous support of this project.

3.6 References

[1] N. Christodoulou, P.A. Turner., C.N. Tomé., C.K. Chow, R.J. Klassen, Metall. and Mat. Trans. A., v. 33 (2002), p. 1103

[2] A.R. Causey, A.G. Norsworthy, C.W. Schultes, Can. Metall. Quart., v. 24 (1984), p. 207

[3] V. Bhakhri and R. J. Klassen, J. Mater. Sci., v. 41 (2006), p. 2259

[4] V. Bhakhri and R. J. Klassen, J. Mater. Sci., v. 41 (2006), p. 2249

[5] V. Bhakhri and R. J. Klassen, Scripta Mater., v. 55 (2006), p. 395

[6] B. Bose and R. J. Klassen, Mat. Sci. and Eng. A., v. 500 (2009), p.164

[7] R. J. Klassen, B. J. Diak and S. Saimoto, Mater. Sci. Eng. A , v. 387-389 (2004), p. 297

[8] B. J. Diak and S. Saimoto, Mater. Sci. Eng. A, v. 319-321 (2001), p. 909.

[9] S. Saimoto, B. J. Diak and K. R. Upadhyaya, Mater. Sci. and Eng. A, v. 234-236 (1997), p. 1015.

[10] H. J. Frost and M. F. Ashby, Deformation-Mechanism Maps, Pergamon Press, Oxford (1982)

[11] U.F. Kocks, A.S. Argon, M.F. Ashby, Prog. Mat. Sci., v. 19 (1975), p. 1

[12] W. D. Nix, H. Gao, J. Mech. Phys. Solids, v. 46 (1998), p. 411.

[13] M. F. Ashby, Philos. Mag., v. 21 (1970), p. 399.

[14] Q. Ma, D. R. Clarke, J. Mater. Res., v. 10 (1995), p. 853

[15] H. Li, A. H. W. Ngan, J. Mater. Res., v. 19 (2004), p. 513

[16] W.J. Poole, M.F. Ashby, N.A. Fleck, Scripta Mater., v. 34 (1996), p. 559

[17] A. A. Elmustafa, D. S. Stone, J. Mech. Phys. Solids, v. 51 (2003), p. 357

[18] M. Griffiths, J.F. Mecke, J.E. Winegar, Zirconium in the nuclear industry: Eleventh Int. Symp., ASTM, STP 1295 (1996), p 580

[19] R.A. Holt, M. Griffiths, R.W. Gilbert, J. of Nucl. Mat., v. 149 (1987), p. 51

[20] M. Griffiths, R.W. Gilbert, V. Fidleris, R.P. Tucker, R.B. Adamson, J. of Nucl. Mat., v. 150 (1987), p. 159

[21] M. Griffiths, R.W. Gilbert, C.E. Coleman, J. of Nucl. Mat., v. 159 (1988), p. 405

[22] M. Griffiths, J. of Nucl. Mat., v. 205 (1993), p. 225

[23] M. Griffiths, J. of ASTM Int., v. 5 (2008), p. 1

[24] E. Kohn, M.G. Wright, AECL Research Report, AECL-5810 (1977), p. 1

[25] M. Griffiths, J. of Nucl. Mat., v. 159 (1988), p. 190

[26] M. Griffiths, P.H. Davis, W.G. Davis, S. Sagat, Zirconium in the nuclear industry: Thirteenth Int. Symp., ASTM, STP 1423 (2002), p. 507

[27] M. Griffiths, R.C. Styles, C.H. Woo, F. Philip, W. Frank, AECL Research Report, AECL-10801 (1993), p. 1

[28] C.D. Cann, C.B. So, R.C. Styles, C.E. Coleman, J. Nucl. Mater., v. 205 (1993), p. 267

[29] O.T. Woo, R.M. Hutcheon, C.E. Coleman, Mater. Res. Soc. Symp. Proc., v. 373 (1995), p. 189.

[30] G.J.C. Carpenter, J.F. Watters, J. Nucl. Mater., v 96 (1981), p. 213

[31] C.K. Chow R.A. Holt, C.H. Woo, C.B. So, J. Nucl. Mater., v. 328 (2004), p. 1

[32] C. Heintze, C. Recknagel, F. Bergner, M. Hernández-Mayoral, A. Kolitsch, Nucl. Instruments and Methods in Phys. Res. B, v. 267 (2009), p. 1505

[33] X.T. Zu, M. Atzmon, L.M. Wang, L.P. You, F.R. Wan, G.S. Was, R.B. Adamson, J. of ASTM intl., v. 1(2004), p.741

[34] V. Perovic, A. Perovic, G.C.Weatherly, L.M. Brown, G.R. Purdy, R.G. Fleck, R.A. Holt, J. of Nucl. Mat., v. 205(1993), p.251

[35] V. Perovic, G.C. Weatherly, R.G. Fleck, Can. Metall. Quart., v. 24 (1985), p. 253

[36] M. Griffiths, C.K. Chow, C.E. Coleman, R.A Holt, S. Sagat, V.F. Urbanic, Atomic Energy of Canada Ltd Research Report, AECL-10844 (1993), p. 1

[37] D. Tabor, Microindentation Techniques in Material Science and Engineering (edited by P.J. Blau and B. R. Lawn), ASTM special Publ. (1985), p. 129

[38] N. Christodoulou, P.A. Turner., E.T.C. Ho, C.K. Chow, M.R. Levi, Metall. and Mat. Trans. A., v. 31A (2000), p. 409

[39] A. Salinas-Rodriguez., M.G. Akben, J.J. Jonas, E.F. Ibrahim, Canadian Metallurgical Quarterly, v. 24 (1985), p. 259

[40] B.S. Rodchenkov, A.N. Semenov, Nucl. Eng. And Design, v. 235 (2005), p. 2009

Chapter 4

4 Effect of Zr^+ ion irradiation on the mechanical anisotropy of Zr-2.5%Nb pressure tube material*

In the preceding chapter, the effect of indentation depth and irradiation hardening on the local deformation properties of Zr-2.5%Nb pressure tube material were investigated. However the indentation tests in that study were performed only on RN plane. This chapter includes results from additional indentation tests performed on the AN and TN planes of Zr-2.5%Nb pressure tube for an overall assessment of the mechanical anisotropy and the change in anisotropy due to Zr^+ ion irradiation (as a simulation of neutron irradiation).

4.1 Introduction

Extruded and cold drawn Zr-2.5%Nb pressure tubes, used in CANDU nuclear reactors, are mechanically anisotropic due to the strongly textured hcp α-phase which is the predominant constituent of their microstructure. Extensive mechanical testing has been done to characterize the anisotropy of both the flow stress and the thermal creep properties of these tubes in the non-irradiated condition and, to a much lesser extent, in the neutron irradiated condition [1-16]. Performing a complete characterization of the mechanical anisotropy is made difficult by the fact that these pressure tubes are only about 4 mm thick and it is therefore impossible to construct conventional uniaxial test specimens aligned parallel to the radial (thickness) direction of the tube. Several research groups have attempted to overcome this problem by performing impression/indentation

* A version of this chapter was published in the Journal of Nuclear Materials, Volume 405, Issue 2, 15 October 2010, Pages 138–143. Part of it was presented in NuMat 2010: the Nuclear Materials Conference in Karlsruhe, Germany.

hardness tests on the radial-normal (RN), axial-normal (AN) and transverse normal (TN) planes of Zircaloy pressure tubes to quantified the anisotropy of the yield stress [17 – 22]. The high spatial resolution possible with micro-indentation testing makes this testing technique potentially very useful for assessing the directional anisotropy of the mechanical properties of Zr-2.5%Nb pressure tubes and this technique is used in this study.

An important question related to the mechanical anisotropy of zirconium alloy pressure tubes used in nuclear reactors is the affect of neutron irradiation on the degree of mechanical anisotropy. Impression tests and pyramidal indentation tests performed by Nakatsuka et al [17, 18] and Mahmood et al. [19] have reported that the anisotropy of the yield stress of Zircaloy pressure tubes was reduced by exposure to neutron irradiation. They proposed that this was due to the neutron irradiation induced defects having a larger affect on impeding prismatic dislocation glide compared to pyramidal dislocation glide. To date, no indentation-type tests have been reported which assess the affect of irradiation hardening on the mechanical anisotropy of extruded and cold drawn Zr-2.5%Nb pressure tubes. We address this topic in this study.

In a previous study we have reported the results of Zr^+ ion irradiation (as a simulation of neutron irradiation) on both the depth dependence of the indentation stress and the mechanism of micro-indentation creep of Zr-2.5%Nb pressure tube material at 25^oC [23]. Since the indentation tests in that study were performed only on the RN plane, the effect of Zr^+ ion irradiation on the overall anisotropy of the indentation stress and the indentation creep rate was not studied.

In this study we present results from pyramidal nano-indentation tests performed, at 25^oC, on the RN [23], AN, and TN planes of non-irradiated and Zr^+ ion irradiated Zr-2.5%Nb pressure tube material. The objective of the experiments is to investigate the effect of Zr^+ ion irradiation damage on the anisotropy of the flow stress, including the anisotropy of its indentation depth dependence, and the activation energy of the thermal indentation creep process.

4.2 Experimental Procedure

This study was performed on extruded and cold-drawn Zr-2.5%Nb CANDU pressure tube material supplied by the Atomic Energy of Canada Ltd. The material has a strong crystallographic texture with the majority of the hcp α–phase grains aligned with their (0001) basal plane normal in the transverse (circumferential) direction of the tube (Fig. 4.1). The calculated fraction of basal pole normals aligned in the axial, radial, and transverse directions of the pressure tube are F_A = 0.031, F_R = 0.340, and F_T = 0.624 respectively. The fabrication proceedure, chemical composition and microstucture of the pressure tube is described elsewhere [3,23-25].

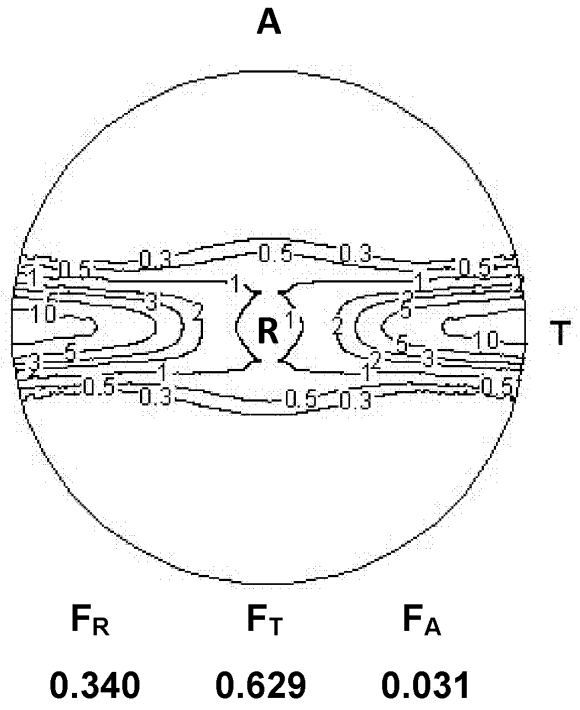

Figure 4.1: (0001) basal pole figure of the extruded and cold drawn Zr-2.5%Nb CANDU pressure tube used in this study. This pole figure was supplied, along with the pressure tube test material, by the Atomic Energy of Canada Ltd. The letters A, T, and R refer to the Axial, Transverse, and Radial directions of the pressure tube. The quantities F_R, F_T, and F_A refer to the calculated basal pole fraction aligned in the radial, transverse and axial directions respectively.

Rectangular samples, 8.5 mm long, 8.5 mm wide and 4.0 mm thick, were cut from the as-received pressure tube. The samples were arranged into three groups; each group had either the AN, RN, or TN planes prepared by mechanical grinding followed by mechanical polishing and then chemical attack polishing. The average roughness of the as-polished surfaces was about ± 8 nm as measured with an atomic force microscope.

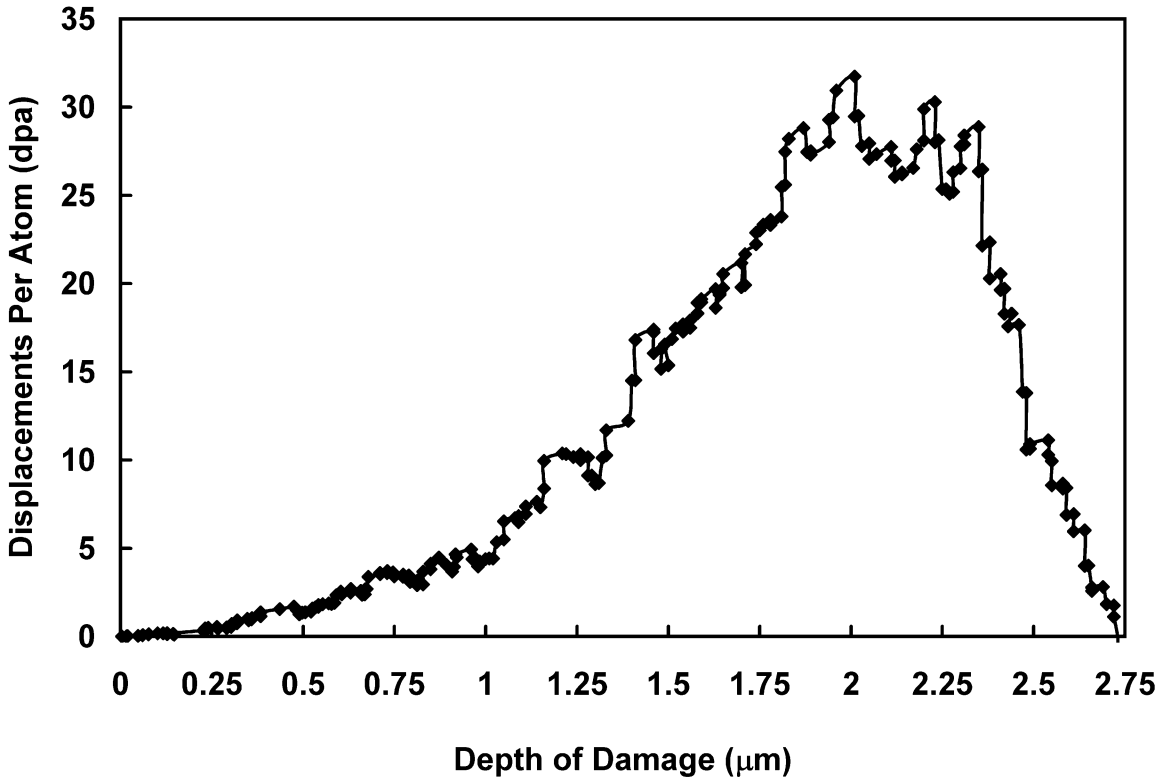

Figure 4.2: Calculated irradiation damage, in units of displacement per atom (dpa), versus depth resulting from irradiation of a Zr-2.5%Nb substrate with 8.5 MeV Zr^+ ions. The samples in this study were exposed to a Zr^+ ion dosage corresponding to about a maximum damage of about 30 dpa at a depth of 2.0 to 2.5 μm.

One polished surface from each of the three sample groups was irradiated with 8.5 MeV Zr^+ ions to a fluence corresponding to a maximum damage of about 30 displacements per

atom (dpa) as calculated from Monte Carlo simulations carried out with the SRIM software. Zr^+ ion irradiation invokes large amounts of irradiation damage into the first several micrometers below the surface without significantly changing the chemical composition of the Zr-2.5%Nb substrate. The microstructure in the first several micrometers below the surface of the Zr^+ ion irradiated sample therefore contains a similar extent of irradiation damage as the microstructure of a Zr-2.5%Nb pressure tube material that was exposed to many years of neutron irradiation at a neutron flux typical to that in the core of a CANDU nuclear reactor. The Zr^+ ion irradiation was performed at 25^{o}C in vacuum in the Tandetron 1.7 MV tandem ion accelerator at the University of Western Ontario (London, ON). Monte Carlo simulations indicate that the maximum interaction of the Zr^+ ions with the Zr-2.5%Nb substrate occurs at a depth between 2.0 and 2.5 μm (Fig. 4.2). Indentation tests were then performed, as described below, within this ion irradiated depth to assess the effect of irradiation damage on the mechanical anisotropy of the Zr-2.5%Nb.

Indentation tests were performed at room temperature (25°C) on the AN, RN, and TN polished surfaces of the non-irradiated and the ion-irradiated samples using an instrumented nano-indentation testing platform (Micro Materials Ltd, Wrexham, UK) with a diamond Berkovich indenter. Indentation tests were carried out at initial indentation depths of h_0 = 0.1, 0.5, 1.0 and 2.0 μm. For each test the indentation force (F) was slowly applied until the desired h_0 was reached. F was then held constant for one hour while the indentation depth h was recorded at 18 second intervals. The indentation depth increased, due to creep, over the course of the one hour test. The average indentation stress was calculated as

$$\sigma_{ind} = \frac{F}{24.5Ch^2} \tag{4.1}$$

Where, $24.5h^2$ is the projected area of an ideal Berkovich indentation, C is a constant that accounts for the effect of sink-in and pile-up on the projected indentation area which was obtained from SEM measurement of the actual projected area of indentations of various depths. The pyramidal Berkovich indentation geometry is geometrically self-

similar in that the width D of the indentation is directly proportional to the indentation depth h. This implies that: i) the average indentation strain must be a direct function of D/h and therefore remains constant regardless of h for a Berkovich indentation, and ii) the average indentation strain rate must be a direct function of $\dot{h}/h$ [26, 27]. We therefore express the apparent average indentation creep rate as

$$\dot{\varepsilon}_{ind} = \frac{\dot{h}}{h} \tag{4.2}$$

Between 7 and 10 indentation creep tests were performed at each level of h_0 on each sample. The indentation load and depth data obtained from the tests were used to calculate σ_{ind} and $\dot{\varepsilon}_{ind}$ using Eqs. 4.1 and 4.2.

4.3 Results and Discussion

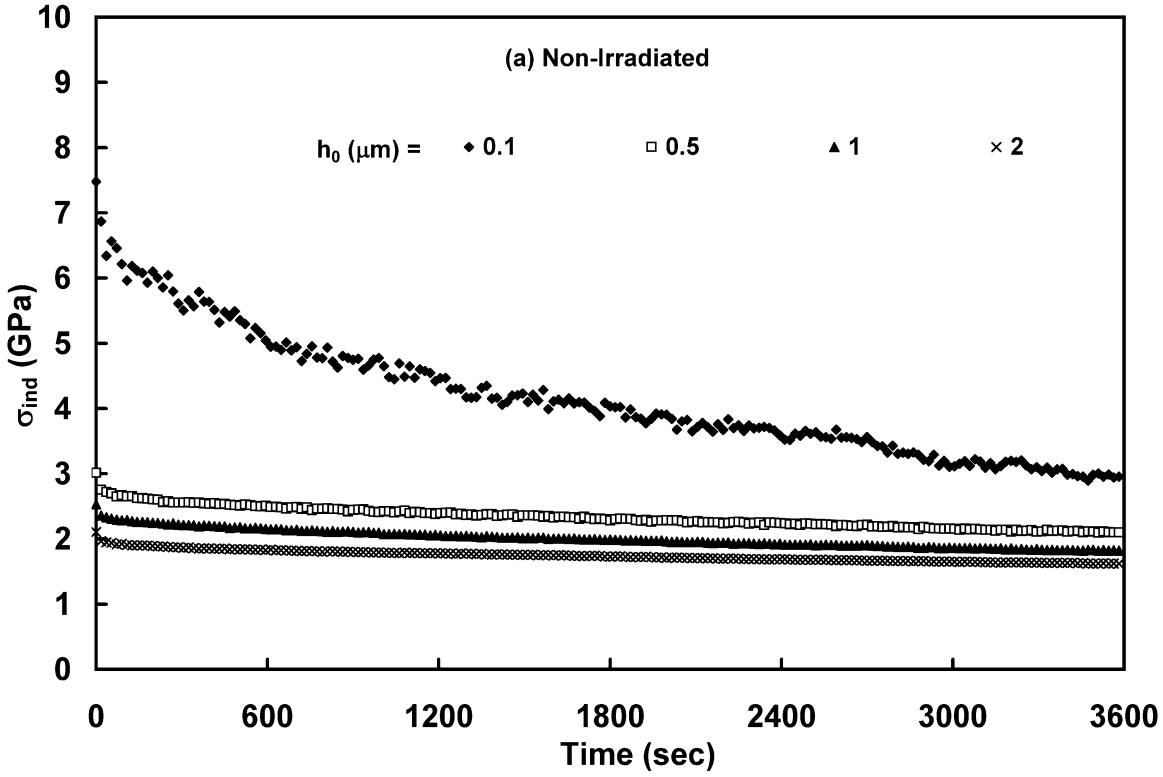

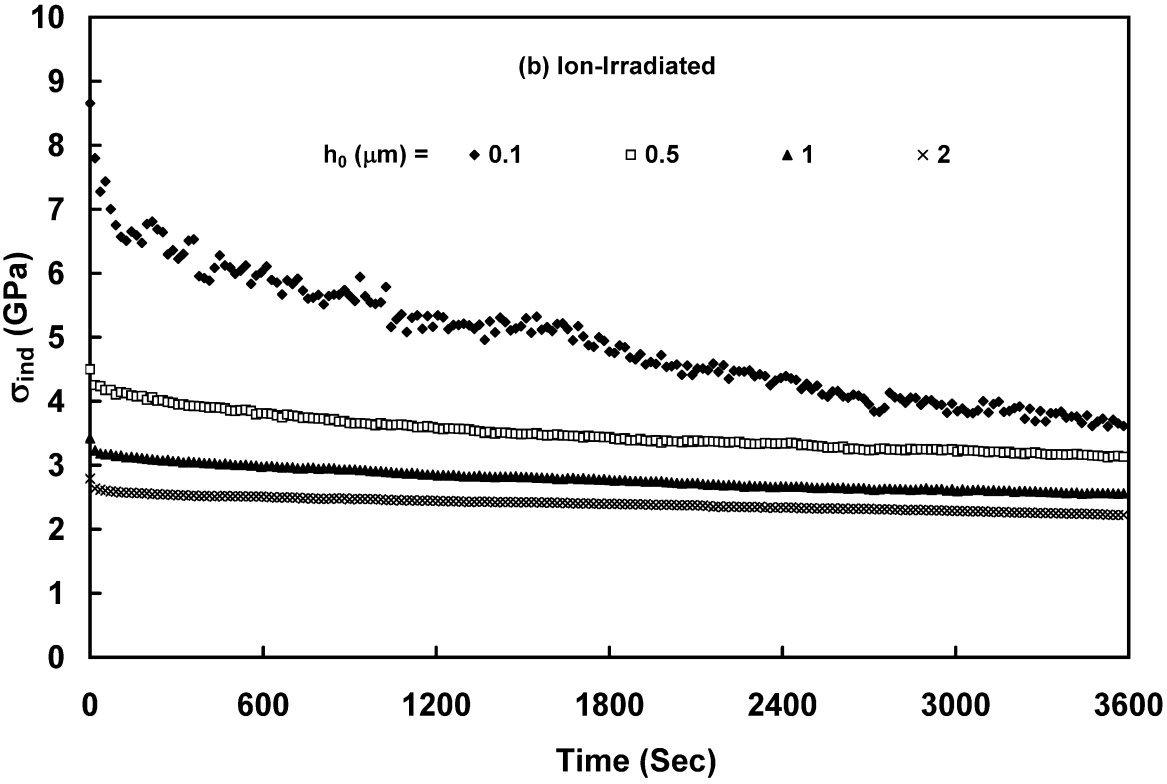

Figure 4.3: Typical average indentation stress σ_{ind} versus time plots from constant-load indentation creep tests performed on the AN plane at different values of h_0 on: (a) non-irradiated, and (b) a Zr^+ ion-irradiated Zr-2.5%Nb. The trends shown in these figures are similar to those shown by the data from indentation tests performed on the RN and TN planes however the magnitude of σ_{ind} is different.

Fig. 4.3 shows the typical decrease in σ_{ind} (Eq. 4.1) with time during constant-load indentation creep tests performed on the AN plane of non-irradiated and Zr^+ ion-irradiated Zr-2.5%Nb material. σ_{ind} decreases with increasing time because h increases, due to creep deformation, while F remains constant. These plots are similar in shape to those obtained from the tests performed on the RN and TN planes however the magnitude of σ_{ind} is different due to the mechanical anisotropy of the material.

4.3.1 Mechanical anisotropy of the non-irradiated Zr-2.5%Nb

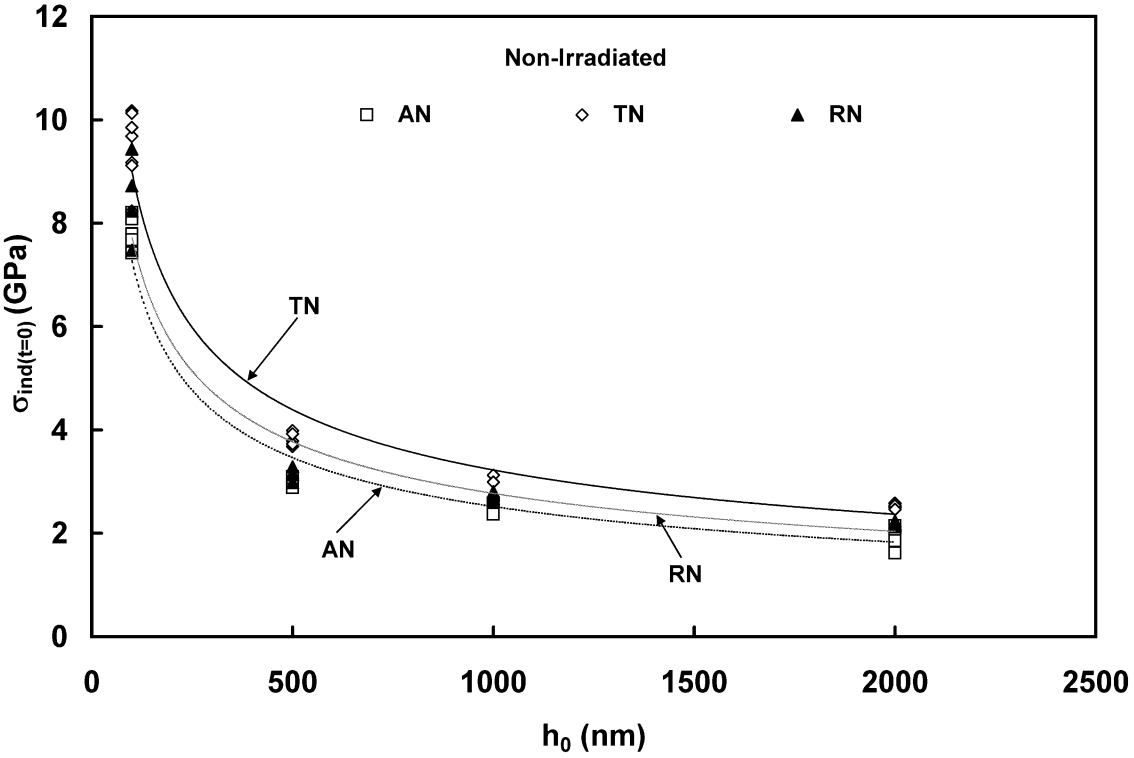

Figure 4.4: Variation in $\sigma_{ind(t=0)}$ with initial indentation depth, h_0 , for indentation tests performed on the AN, TN and RN planes of the non-irradiated Zr-2.5%Nb.

The anisotropy of the depth dependence of the initial indentation stress, at the instant that h_0 is reached, $\sigma_{ind_{t=0}}$ is shown in Fig. 4.4 for the non-irradiated Zr-2.5%Nb material. The decreasing $\sigma_{ind_{t=0}}$ with increasing h_0 is typical of the depth dependence of the indentation hardness reported for most metals [23, 28-34]. $\sigma_{ind_{t=0}}$ is larger, at all depths, for indentations made on the TN plane compared to those made on either the RN or AN planes. The ratio of $\sigma_{ind_{t=0}}$ on the TN plane relative to $\sigma_{ind_{t=0}}$ on the AN planes, calculated from the deepest indentations (h_0 = 2μm), is 1.3 (Table 4.1). This ratio is very close to the previously reported ratio of 1.4 for the uniaxial tensile yield stress in the transverse

direction relative to that in the axial direction of Zr-2.5%Nb pressure tube material [6]. The ratio of $\sigma_{ind_{t=0}}$ on the TN plane relative to $\sigma_{ind_{t=0}}$ on the RN planes is 1.2 (Table 4.1). No tensile test data are available from the radial direction due to the small thickness of these pressure tubes.

Table 4.1: The ratio of $\sigma_{ind_{t=0}}$ on the TN plane relative to $\sigma_{ind_{t=0}}$ on the AN and RN planes before and after irradiation

Stress Ratios	Before Irradiation	After Irradiation
$\frac{\sigma_{ind\,t=0}(TN)}{\sigma_{ind\,t=0}(AN)}$	1.3	1.04
$\frac{\sigma_{ind\,t=0}(TN)}{\sigma_{ind\,t=0}(RN)}$	1.2	1.08

Fig. 4.5 illustrates the orientation of the unit cell of the majority of the hcp α-phase grains with respect to the indentation direction for indentation made on the AN, RN, and TN planes in the Zr-2.5%Nb pressure tubes. For indentations made on the TN plane, most of the α-phase grains are oriented such that the <0001> c-axis is parallel to the direction of indentation whereas indentations made on AN and RN planes are aligned with the indentation direction parallel to $<10\bar{1}0>$ and $<11\bar{2}0>$ respectively. Previously reported uniaxial tests have indicated that plastic deformation of Zr based materials occurs primarily by prismatic slip along the $\{10\bar{1}0\}<\bar{1}2\bar{1}0>$ system however when loaded in the direction of the c axis deformation occurs by pyramidal slip primarily along the $\{10\bar{1}1\}<\bar{1}\,\bar{1}23>$ system [35-39]. Since indentation performed on the TN plane involves application of indentation force primarily in the <0001> c axis direction it is very likely that pyramidal slip plays a more prominent role in the deformation process than during indentation on either the RN or AN planes. This could account for the observed anisotropy of $\sigma_{ind_{t=0}}$ since the critical resolved shear stress for pyramidal slip is considerably greater than that for prismatic slip [36]. The data in Fig. 4.4 indicate that although a multiaxial stress state exists beneath a pyramidal indentation, the measured

indentation stress still displays the same overall anisotropy with respect to the loading direction as that obtained from uniaxial tensile tests.

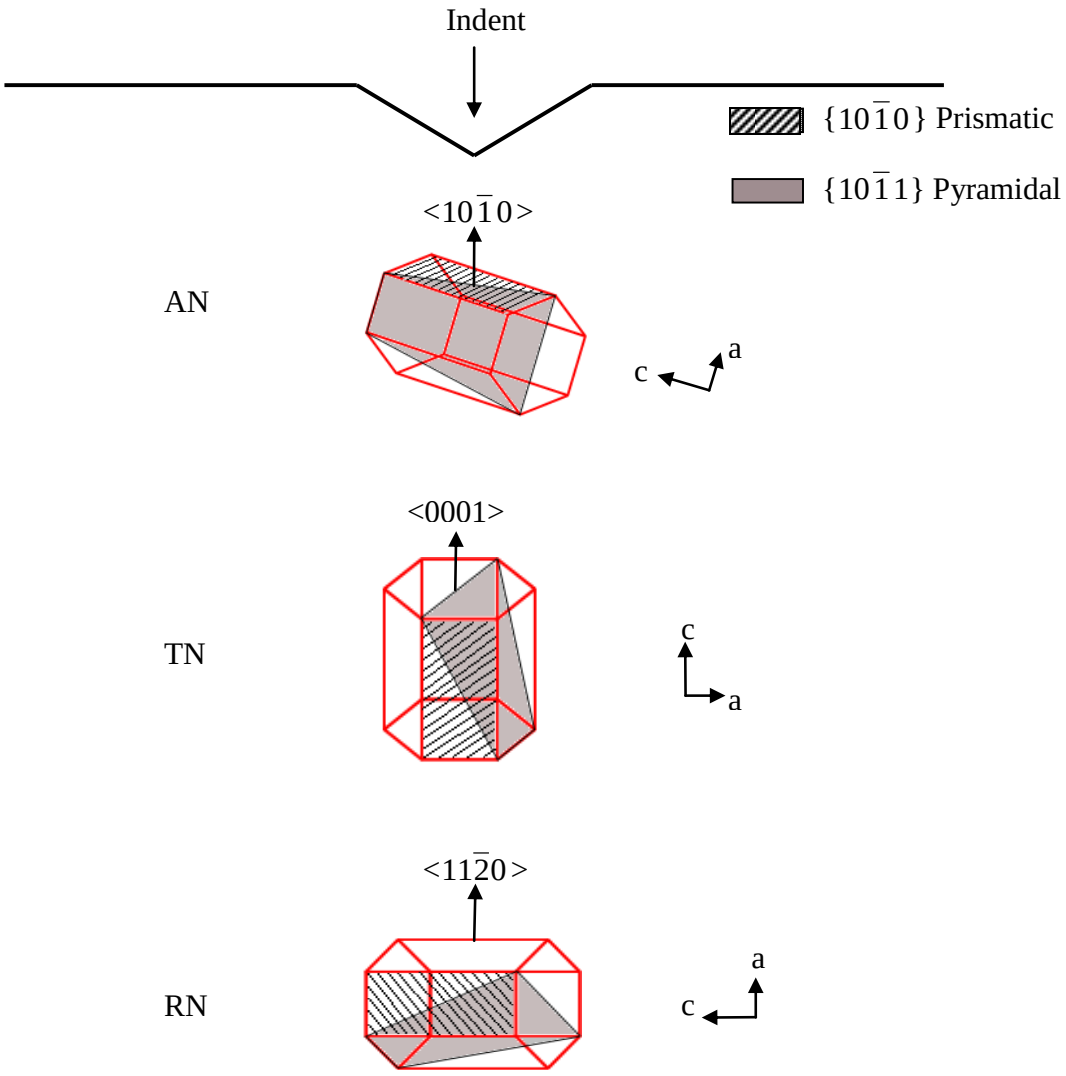

Figure 4.5: Schematic presentation of the orientation of the hcp unit cell of the majority of the α-phase grains in the Zr-2.5%Nb samples with respect to the indentation direction. The orientation of the prismatic and the pyramidal slip planes is shown.

Fig.4.6 shows a plot of the indentation stress relaxation rate $\partial\sigma_{ind}(t)/\partial t$ versus σ_{ind} for all the indentation creep tests performed on the non-irradiated samples. The data from tests performed at different indentation depths on the RN and AN planes lie on essentially the same curve indicating that similar indentation creep behaviour occurs, for these samples, over a wide range of indentation stress and depth. The shape of the $\partial\sigma_{ind}(t)/\partial t$ versus σ_{ind} curve for indentations performed on the TN plane is quite different from that of the RN and AN planes particularly at the high levels of indentation stress. This apparent creep anisotropy is discussed, along with an assessment of the effect of ion irradiation on the creep anisotropy, at the end of Section 4.3.2.

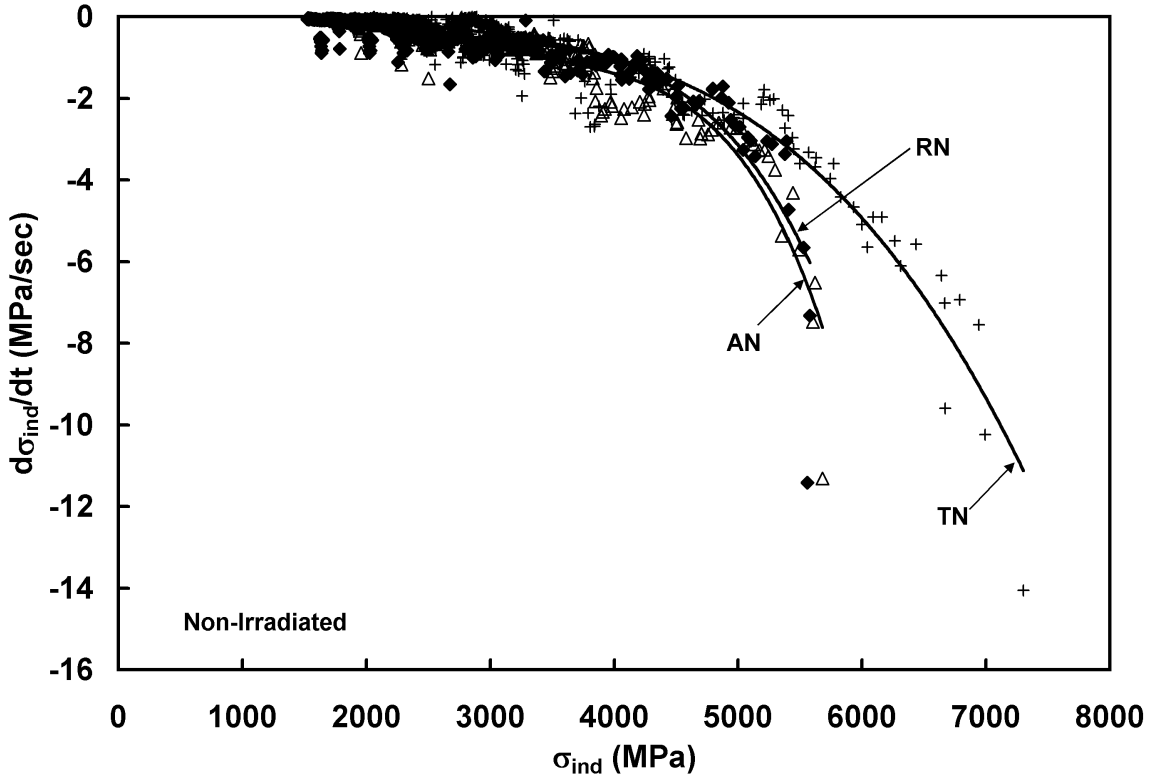

Figure 4.6: The rate of change of indentation stress, $\partial\sigma_{ind}(t)/\partial t$, versus σ_{ind} for non-irradiated AN, TN and RN samples. For all cases data from tests performed at different indentation depths lie on essentially the same curves. However the shape of the TN curve is different from the other two curves indicating an apparent anisotropy in the thermal indentation creep mechanism.

4.3.2 Mechanical anisotropy of Zr^+ ion-irradiated Zr-2.5%Nb

Fig. 4.7 depicts the indentation depth dependence of the initial indentation stress $\sigma_{ind_{t=0}}$ for samples indented on the AN, RN, and TN planes after Zr^+ ion irradiation. The indentation stress decreases with increasing indentation depth similar to that observed in the non-irradiated material. The ratio of $\sigma_{ind_{t=0}}$ on the TN plane relative to that on the AN planes is 1.04 (Table 4.1). The stress ratio calculated from uniaxial tensile test data reported by Himbeault et al. [14] shows that the ratio 1.4 in the non-irradiated condition [6] has decreased to 1.2 after 15 years of service i.e. the ratio has decreased about 14% whereas in our case the ratio has decreased about 20% after 30 dpa damage which is equivalent to 30 years of in-reactor operation. This indicates that the anisotropy of the yield stress has markedly decreased as a result of irradiation hardening. The ratio of $\sigma_{ind_{t=0}}$ on the TN plane relative to $\sigma_{ind_{t=0}}$ on the RN planes is 1.08 (Table 4.1) after irradiation.

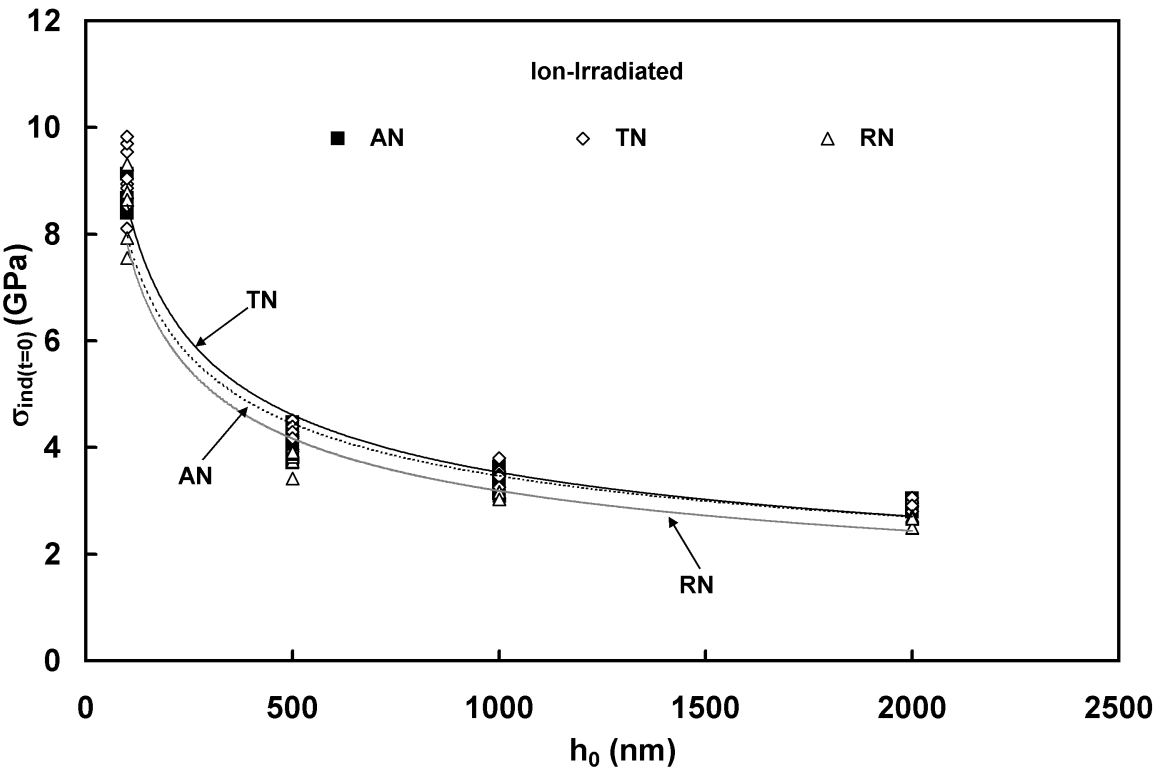

Figure 4.7: Variation in $\sigma_{ind(t=0)}$ with initial indentation depth, h_0 for indentation tests performed on the AN, TN and RN planes of the Zr^+ ion-irradiated Zr-2.5%Nb.

Comparison of Figs. 4.7 and 4.4 indicates that the Zr^+ irradiation has significantly increased the hardness of the material. We define the relative change in indentation stress $\Delta\hat{\sigma}$ as

$$\Delta\hat{\sigma} = \frac{\sigma_{ind_{irradiated}} - \sigma_{ind_{nonirradiated}}}{\sigma_{ind_{nonirradiated}}} \tag{4.3}$$

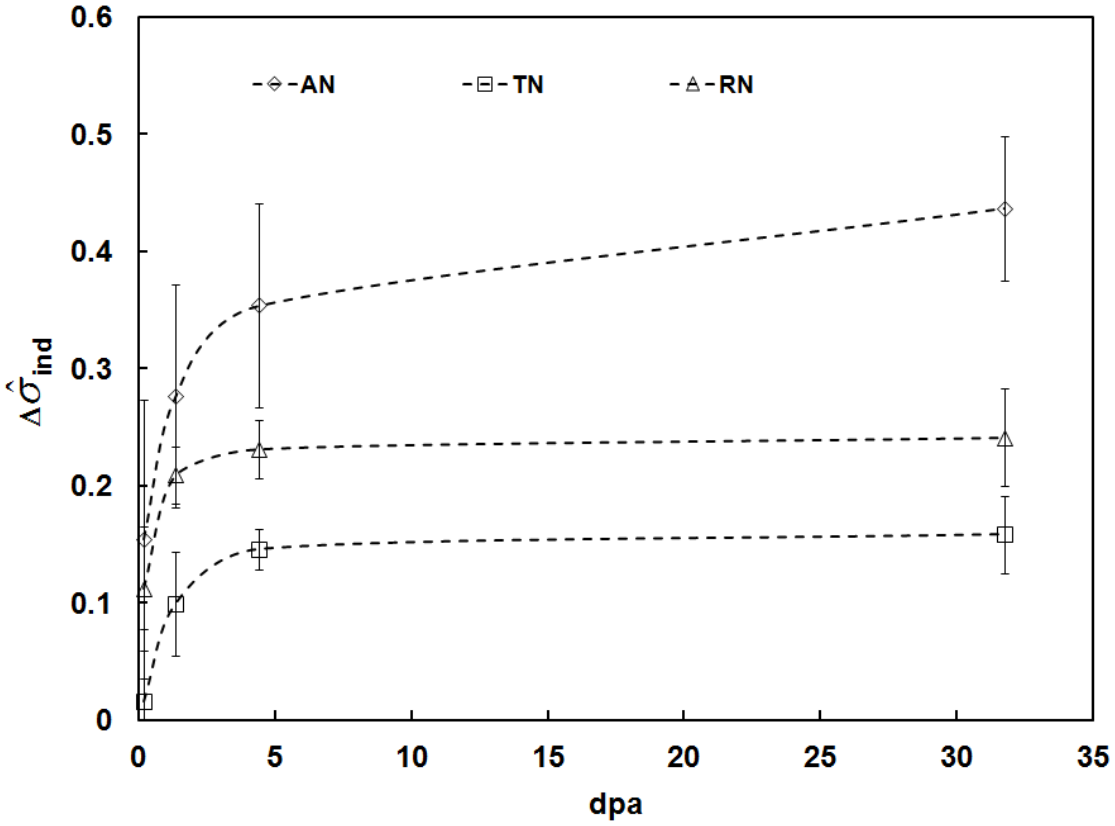

Figure 4.8: Normalized change in the initial indentation stress $\Delta\hat{\sigma}_{ind}$ (Eq. 4.3) plotted against the level of Zr^+ ion irradiation damage as expressed by displacements per atoms (dpa) for indentation tests performed on the AN, TN, and RN planes of the Zr-2.5%Nb test material.

Fig. 4.8 shows $\Delta\hat{\sigma}$, calculated from the $\sigma_{ind_{t=0}}$ data, plotted against the level of irradiation damage expressed in dpa, as calculated from Fig. 4.2, at the indentation depth of the

specific test performed on the ion-irradiated AN, RN, and TN samples. Considerable anisotropy exists in the degree of ion-irradiation hardening. Indentations made on the AN plane show the largest $\Delta\hat{\sigma}$ for a given level of dpa. This finding is in agreement with those of Nakatsuka et al [17,18] and Mahmoud et al [19] who report that, for Zircaloy samples, neutron-irradiation has a larger effect upon inhibiting prismatic dislocation glide than pyramidal dislocation glide.

Fig.4.9 shows $\Delta\hat{\sigma}_{ind}$ plotted against the resolved basal pole fraction aligned in the direction of indentation (Fig. 4.1) for indentations made at levels of Zr^{+} ion irradiation damage ranging from 0.2 to 30 dpa. The amount of irradiation hardening, i.e. the magnitude of $\Delta\hat{\sigma}_{ind}$, increases, for any level of irradiation damage, with decreasing basal pole fraction in the direction of indentation.

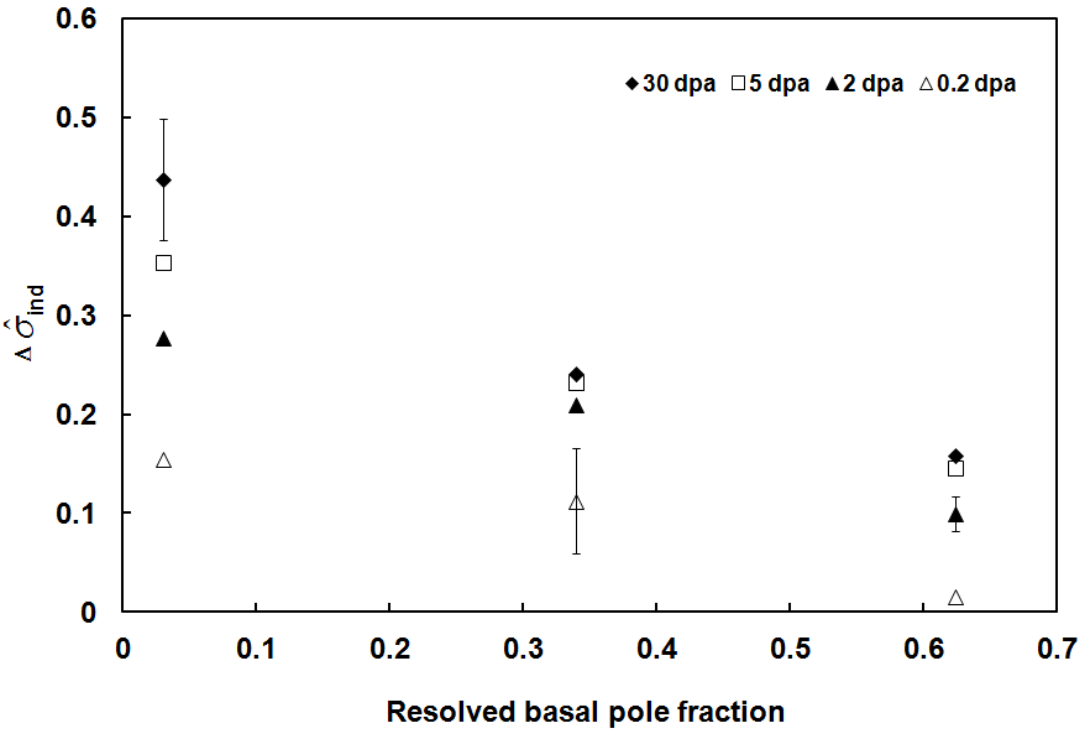

Figure 4.9: Normalized change in the initial indentation stress $\Delta\hat{\sigma}_{ind}$ (Eq. 4.3) plotted against the resolved basal pole fraction aligned in the direction of indentation for indentations made in Zr-2.5%Nb that had levels of Zr^{+} ion irradiation damage ranging from 0.2 to 30 dpa.

A plot of $\partial\sigma_{ind}(t)/\partial t$, versus σ_{ind} for the indentation creep tests performed on the ion-irradiated material is shown in Fig.4.10. Comparison of Figs. 4.10 and 4.6 indicates that while the non-irradiated material displays anisotropic creep behaviour, i.e. indentation creep on the TN plane follows a different trend than that on the AN and RN planes, the ion-irradiated material displays essentially isotropic creep behaviour.

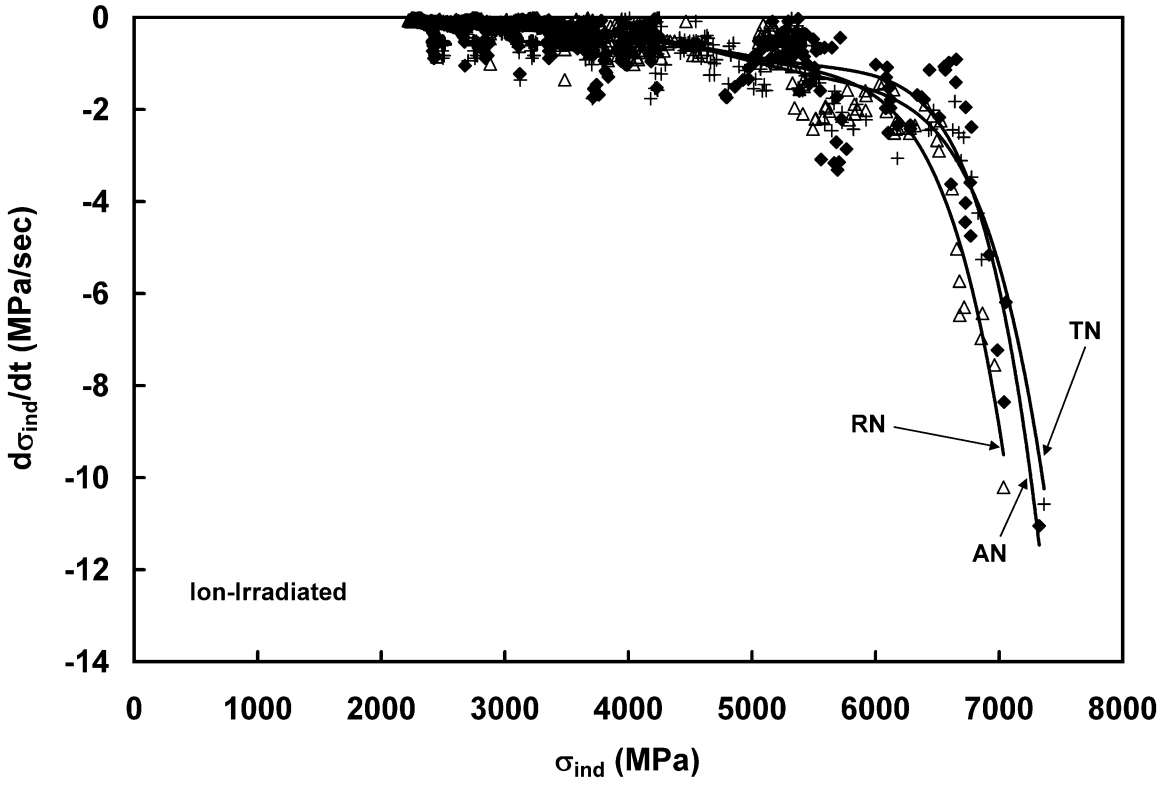

Figure 4.10: The rate of change of indentation stress, $\partial\sigma_{ind}(t)/\partial t$, versus σ_{ind} for Zr^{+} ion-irradiated AN, TN and RN samples. For all cases, the data from tests performed at different indentation depths lie on essentially the same curve. The shape of the curve is not significantly dependent upon indentation direction. This indicates the isotropy of the thermal indentation creep of the ion-irradiated material.

The mechanism of creep deformation that operates during the one-hour constant F stage of the indentation tests can be assessed by first converting σ_{ind} and $\dot{\varepsilon}_{ind}$ (Eqs. 4.1 and 4.2) to equivalent average shear stress τ_{ind} and shear strain rate $\dot{\gamma}_{ind}$ that are characteristic of the pyramidal indentation stress state [40]:

$$\tau_{ind} = \frac{\sigma_{ind}}{3\sqrt{3}} \qquad \tau_{eff} = \frac{\sigma_{ind} - \sigma_{th}}{3\sqrt{3}} \tag{4.4}$$

$$\dot{\gamma}_{ind} = \frac{\sqrt{3}\dot{h}}{h} \tag{4.5}$$

Since the local stress ahead of a pyramidal indentation is very high, and the test temperature of this study is very low relative to the melting temperature of zirconium alloys, the indentation creep occurs by a mechanism involving dislocation glide where the rate of dislocation glide is limited by the strength of discrete obstacles present within the microstructure. The shear strain rate $\dot{\gamma}$ for such a mechanism can be expressed in terms of the yield shear stress τ_{yield}, the effective shear stress τ_{eff} driving the creep process, and the absolute temperature T as [41]

$$\dot{\gamma} = \dot{\gamma}_p \left(\frac{\tau_{yield}}{\mu} \right)^2 e^{-\frac{\Delta G(\tau_{eff})}{kT}} \tag{4.6}$$

Where $\dot{\gamma}_p$ is constant (we use $\dot{\gamma}_p = 10^{11} s^{-1}$ in keeping with that suggested by Frost and Ashby [41]), μ is the elastic shear modulus, k is Boltzmann's constant and $\Delta G(\tau_{eff})$ is the thermal energy required for a dislocation, subjected to τ_{eff}, to overcome the discrete obstacles. $\Delta G(\tau_{eff})$ can be expressed by the following general equation [40, 41]

$$\Delta G\left(\tau_{eff}\right) = \Delta G_0 \left[1 - \left(\frac{\tau_{eff}}{\hat{\tau}}\right)^p\right]^q \tag{4.7}$$

where ΔG_0 is the activation energy required for a dislocation to move past the discrete obstacles, $\hat{\tau}$ is the athermal shear strength of the material, *p* and *q* are constants. ΔG_0 and the constants *p* and *q* are characteristic of the particular dislocation-obstacle interaction that governs the creep rate and, in the case of the Zr-2.5%Nb material in this study, may depend upon indentation direction. Our previous studies of the indentation creep rate on the RN plane of Zr-2.5%Nb have found that ΔG_0 is independent of indentation depth but increases with prior Zr^+ ion irradiation [23].

In this study we have determined $\Delta G\left(\tau_{eff}\right)$ by fitting Eq. 4.6 to the $\dot{\gamma}_{ind}$ versus τ_{eff} data obtained from each one hour constant F creep test performed on the non-irradiated and the Zr^+ ion-irradiated samples. To accomplish this we assume that the rate of stress relaxation after one-hour of indentation creep is sufficiently low that $\sigma_{ind_{t=1hr}}$ corresponds to the threshold stress σ_{th} (Eq. 4.4) below which no significant further creep occurs. The activation energy ΔG_0 was then determined by extrapolating the $\Delta G\left(\tau_{eff}\right)$ versus τ_{eff} trends, obtained from each indentation creep test, to $\tau_{eff} = 0$.

The dependence of ΔG_0, normalized with respect to μb^3 where *b* is the Burgers vector, upon irradiation damage for indentation creep tests perform on the AN, RN and TN planes is shown in Fig. 4.11. While ΔG_0 increases with increasing irradiation damage its magnitude is essentially independent of indentation direction. The increase in ΔG_0 with increasing Zr^+ irradiation indicates the effectiveness of the irradiation-induced damage as obstacles to dislocation glide. ΔG_0 is between 0.182 and 0.215 μb^3. This is of magnitude similar to what is expected for the free energy of "intermediate strength" obstacles to dislocation glide such as dislocation/dislocation interactions [41].

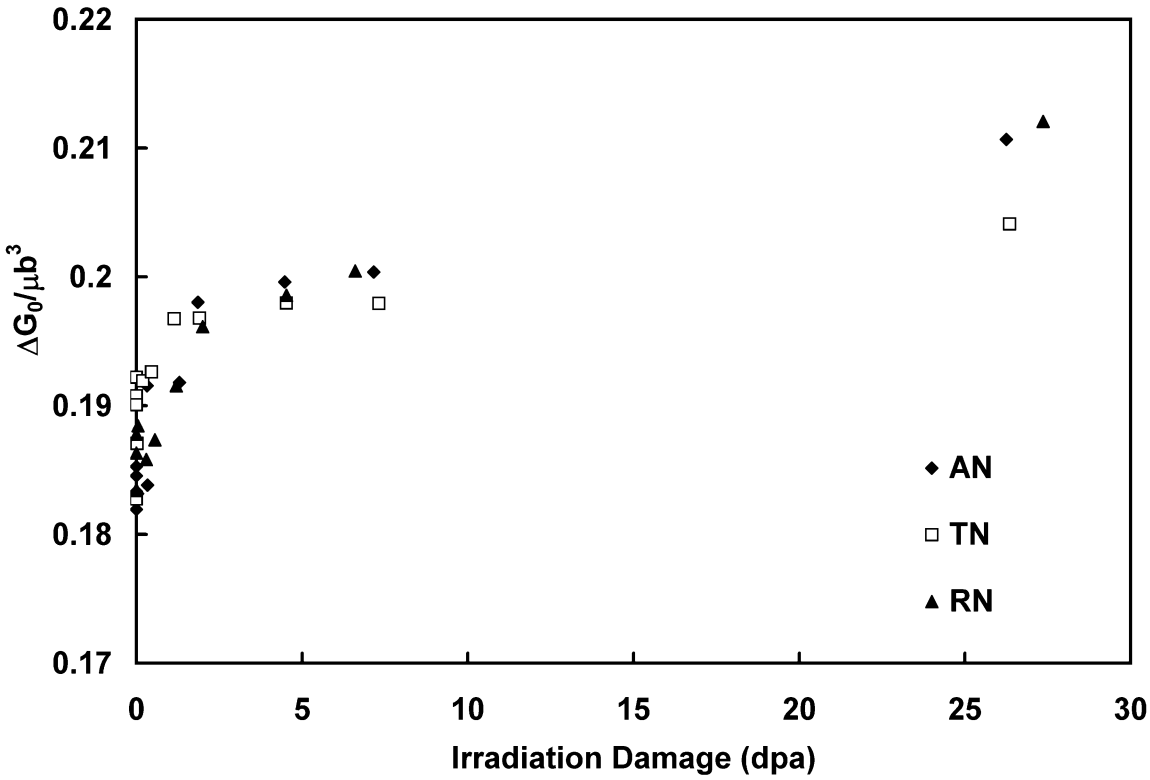

Figure 4.11: Activation energy ΔG_0 ,normalized with respect to the strain energy (μb^3) of a dislocation, plotted against the level of Zr^+ ion irradiation damage as expressed by displacements per atoms (dpa) for indentation tests performed on the AN, TN, and RN planes of the Zr-2.5%Nb test material.

4.4 Conclusions

Constant load pyramidal indentation creep tests were performed to study the effect of Zr^+ ion irradiation on the anisotropy of the local plastic deformation of the Zr-2.5%Nb pressure tube material. All tests were performed at 25^{o}C on the RN [23], AN, and TN planes of non-irradiated and Zr^+ ion irradiated material.

The average indentation stress $\sigma_{ind\,t=0}$ increased with decreasing indentation depth, in keeping with the commonly observed depth dependence of indentation hardness, and is larger, at all depths, for indentations made on the TN plane compared to those made on

either the RN or AN planes. The ratio of $\sigma_{ind_{t=0}}$ on the TN plane relative to $\sigma_{ind_{t=0}}$ on the AN and RN planes is 1.3 and 1.2 respectively. The stress ratio between TN and AN plane agrees well with the previously published uniaxial test results.

The indentation stress increases with increasing levels of Zr^+ ion irradiation. The amount of increase is highest for indentations made in the axial direction and lowest for indentations made in the transverse direction of the pressure tube. The ratio of $\sigma_{ind_{t=0}}$ on the TN plane relative to $\sigma_{ind_{t=0}}$ on the AN and RN planes is now 1.04 and 1.08 respectively indicating that the anisotropy of the yield stress is decreased as a result of irradiation hardening. The relative change in indentation stress $\Delta\hat{\sigma}$, for any level of irradiation damage, decreases with increasing resolved fraction of basal poles in the indentation direction. This suggests, since the Zr-2.5%Nb pressure tubing studied here is strongly textured with basal pole alignment in the transverse (circumferential) direction, that the ion irradiation damage has a greater effect on blocking the movement of dislocations on prismatic compared to pyramidal slip systems. This is in agreement with previously reported findings from impression tests performed on Zircaloy alloys [17-19].

The activation energy ΔG_0 of the obstacles that limit the rate of dislocation glide during indentation creep of the Zr-2.5%Nb at 25^{o}C does not change with indentation direction. ΔG_0 does, however, increase with increasing levels of Zr^+ ion damage. The increase is due to the increased crystallographic damage, which acts as obstacles to the dislocation glide.

4.5 Acknowledgements

The authors wish to thank the Natural Science and Engineering Research Council of Canada (NSERC) and the University Network of Excellence in Nuclear Engineering (UNENE) who provided financial support for this research. The assistance of Dr. T. Simpson of the University of Western Ontario Nanofabrication Laboratory in preparing the TEM foils is gratefully acknowledged. Finally, we offer a special note of thanks to

Mr. B. Leitch of the Atomic Energy of Canada Ltd (Chalk River Laboratories) for providing the Zr-2.5%Nb pressure tube material used in this study.

4.6 References

[1] P.A. Ross-Ross, V. Fidleris, D.E. Fraser, Canadian Metallurgical Quarterly, v. 11 (1972), p. 101

[2] P.A. Ross-Ross, W. Evans, W.J. Langford, Atomic Energy of Canada Ltd Research Report, AECL-4262 (1972), p. 1

[3]N. Christodoulou, P.A. Turner., C.N. Tomé., C.K. Chow, R.J. Klassen, Metall. and Mat. Trans. A., v. 33 (2002), p. 1103

[4] A.R. Causey, V. Fidleris, S.R. MacEwen, C.W. Schulte, Influence of Radiation on Material Properties: 13th Intl. Symp. (1987), p. 54

[5] A.R. Causey, A.G. Norsworthy, C.W. Schultes, Can. Metall. Quart., v. 24 (1984), p. 207

[6] N. Christodoulou, P.A. Turner., E.T.C. Ho, C.K. Chow, M.R. Levi, Metall. and Mat. Trans. A., v. 31A (2000), p. 409

[7] N. Christodoulou, A.R. Causey, r.a. Holt, C.N. Tomé, N. Badie, R.J. Klassen, R. Sauvé, C.H. Woo, Zirconium in the nuclear industry: Eleventh Int. Symp.(1996), p. 518

[8] B.S. Rodchenkov, A.N. Semenov, Nucl. Eng. And Design, v. 235 (2005), p. 2009

[9] E.F. Ibrahim, J. of Nucl. Mat., v. 101 (1981), p. 1

[10] E.F. Ibrahim, R.A. Holt, J. of Nucl. Mat., v. 91 (1980), p. 311

[11] R.A. Holt, N. Christodoulou, A.R. Causey, J. of Nucl. Mat., v. 317 (2003), p. 256

[12] M. Griffiths, N. Wang, A. Buyers, S.A. Donohue, J. of ASTM Int., v. 5 (2008), p. 541

[13] M. Griffiths, P.H. Davis, W.G. Davis, S. Sagat, Zirconium in the nuclear industry: Thirteenth Int. Symp., ASTM, STP 1423 (2002), p. 507

[14] D.D. Himbeault, C.K. Chow, M.P. Plus, Metall. And Mater. Trans. A, v. 25 (1994), p. 135

[15] R.A. Holt, G.A. Bickel, N. Christodoulou, J. of Nucl. Mat., v. 373 (2008), p. 130

[16] R.A. Holt, J. of Nucl. Mat., v. 372 (2008), p. 182

[17] M. Nakatsuka, M. Nagai, J. of Nucl. Sci. And Tech., v. 24 (1987), p. 832

[18] M. Nakatsuka, M. Nagai, J. of Nucl. Sci. And Tech., v. 24 (1987), p. 906

[19] S.T. Mahmood, S.A. Hussien, P.S. Godavarti, K.L. Murty, Effects of Radiation on Materials: 15th Int. Symp., ASTM, STP 1125 (1992), p. 337

[20] P.S. Godavarti, S. Hussien, K.L. Murty, Metall. Trans. A, v. 19 (1988), p. 1243

[21] K.L. Murty, S. Hussien, Y.H. Jung, Scripta Metallurgica, v. 19 (1985), p. 1985

[22] M.D. Mathew, K.L. Murti, Proceedings of the 10th Intl. Conf. on Nucl. Engg, ICONE 10 (2002), p. 227

[23] B. Bose, R.J. Klassen, J. of Nucl. Mat., v. 399 (2010), p. 32

[24] V. Perovic, G.C. Weatherly, R.G. Fleck, Can. Metall. Quart., v. 24 (1985), p. 253

[25] M. Griffiths, C.K. Chow, C.E. Coleman, R.A Holt, S. Sagat, V.F. Urbanic, Atomic Energy of Canada Ltd Research Report, AECL-10844 (1993), p. 1

[26] A.C. Fischer-Cripps, Nanoindentation (2nd edition), Springer (2004) New York, p. 7

[27] K.L. Johnson, J. Mech. Phys. Solids., v. 18 (1970), p. 115

[28] V. Bhakhri and R. J. Klassen, J. Mater. Sci., v. 41 (2006), p. 2259

[29] V. Bhakhri and R. J. Klassen, J. Mater. Sci., v. 41 (2006), p. 2249

[30] V. Bhakhri and R. J. Klassen, Scripta Mater., v. 55 (2006), p. 395

[31] B. Bose and R. J. Klassen, Mat. Sci. and Eng. A., v. 500 (2009), p.164

[32] R. J. Klassen, B. J. Diak and S. Saimoto, Mater. Sci. Eng. A , v. 387-389 (2004), p. 297

[33] B. J. Diak and S. Saimoto, Mater. Sci. Eng. A, v. 319-321 (2001), p. 909.

[34] S. Saimoto, B. J. Diak and K. R. Upadhyaya, Mater. Sci. and Eng. A, v. 234-236 (1997), p. 1015.

[35] R.A. Holt, M. Griffiths, R.W. Gilbert, J. of Nucl. Mat., v. 149 (1987), p. 51

[36] A. Akhtar, J. of Nucl. Mat., v. 47 (1973), p. 79

[37] E. Tenckhoff, J of ASTM Int., v. 2 (2005), p. 119

[38] A. Salinas-Rodriguez., M.G. Akben, J.J. Jonas, E.F. Ibrahim, Canadian Metallurgical Quarterly, v. 24 (1985), p. 259

[39] M. Griffiths, J. of Nucl. Mat., v. 205 (1993), p. 225

[40] U.F. Kocks, A.S. Argon, M.F. Ashby, Prog. Mat. Sci., v. 19 (1975), p. 1

[41] H. J. Frost and M. F. Ashby, Deformation-Mechanism Maps, Pergamon Press, Oxford (1982)

Chapter 5

5 Assessment of the Effect of Irradiation Temperature on the Mechanical Anisotropy of the Zr^+ Ion Irradiated Zr-2.5%Nb*

In the previous chapters, creep tests were performed on pressure tube material that was irradiated at 25°C. This chapter describes the investigations carried out on Zr-2.5%Nb pressure tube material irradiated with Zr^+ at 300°C, and compares the results with those reported in the earlier chapters.

5.1 Introduction

Extruded and cold drawn Zr-2.5%Nb pressure tubes used in CANDU nuclear reactors are mechanically anisotropic due to their heavily textured hcp grain morphology. Mechanical characterization of these pressure tubes has traditionally been done with conventional uniaxial test techniques [1-12] and thus, because of geometrical constraints, the mechanical properties in the radial (thickness) direction of the tubes have not been well studied. In previous studies we have overcome this problem by using micro-indentation tests performed on the RN, AN, and TN planes of the Zr-2.5%Nb pressure tubes to characterize the anisotropy of the indentation stress, which is related to the flow stress, and the indentation creep [13, 14].

---

* A version of this chapter was published as: Assessment of the Effect of Irradiation Temperature on the Mechanical Anisotropy of the Zr^+ Ion Irradiated Zr-2.5%Nb, by Bipasha Bose and Robert J. Klassen, MRS Proceedings, Volume 1298 (2011), pp. q07-02 (6 pages), Copyright © 2011 Materials Research Society. Reprinted with the permission of Cambridge University Press.

In previous studies we have also shown that high energy Zr^+ ion irradiation is an effective way to simulate the crystallographic damage resulting from neutron irradiation in Zr-2.5%Nb pressure tube material. Micro-indentation hardness testing at depths in the range of several micrometers, which corresponds to the depth of maximum ion irradiation damage, allows one to study the effect of irradiation damage on the mechanical anisotropy of Zr-2.5%Nb pressure tube material. Micro-indentation hardness and creep tests performed at 25°C on pressure tube material that was ion irradiated at 25°C demonstrate that irradiation damage reduces the mechanical anisotropy of the material and increases the apparent activation energy of the indentation creep process [13, 14].

Since the service temperature of CANDU pressure tubes is between 250°C and 310°C it is necessary to assess the extent that concurrent thermal annealing during irradiation will affect the mechanical anisotropy of both the indentation stress and the indentation creep of irradiation hardened pressure tube material. In this study we assess the effect of concurrent thermal annealing on the extent and nature of irradiation hardening by performing micro-indentation tests on Zr-2.5%Nb pressure tube material that was irradiated with Zr^+ ions at 300°C and compare the results with previously reported data from similar tests performed on non-irradiated Zr-2.5%Nb samples and samples that were irradiated at 25°C [13, 14].

5.2 Experiment

Rectangular samples, 8.5 mm by 8.5 mm and 4.0 mm thick, were cut from as-fabricated extruded and cold drawn Zr-2.5%Nb CANDU pressure tube material supplied by the Atomic Energy of Canada Ltd. This material has a strong crystallographic texture with the majority of the hcp α–phase grains aligned with their (0001) basal plane normal in the transverse direction of the tube. The calculated fraction of basal plane normals aligned in the axial, radial, and transverse directions of the pressure tube are $F_A = 0.031$, $F_R = 0.340$, and $F_T = 0.624$ respectively. The axial-normal (AN), radial-normal (RN), and transverse-normal (TN) surfaces of the samples were mechanically ground and chemically polished to an average roughness of about ± 8 nm and then irradiated at

300°C with 8.5 MeV Zr^+ ions. The ion irradiation was performed in vacuum in the Tandetron 1.7 MV tandem ion accelerator at the University of Western Ontario.

Monte Carlo simulation, via the SRIM software, was used to calculate the extent of crystallographic damage, in units of displacements per atom (dpa), imparted by the Zr^+ ions as a function of depth in the Zr-2.5%Nb substrate. The maximum irradiation damage occurred at about 2.0 μm below the surface of the sample. At this depth the applied Zr^+ dosage causes approximately 30 dpa. This is similar to the level of crystallographic damage incurred in a Zr-2.5% Nb pressure tube as a result of neutron exposure at about 300°C over thirty years in a CANDU nuclear reactor.

Micro-indentation tests were performed at initial indentation depths of h_0 = 0.1, 0.5, 1.0 and 2.0 μm to study the dependence of the indentation stress and indentation creep properties upon the level of irradiation damage. The micro-indentation tests were performed at 25°C using a pyramidal Berkovich diamond indenter on an instrumented nano-/micro-indentation tester (Micro Materials ltd, Wrexham, UK). During each test the indentation force (F) was slowly increased until the desired h_0 was reached. F was then held constant for one hour while the indentation depth h was continuously recorded.

5.3 Results & Discussion

Figure 5.1 depicts the dependence of the initial indentation stress $\sigma_{ind_{t=0}}$, obtained when h_0 is first reached during the loading stage of the indentation test, as a function of indentation depth h_0. $\sigma_{ind_{t=0}}$ was calculated as:

$$\sigma_{ind_{t=0}} = \frac{F}{24.5Ch_0^2} \tag{5.1}$$

where, $24.5h^2$ is the projected area of an ideal Berkovich indentation and C is a constant that accounts for the effect of sink-in and pile-up on the projected indentation area. C

was obtained from SEM measurement of the projected area of indentations of various depths. The indentation stress of metals decreases with increasing indentation depth up to about 10 μm and then remains relatively constant with further increasing depth. It is thought that this depth dependence of the indentation stress, widely known as indentation size effect [15-21], is due to the necessity of a higher local dislocation density to accommodate the larger plastic strain gradients associated with sub-micrometer deep indentations. As a result, $\sigma_{ind_{t=0}}$ decreases with increasing indentation depth in a manner that is typical of most ductile materials [22-27]. Figure 5.1(a) indicates that Zr^{+} ion irradiation increases $\sigma_{ind_{t=0}}$ relative to that of the non-irradiated material however the extent of the increase is reduced when the irradiation temperature is 300^{o}C compared to when it is 25^{o}C.

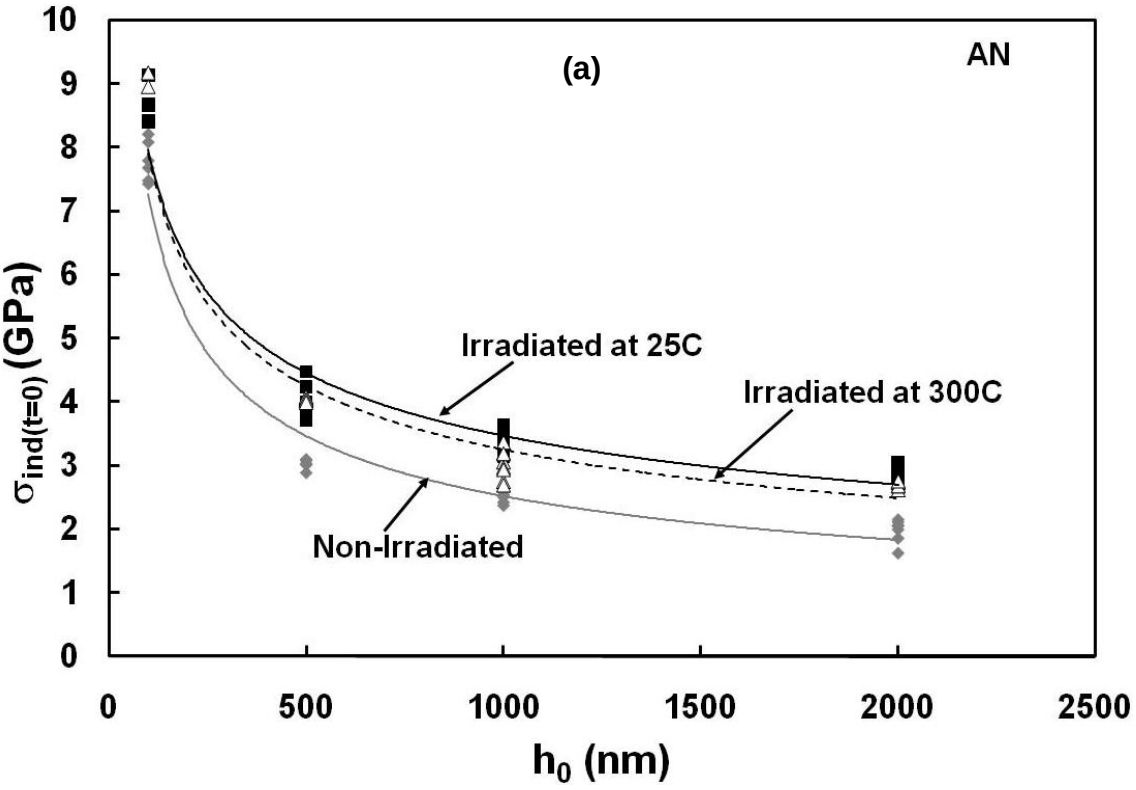

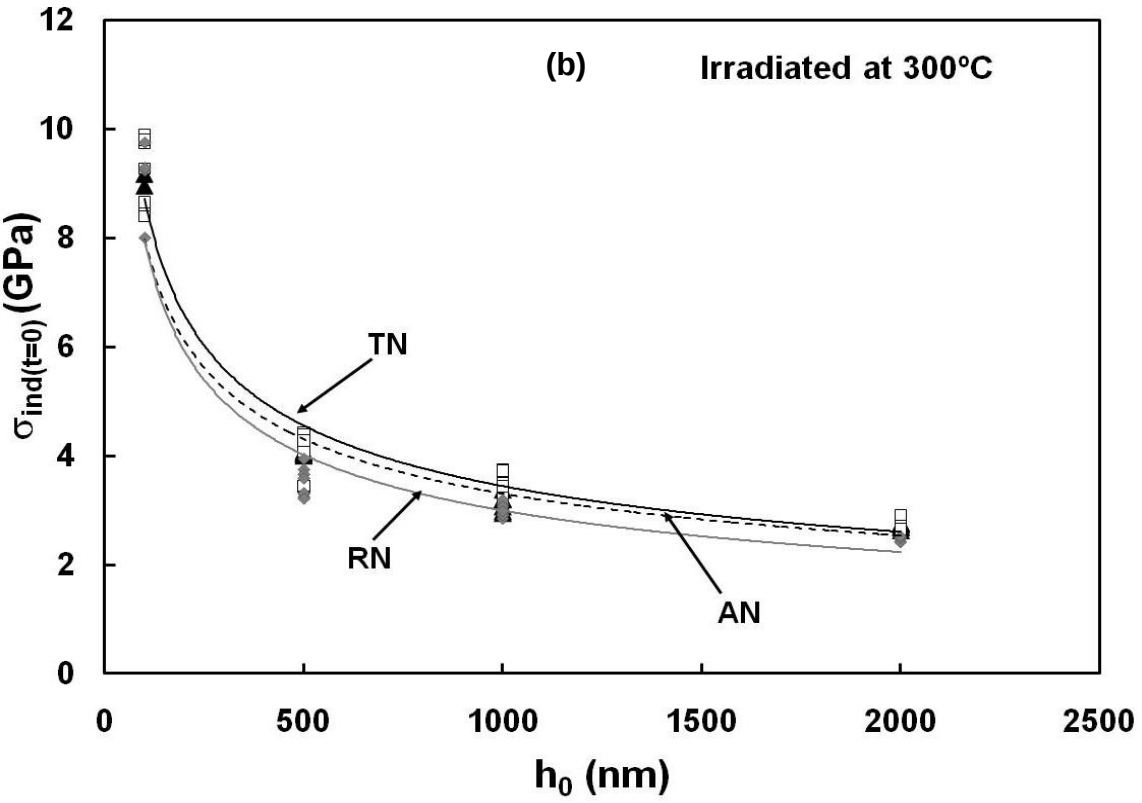

Figure 5.1: Dependence of the average initial indentation stress $\sigma_{ind(t=0)}$ upon initial indentation depth, h_0 , for tests performed on (a) the AN plane on samples that were either non-irradiated [13] or Zr^+ irradiated at 25°C [13] or 300°C and (b) on the AN, TN and RN planes of the Zr^+ ion-irradiated Zr-2.5%Nb at 300°C.

The effect of Zr^+ ion irradiation on the anisotropy of $\sigma_{ind_{t=0}}$ is shown in Figure 5.1(b) and summarized in Table 5.1. In the non-irradiated condition, the ratio of $\sigma_{ind_{t=0}}$ on the TN plane relative to that on the AN plane is 1.3 which is very close to the previously reported ratio of 1.4 for the uniaxial tensile yield stress [13]. The ratio of $\sigma_{ind_{t=0}}$ on the TN plane relative to that on the RN plane is 1.2. These ratios are reduced with Zr^+ ion irradiation at both 25°C and 300°C, however, the amount of reduction decreases with increasing irradiation temperature. To further study the effect of ion irradiation on $\sigma_{ind_{t=0}}$, we define the relative change in indentation stress $\Delta\hat{\sigma}$ that results from Zr^+ ion irradiation as

$$\Delta\hat{\sigma}_{ind} = \frac{\sigma_{ind_{irradiated}} - \sigma_{ind_{nonirradiated}}}{\sigma_{ind_{nonirradiated}}} \tag{5.2}$$

Table 5.1: The ratio of $\sigma_{ind_{t=0}}$ on the TN plane relative to that on the AN and RN planes before and after irradiation

Stress Ratios	Non-irradiated [13]	Zr^+ Irradiated at 25°C [13]	Zr^+ Irradiated at 300°C
$\frac{\sigma_{ind\,t=0}(TN)}{\sigma_{ind\,t=0}(AN)}$	1.3	1.04	1.10
$\frac{\sigma_{ind\,t=0}(TN)}{\sigma_{ind\,t=0}(RN)}$	1.2	1.08	1.14

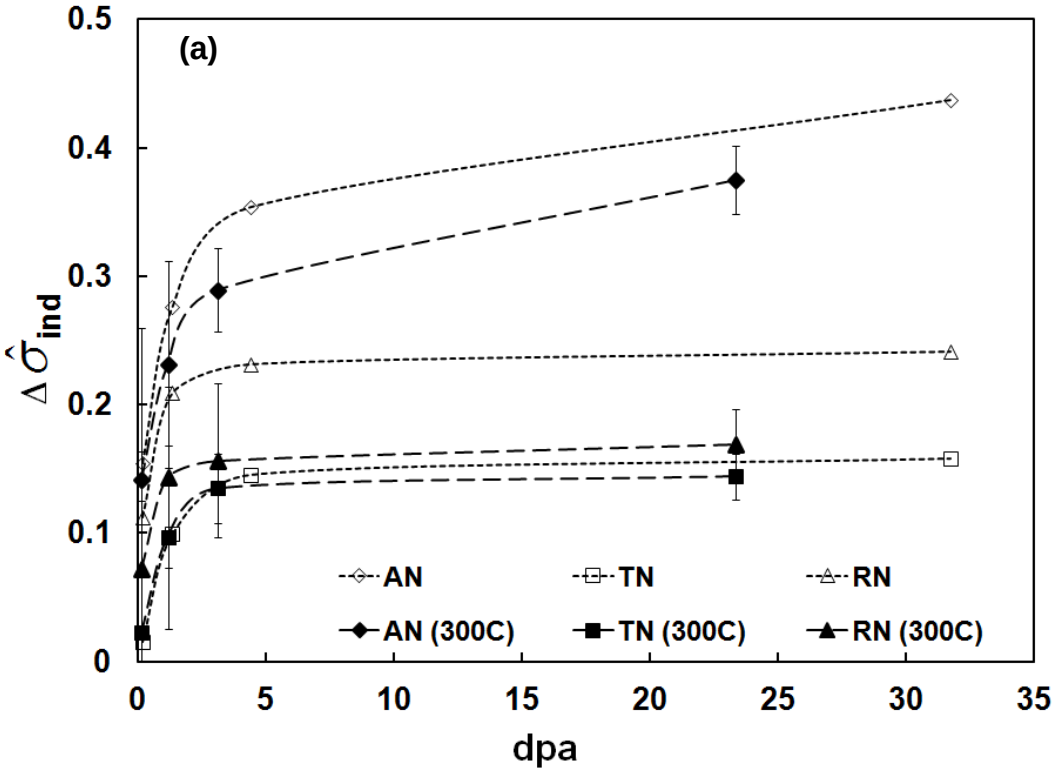

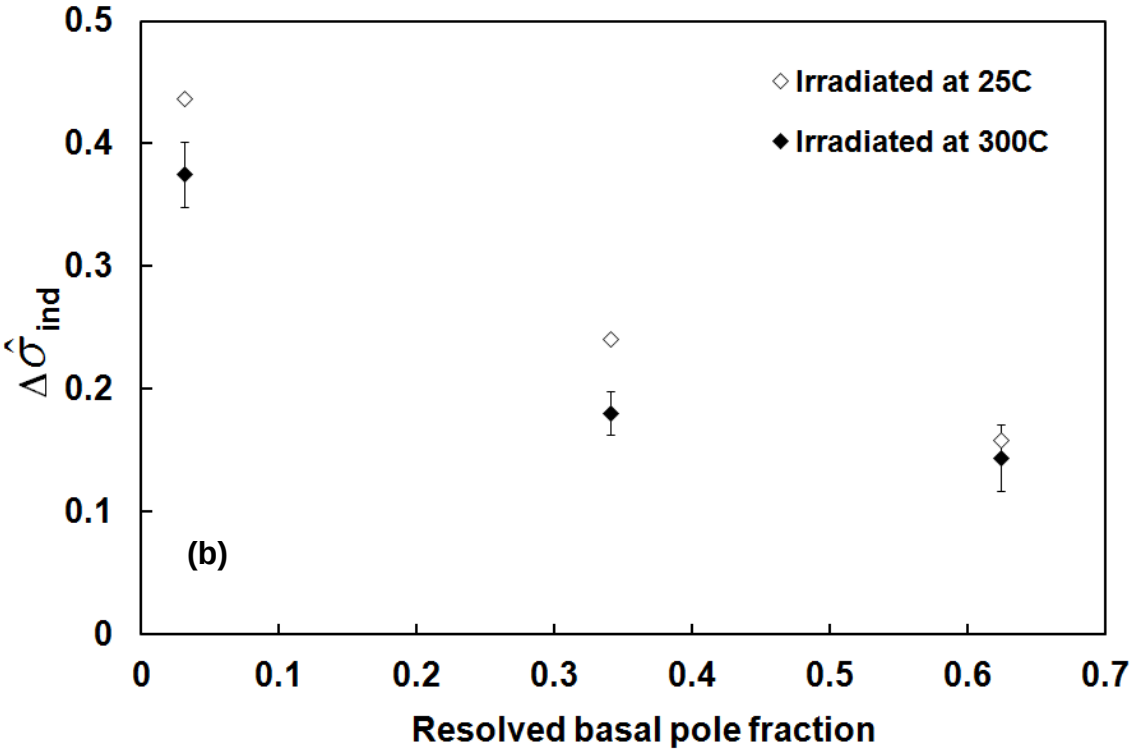

Figure 5.2: Normalized change in the initial indentation stress $\Delta\hat{\sigma}_{ind}$ plotted against (a) the level of Zr^+ ion irradiation damage (dpa) resulting from Zr^+ irradiation at 25°C [13] and 300°C (b) resolved basal pole fraction aligned in the direction of indentation for indentations made in Zr-2.5%Nb that were Zr^+ ion irradiated at 25°C [13] and 300°C.

Figure 5.2(a) shows $\Delta\hat{\sigma}_{ind}$, calculated from the $\sigma_{ind_{t=0}}$ data, plotted against ion irradiation damage. Indentations made on the AN plane show the largest $\Delta\hat{\sigma}_{ind}$ for a given level of dpa regardless of whether the Zr^+ ion irradiation is performed at 300°C or 25°C. Figure 5.2(b) shows $\Delta\hat{\sigma}_{ind}$, calculated from highest dpa levels, plotted against the resolved basal pole fraction aligned in the direction of indentation. The amount of irradiation hardening, i.e. the magnitude of $\Delta\hat{\sigma}_{ind}$, increases, for any level of irradiation damage, with decreasing basal pole fraction in the direction of indentation at both temperatures however the $\Delta\hat{\sigma}_{ind}$ values are lower for the 300°C irradiations.

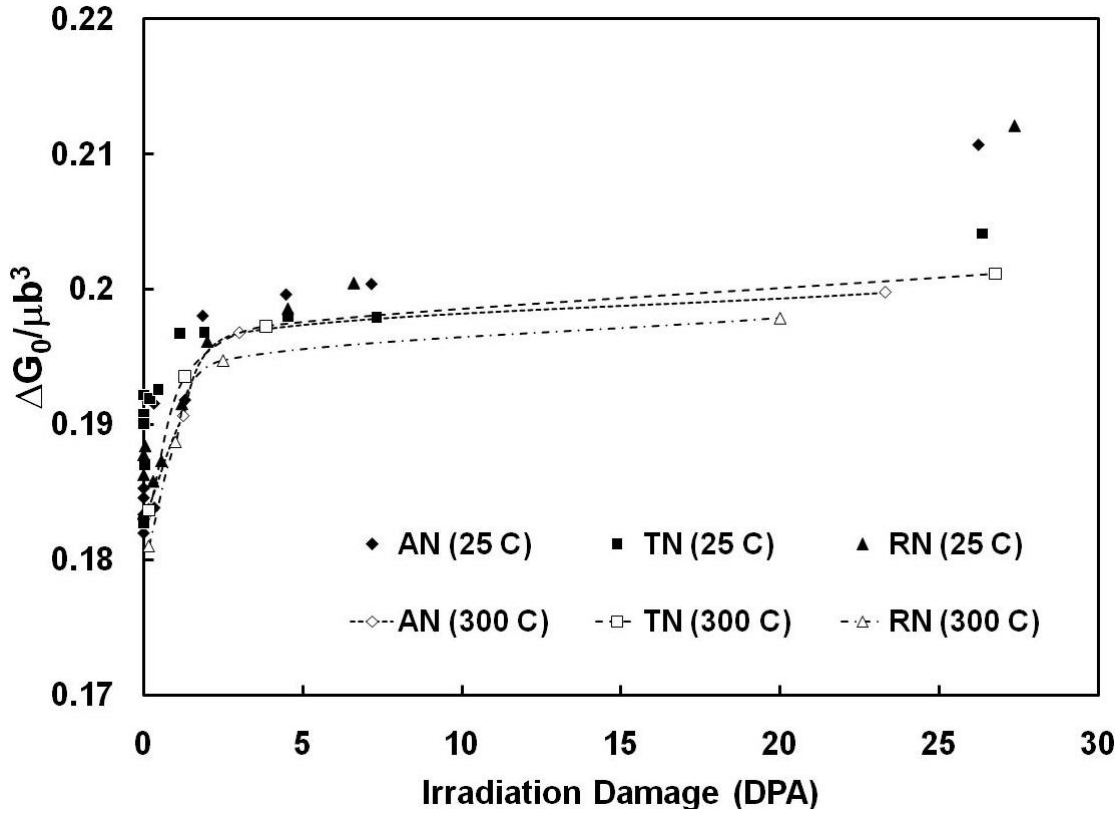

Figure 5.3: Apparent activation energy ΔG_0, normalized with respect to μb^3, plotted against the level of Zr^+ ion irradiation damage for samples irradiated at 25°C [13] and 300°C.

Since the local stress ahead of a pyramidal indentation is very high, the indentation creep occurs by a mechanism involving dislocation glide and the rate of dislocation glide is limited by the strength of discrete obstacles present within the microstructure. The shear strain rate $\dot{\gamma}$ resulting from the operation of such a time-dependent obstacle-limited dislocation glide process can be expressed in terms of the applied effective shear stress τ_{eff}, the yield stress in shear τ_{yield}, and the absolute temperature T as [29]

$$\dot{\gamma} = \dot{\gamma}_p \left(\frac{\tau_{yield}}{\mu} \right)^2 e^{-\frac{\Delta G(\tau_{eff})}{kT}} \tag{5.3}$$

where $\dot{\gamma}_p$ is constant (we use $\dot{\gamma}_p = 10^{11} s^{-1}$ in keeping with that suggested in Ref. [29]), μ is the elastic shear modulus, k is Boltzmann's constant and $\Delta G(\tau_{eff})$ is the thermal energy required for a dislocation, subjected to τ_{eff}, to overcome the discrete obstacles controlling the creep rate. The one hour constant-force indentation creep tests provide data from which σ_{ind} and $\dot{\varepsilon}_{ind}$ can be calculated as a function of time. $\Delta G(\tau_{eff})$ can then be determined by applying Eq. (5.3) along with the following expressions for the equivalent indentation shear stress τ_{ind}, τ_{eff} and the apparent equivalent indentation shear strain rate $\dot{\gamma}_{ind}$

$$\tau_{ind} = \frac{\sigma_{ind}}{3\sqrt{3}} \qquad \tau_{eff} = \frac{\sigma_{ind} - \sigma_{ind\,t=1hr}}{3\sqrt{3}} \text{ and } \dot{\gamma}_{ind} = \sqrt{3}\dot{\varepsilon}_{ind} = \frac{\sqrt{3}\dot{h}}{h} \tag{5.4}$$

The apparent activation energy required for a dislocation to move past the discrete obstacles, ΔG_0, can be determined by extrapolating the $\Delta G(\tau_{eff})$ versus τ_{eff} trends, obtained from each indentation creep test, to τ_{eff} = 0 [24-28]. Figure 5.3 shows ΔG_0, normalized with respect to μb^3 where *b* is the Burgers vector, versus the level of ion irradiation damage. While ΔG_0 increases with increasing irradiation damage, and its magnitude is essentially independent of indentation direction, its magnitude is slightly lower, for a given level of dpa, when the Zr^+ irradiation occurs at 300°C than when it occurs at 25°C. This suggests that the crystallographic damage resulting from the Zr^+ ion irradiation is slightly less effective at impeding dislocation glide when the irradiation is performed at 300°C than at 25°C.

5.4 Conclusions

The effect of Zr^+ ion irradiation at 300°C on increasing the indentation hardness, decreasing the anisotropy of the indentation hardness, and increasing the apparent activation energy ΔG_0 of the indentation creep rate of extruded and cold drawn Zr-2.5%Nb CANDU pressure tube material was studied.

The increase in the initial indentation stress $\sigma_{ind_{t=0}}$ with increasing levels of Zr^+ ion irradiation at 300°C was lower than that reported earlier for Zr^+ irradiation performed at 25°C [13, 14]. The ratio of $\sigma_{ind_{t=0}}$ on the TN plane relative to that on either the AN or RN planes decreased significantly with increasing Zr^+ ion irradiation indicating that the anisotropy of the indentation stress decreased however the level of the decrease was less than when the Zr^+ ion irradiation was performed at 25°C. The relative change in indentation stress $\Delta\hat{\sigma}_{ind}$, for any level of irradiation damage, decreases with increasing resolved fraction of basal poles in the indentation direction. The fact that the Zr-2.5%Nb test material was strongly textured with the majority of the (0001) basal plane normals aligned in the transverse direction of the tubing and the fact that this alloy deforms primarily by prismatic and pyramidal dislocation glide, suggest that the crystallographic damage resulting from the Zr^+ ion irradiation has a greater effect on blocking the movement of dislocations on prismatic than on pyramidal slip systems.

The apparent activation energy of the obstacles that limit the rate of dislocation glide during indentation creep did not change with indentation direction but increased with increasing levels of Zr^+ ion damage. The values of ΔG_0 were, however, lower when the Zr^+ irradiation was performed at 300°C rather than 25°C.

These observed differences in the indentation deformation of Zr-2.5%Nb samples irradiated with Zr^+ ions at 25°C and at 300°C indicate the effect that concurrent thermal annealing has on the accumulation of irradiation damage at 300°C. The effect of irradiation temperature on reducing the degree of, and the strength of, irradiation damage obstacles must therefore be considered when predicting the strength and thermal creep behaviour of irradiated nuclear materials.

5.5 Acknowledgements

The authors wish to acknowledge the financial support of the Natural Science and Engineering Research Council of Canada (NSERC) and the University Network of Excellence in Nuclear Engineering (UNENE) for their financial support of this research through a collaborative research grant.

5.6 References

[1] P.A. Ross-Ross, V. Fidleris, D.E. Fraser, Canadian Metallurgical Quarterly, v. 11 (1972), p. 101

[2] P.A. Ross-Ross, W. Evans, W.J. Langford, Atomic Energy of Canada Ltd Research Report, AECL-4262 (1972), p. 1

[3] A.R. Causey, V. Fidleris, S.R. MacEwen, C.W. Schulte, Influence of Radiation on Material Properties: 13th Intl. Symp. (1987), p. 54

[4] A.R. Causey, A.G. Norsworthy, C.W. Schultes, Can. Metall. Quart., v. 24 (1984), p. 207

[5] N. Christodoulou, P.A. Turner., E.T.C. Ho, C.K. Chow, M.R. Levi, Metall. and Mat. Trans. A., v. 31A (2000), p. 409

[6] N. Christodoulou, A.R. Causey, R.A. Holt, C.N. Tomé, N. Badie, R.J. Klassen, R. Sauvé, C.H. Woo, Zirconium in the nuclear industry: Eleventh Int. Symp.(1996), p. 518

[7] B.S. Rodchenkov, A.N. Semenov, Nucl. Eng. And Design, v. 235 (2005), p. 2009

[8] E.F. Ibrahim, J. of Nucl. Mat., v. 101 (1981), p. 1

[9] E.F. Ibrahim, R.A. Holt, J. of Nucl. Mat., v. 91 (1980), p. 311

[10] R.A. Holt, N. Christodoulou, A.R. Causey, J. of Nucl. Mat., v. 317 (2003), p. 256

[11] D.D. Himbeault, C.K. Chow, M.P. Plus, Metall. And Mater. Trans. A, v. 25 (1994), p. 135

[12] R.A. Holt, G.A. Bickel, N. Christodoulou, J. of Nucl. Mat., v. 373 (2008), p. 130

[13] B. Bose, R.J. Klassen, J. of Nucl. Mat., v. 405(2010), p. 138

[14] B. Bose, R.J. Klassen, J. of Nucl. Mat., v. 399(2010), p. 32

[15] N.A. Fleck, G.M. Mullar, M.F. Ashby, J.W. Hutchinson, Acta Metall. Mater., v.42 (1994), p. 475

[16] W. D. Nix, H. Gao, J. Mech. Phys. Solids, v. 46 (1998), p. 411.

[17] M. F. Ashby, Philos. Mag., v. 21 (1970), p. 399.

[18] Q. Ma, D. R. Clarke, J. Mater. Res., v. 10 (1995), p. 853

[19] H. Li, A. H. W. Ngan, J. Mater. Res., v. 19 (2004), p. 513

[20] W.J. Poole, M.F. Ashby, N.A. Fleck, Scripta Mater., v. 34 (1996), p. 559

[21] A. A. Elmustafa, D. S. Stone, J. Mech. Phys. Solids, v. 51 (2003), p. 357

[22] A. A. Elmustafa, D.S. Stone, Materials Letters, v. 57 (2003), p. 1072

[23] A. A. Elmustafa, D.S. Stone, Mater. Sci. Eng, A, v. 358 (2003), p. 1

[24] V. Bhakhri and R. J. Klassen, J. Mater. Sci., v. 41 (2006), p. 2259

[25] V. Bhakhri and R. J. Klassen, J. Mater. Sci., v. 41 (2006), p. 2249

[26] V. Bhakhri and R. J. Klassen, Scripta Mater., v. 55 (2006), p. 395

[27] B. Bose and R. J. Klassen, Mat. Sci. and Eng. A., v. 500 (2009), p.164

[28] R. J. Klassen, B. J. Diak and S. Saimoto, Mater. Sci. Eng. A, v. 387-389(2004), p. 297

[29] H. J. Frost and M. F. Ashby, Deformation-Mechanism Maps, Pergamon Press, Oxford (1982)

.

Chapter 6

6 Temperature dependence of the anisotropic deformation of Zr-2.5%Nb pressure tube material during micro-indentation*

In the previous chapters all the indentation tests were performed at 25^{o}C to assess the effect of indentation depth, irradiation hardening and irradiation temperature on the deformation kinetics and the mechanical anisotropy of Zr-2.5%Nb pressure tube material. In the present investigation, the indentation tests were performed over the temperature range from 25 to 400^{o}C to assess the temperature dependence of the anisotropy of the deformation parameters of the non-irradiated Zr-2.5%Nb pressure tube material.

6.1 Introduction

Zr-2.5%Nb pressure tubes, used for many years in the primary coolant loop of CANDU nuclear reactors, are mechanically anisotropic due to their highly textured microstructure however the degree of anisotropy, and the microstructural factors that dictate the anisotropy, over the temperature range up to and beyond 310^{o}C (the current service temperature of these pressure tubes in a CANDU reactor) is not completely characterized or understood. Most mechanical tests of such tubes are performed under uniaxial or biaxial loading in the axial and transverse (circumferential) directions of the tube. The flow stress and ductility resulting from loading in the radial, through thickness, direction

---

* A version of this chapter was published in the Journal of Nuclear Materials, Volume 419, Issue 1-3, December 2011, Pages 235–240.

is still seldom measured due to the practical difficulty of preparing and testing small specimens cut from the 4 mm thick tubes. A comparison of the temperature dependence of the flow stress, ductility, and activation energy associated with plastic deformation in the radial, axial, and transverse directions of Zr-2.5%Nb pressure tubes has therefore not been reported. These data are, however, very important for developing constitutive equations capable of accurately predicting the deformation of this material when it is subjected to high multiaxial loadings at their 250 – 310^{o}C service temperature.

Pyramidal micro-indentation testing is a method of assessing the local mechanical properties of small volumes of material. The technique is thus potentially well suited for characterizing the mechanical anisotropy of Zr-2.5%Nb pressure tubes. Constant-force pyramidal indentation tests provide data that depict simultaneously decreasing indentation stress and indentation velocity. Since the indentation stress is related to the yield stress of the material, these data can be analyzed to assess the strain rate dependence of the yield stress. It is essential to realize that the actual state of stress and strain any point beneath the indentation is constantly changing, thus any measured changes in the magnitude of, or the strain rate dependence of, the indentation stress provide only a qualitative indication of the nature of the operative deformation mechanisms within the indented material. The precision of the qualitative data for assessing quantitatively the characteristics of the operative deformation mechanisms must always be verified by comparisons with data from conventional constant uniaxial stress and constant uniaxial strain rate tests.

In previous investigations we have successfully used pyramidal micro-indentation to assess the anisotropy of the flow stress and the activation energy of the plastic deformation of extruded and cold-drawn Zr-2.5%Nb pressure tubes at 25^{o}C in both the non-irradiated and the Zr^{+} ion irradiated conditions [9-11]. In the present investigation we use the same technique to assess the temperature dependence of the anisotropy of the flow stress and the activation energy of the plastic deformation of non-irradiated Zr-2.5%Nb pressure tube material over the temperature range from 25 to 400^{o}C. We compare our findings with what data are available on the effect of temperature on the

directional anisotropy of the yield stress of the Zr-2.5%Nb material to assess their quantitative accuracy.

The directional anisotropy of the flow stress and ductility of Zr-2.5%Nb pressure tubes may change at elevated temperature since both parameters are influenced by factors such as the onset of increased deformation by twinning, increased ease for dislocation cross slip, enhanced dislocation climb and impaired dislocation velocity resulting from increased mobility of oxygen solute atoms [1-8]. These factors may affect the flow stress and ductility in one direction of the textured pressure tube more than in another. We use the data obtained from our micro-indentation tests to show that a previously proposed description of deformation operating by either prismatic or pyramidal dislocation glide is consistent with the qualitative observations of the temperature dependence of the anisotropic indentation stress of the cold-worked Zr-2.5%Nb pressure tube material.

6.2 Experimental Procedure

This investigation was performed on extruded and 27% cold-drawn Zr-2.5%Nb CANDU pressure tube material supplied, in the non-irradiated condition, by the Atomic Energy of Canada Ltd. The microstructure of this material consists of hcp α-Zr grains, elongated in the axial direction of the tube, surrounded by a thin discontinuous layer of Nb-rich bcc β precipitates. The α grains have average dimensions of about 0.2, 1.0 and 5.0 μm in the radial, transverse and axial directions of the tube respectively. The α grains are textured with the majority of the (0001) basal plane normals aligned along the transverse direction of the tube [12]. The calculated fraction of basal pole normals aligned in the axial, radial, and transverse directions of this pressure tube are $F_A = 0.031$, $F_R = 0.340$, and $F_T = 0.629$ respectively. Other details regarding the fabrication and microstructure of this material can be found elsewhere [9, 12-14].

Rectangular samples, 8.5 mm long, 8.5 mm wide and about 4 mm thick, were cut from the as-received pressure tube. The Axial Normal (AN), Radial Normal (RN), and the

Transverse Normal (TN) sides (Figure 6.1) of selected samples were prepared by mechanical grinding, mechanical polishing, and then chemical attack polishing. The average roughness of the polished surface was about ± 8 nm as measured with atomic force microscopy.

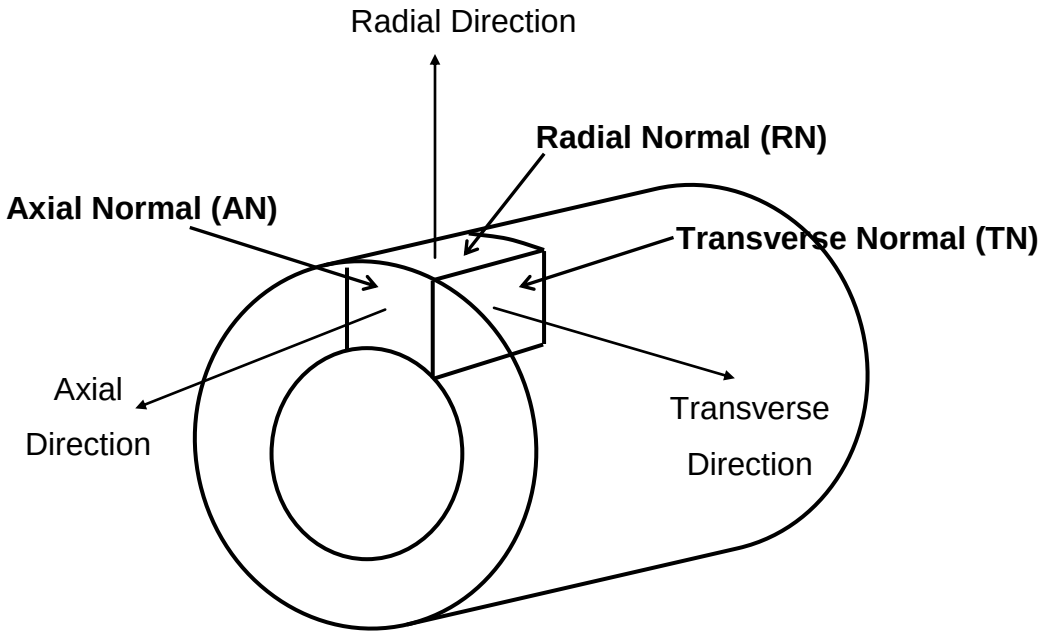

Figure 6.1: Orientation of the test specimens extracted from the Zr-2.5%Nb pressure tube.

Micro-indentation tests were carried out in air at 25, 200, 300 and 400°C on the polished surfaces of the samples. The maximum thickness of oxide layer formed on these samples after testing at the highest temperature, 400°C, was about 200 ± 50 nm. Micro-indentation tests were performed to indentation depths of $h \geq 5.0$ μm using an instrumented micro-indentation testing platform (Micro Materials ltd, Wrexham, UK) with separate, independently PID controlled, heaters attached to the specimen stage and the indenter. A diamond Berkovich indenter was used for the 25^{o}C tests while a sapphire

Berkovich indenter was used for the high-temperature tests. Each micro-indentation test consisted of two stages: i) a loading stage where the indentation force *F* was increased at a constant rate until the desired *h* was reached followed by ii) a constant *F* stage of 300 second duration over which *h* was recorded. Between 7 and 15 micro-indentation tests were performed at each temperature on each of the AN, RN and TN surfaces.

6.3 Results

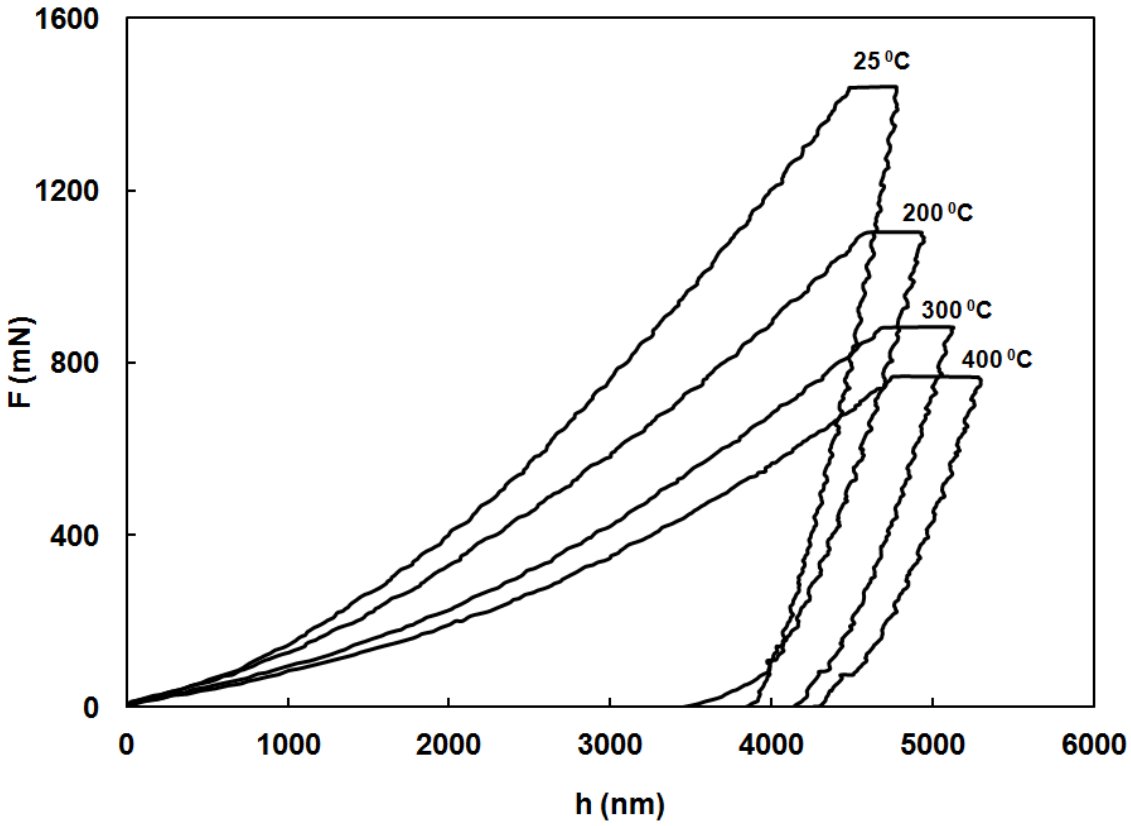

Figure 6.2: Typical indentation force (*F*) vs. indentation depth (*h*) curves at different test temperature for indentations made on the TN plane of the Zr-2.5%Nb material.

Typical plots of *F* versus *h* are shown in Figure 6.2 for one micro-indentation test performed, on the TN surface, at each of the four test temperatures. The curves show clearly the decreasing indentation force, for a given *h*, with increasing temperature.

Figure 6.3(a) shows *h* versus time *t* over the constant *F* stage of the same indentation tests shown in Figure 6.2. The plots illustrate the increased indentation creep rate at the elevated temperature. Figure 6.3(b) shows the *h* versus *t* data from all the indentation tests performed on the TN surface at 400^{o}C. The degree of scatter in *h* during the constant *F* creep tests is relatively small even at this the highest test temperature. This indicates that the indentation response of the test material is not significantly affected by grain-to-grain variations in the microstructure (i.e. variations in the dislocation density) of the test material. This is consistent with the fact that the indentation creep tests were performed at indentation depths greater than several micrometers and the indentation response, therefore, reflects the average deformation over a volume encompassing multiple grains.

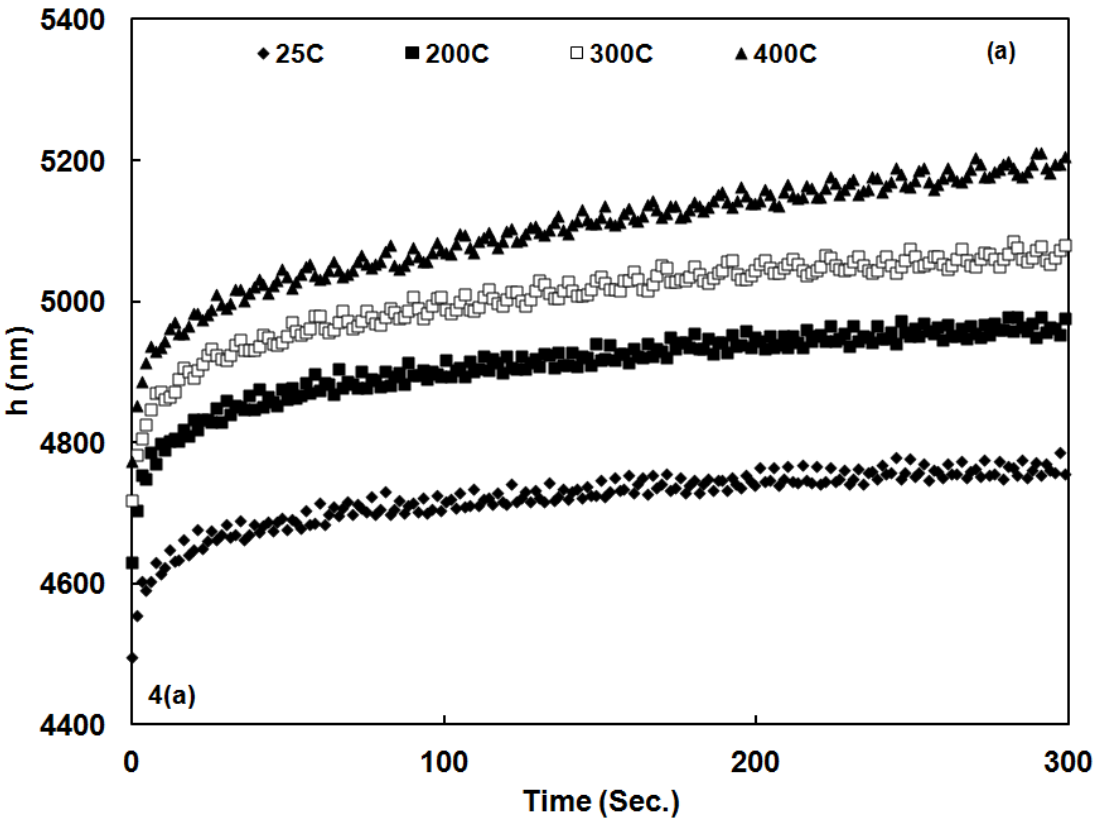

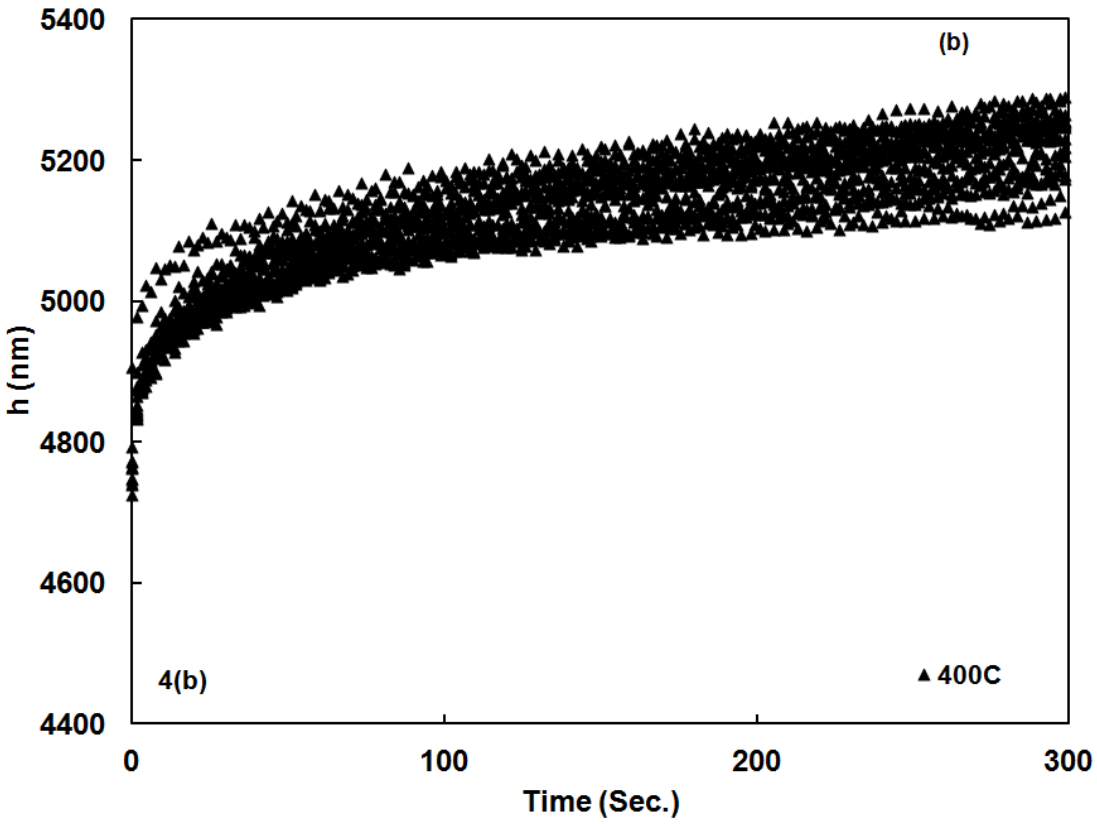

Figure 6.3: (a) Indentation depth *h* versus time (*t*) over the 300 second constant-load stage of indentation tests performed on the TN plane of the Zr-2.5%Nb material at 25, 200, 300 and 400°C. (b) Plots of *h* versus *t* for all tests carried out at 400°C on the TN plane.

Figure 6.4 shows the average indentation stress σ_{ind} versus *t* for the tests shown in Figure 6.2. σ_{ind} was calculated as

$$\sigma_{ind} = \frac{F}{24.5Ch^2} \tag{6.1}$$

where, $24.5h^2$ is the projected area of an ideal Berkovich indentation and *C* is a constant that accounts for the effect of sink-in and pile-up on the actual projected indentation area. The constant *C* was obtained from SEM measurement of the actual projected area of

indentations of various depths. σ_{ind} decreases with increasing time due to the fact that h increases by creep deformation while F remains constant. Plots of similar profile as those shown in Figure 6.4 but of different magnitude were obtained from the micro-indentations performed on the AN and RN surfaces.

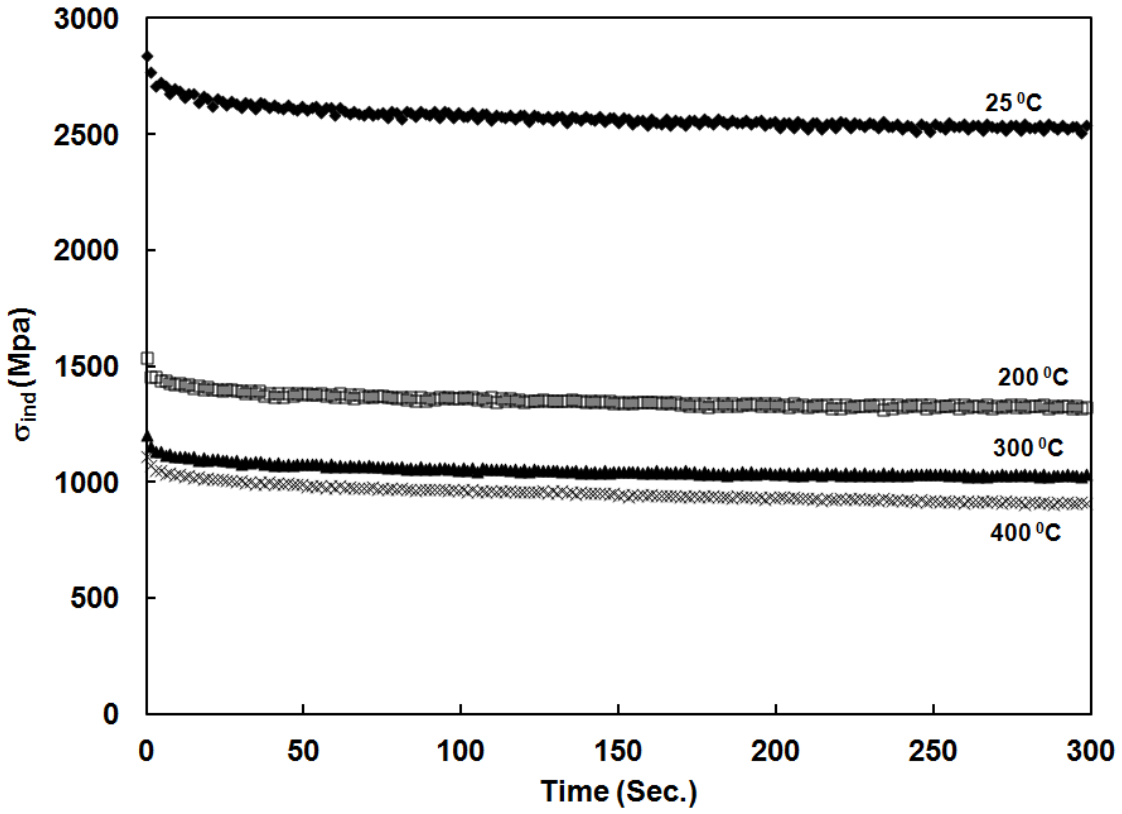

Figure 6.4: Typical decrease in average indentation stress (σ_{ind}) with time (t) for the same tests shown in Figure 6.3.

6.4 Discussion

Plastic deformation occurs in the Zr-2.5%Nb alloy by dislocation glide upon either prismatic $\{10\bar{1}0\}\langle\bar{1}2\bar{1}0\rangle$ or pyramidal $\{10\bar{1}1\}\langle\bar{1}\,\bar{1}23\rangle$ slip systems. The extruded and

cold-drawn Zr-2.5%Nb pressure tubes display significantly higher yield stress in the transverse direction primarily because their crystallographic texture, with the majority of $\{0001\}$ poles aligned in the transverse direction, requires that plastic flow occur primarily by the more difficult $\{10\bar{1}1\}\langle\bar{1}\,\bar{1}23\rangle$ pyramidal slip [1, 15-17]. The directional anisotropy of the flow stress of Zr-2.5%Nb pressure tubes is related to both the strength of the obstacles that limit dislocation glide upon these slip systems and the alignment of slip systems relative to the direction of loading. In the following sections we analyze the effect of temperature upon the anisotropy of both the initial indentation stress and the activation energy of the indentation deformation rate. We compare the values of the measured indentation stress and activation energy with previously reported data, obtained from conventional constant-stress and constant-strain rate testing, to assess the quantitative accuracy of our data. We then use our data, along with a very simple description of indentation in terms of dislocation slip on systems most closely aligned with the indentation direction to demonstrate how the observed temperature dependence of both the anisotropy of the indentation stress and the activation energy for indentation creep can be explained in terms of the temperature dependence of dislocation glide on both prismatic and pyramidal slip systems.

6.4.1 Temperature dependence of the anisotropy of the initial indentation stress

Figure 6.5 shows the initial indentation stress $\sigma_{ind_{t=0}}$, calculated with Eq.(6.1) at the start of the constant *F* stage of each indentation test, versus temperature. The indentation depth *h* corresponding to $\sigma_{ind_{t=0}}$ is between 4 and 5 μm and is sufficiently deep that $\sigma_{ind_{t=0}}$ is essentially independent of *h*. The measured $\sigma_{ind_{t=0}}$ in all three indentation directions decreases with increasing temperature and reflects the expected decrease in the flow stress with increasing temperature.

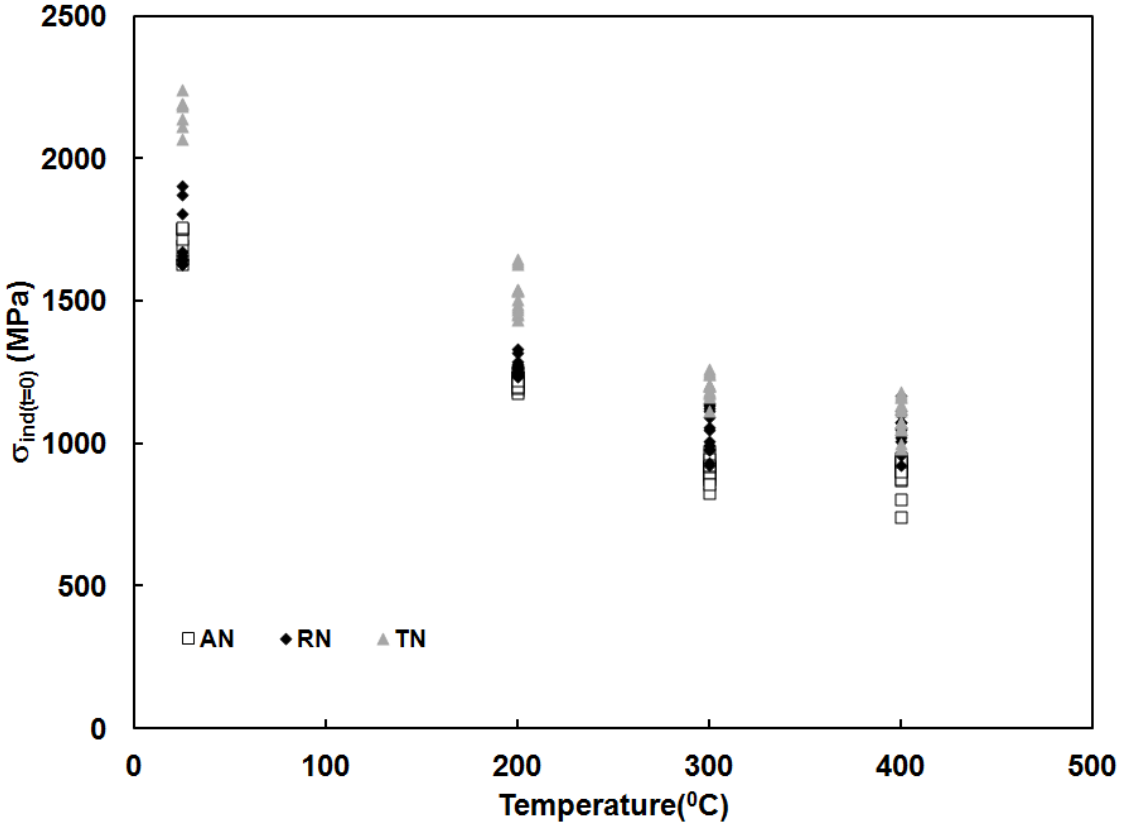

Figure 6.5: Initial indentation stress, $\sigma_{ind\,t=0}$, versus temperature for indentation tests performed on the AN, RN, an TN planes of the Zr-2.5%Nb pressure tube material.

The anisotropy of the flow stress of Zr-2.5%Nb pressure tube material is reflected by $\sigma_{ind\,t=0}$ being highest, at any given temperature, for indentations made in the transverse direction (i.e. on the TN plane). The stress ratios $\sigma_{ind_{t=0}}(TN)/\sigma_{ind_{t=0}}(AN)$ and $\sigma_{ind_{t=0}}(TN)/\sigma_{ind_{t=0}}(RN)$ are plotted versus temperature in Figure 6.6. The ratios are essentially equal, $\sigma_{ind_{t=0}}(TN)/\sigma_{ind_{t=0}}(AN)=1.29$ and $\sigma_{ind_{t=0}}(TN)/\sigma_{ind_{t=0}}(RN)=1.26$, at 25°C but diverge with increasing temperature until $\sigma_{ind_{t=0}}(TN)/\sigma_{ind_{t=0}}(AN)=1.22$ and $\sigma_{ind_{t=0}}(TN)/\sigma_{ind_{t=0}}(RN)=1.05$ at 400°C. Similar decreases in the anisotropy of the flow

stress of Zr-2.5%Nb have been previously reported from uniaxial stress tests performed in the axial and the transverse directions [4,19]. The difference between $\sigma_{ind_{t=0}}(TN)/\sigma_{ind_{t=0}}(AN)$ and $\sigma_{ind_{t=0}}(TN)/\sigma_{ind_{t=0}}(RN)$ is very small, approx 3%, at 25°C but increases to approximately 11% at 300°C and 26% at 400°C. This indicates that the flow stress in the radial direction follows different temperature dependence than that in the axial direction.

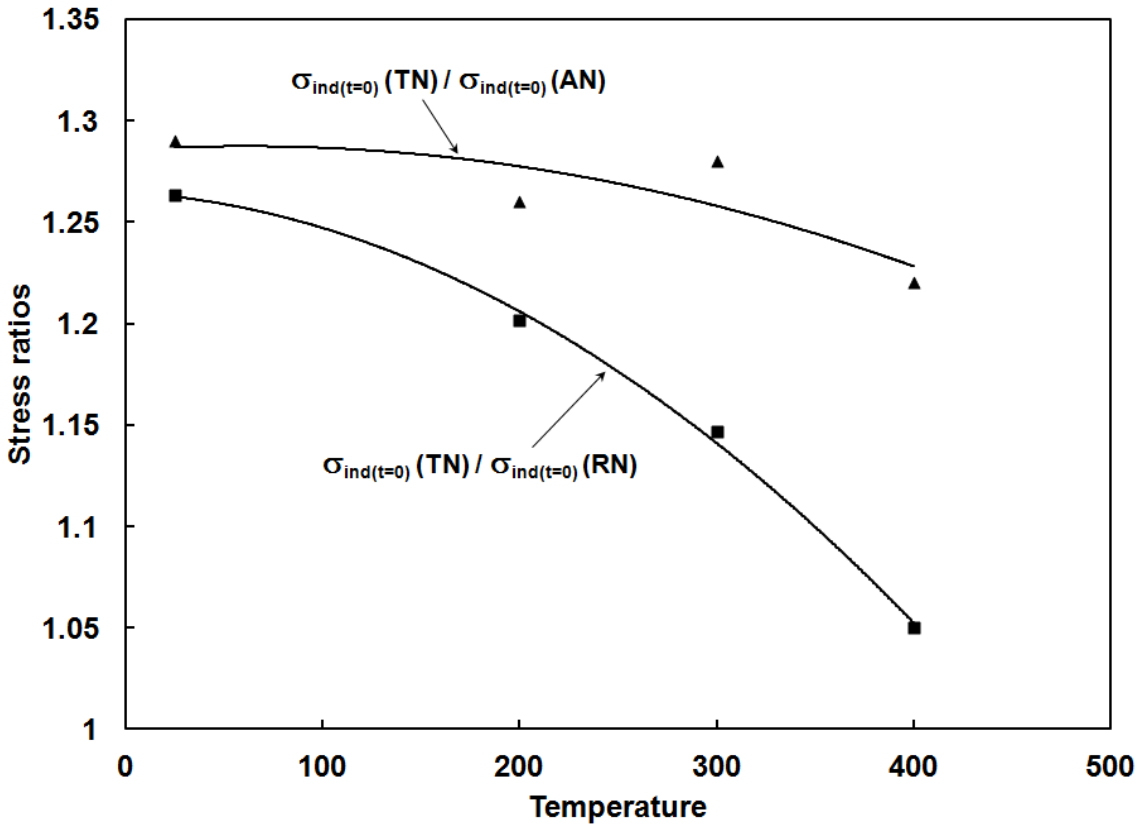

Figure 6.6: Initial indentation stress ratios, $\sigma_{ind\,t=0}(TN)/\sigma_{ind\,t=0}(AN)$ and $\sigma_{ind\,t=0}(TN)/\sigma_{ind\,t=0}(RN)$ versus temperature. The shape of the curves indicates that the degree of anisotropy of the flow stress of the Zr-2.5%Nb pressure tube material changes with temperature.

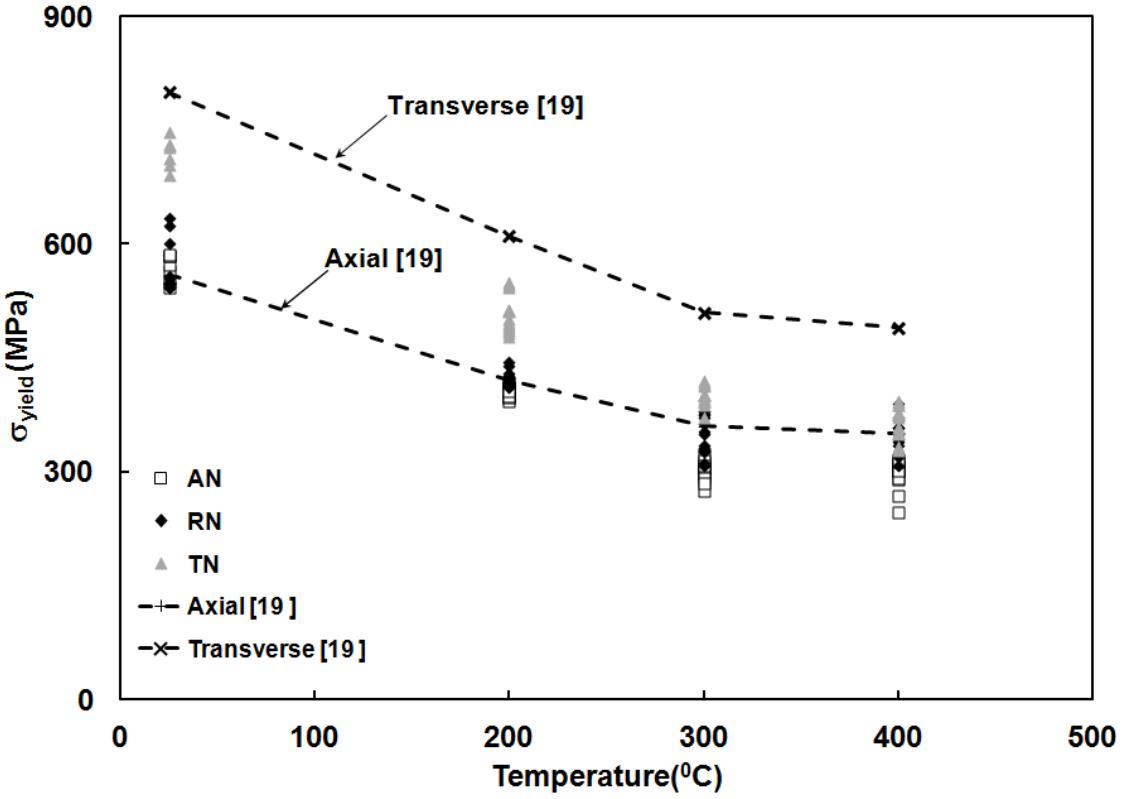

Figure 6.7: Previously published uniaxial yield stress data versus temperature for Zr and Zr-Nb alloys. Included in the plot are equivalent yield stress data calculated from the initial indentation stress data shown in Figure 6.6 with the equation $\sigma_{yield} \approx \sigma_{ind_{t=0}} / 3$.

Early studies have indicated that the pyramidal indentation hardness of a wide range of ductile, isotropic, bcc and fcc metals is approximately equal to three times the uniaxial flow stress of the metal. The indentation hardness is greater in magnitude than the uniaxial flow stress primarily because of large hydrostatic stress resulting from the geometric constraint imposed by the undeformed material surrounding the indentation [18]. Previously reported values of the uniaxial flow stress in the axial and the transverse directions of Zr-2.5%Nb pressure tubes are plotted as a function of temperature in Figure 6.7. Included in this plot are values of $\sigma_{ind_{t=o}} / 3$ from this study. The data from the

micro-indentation tests performed in the axial direction (i.e. indentations made on the AN plane) correspond quite closely to those obtained from previously reported uniaxial tensile test data from the axial direction of Zr-2.5%Nb pressure tubes as shown by the data from Reference [19] in Figure 6.7. The data from micro-indentation tests performed in the transverse direction (i.e. on the TN plane) are consistently lower, by about 20%, than those obtained from uniaxial tensile tests in the transverse direction of Zr-2.5%Nb pressure tubes. We conclude therefore that, for the extruded and cold-worked Zr-2.5Nb pressure tube material studied here, the measured initial indentation stress $\sigma_{ind_{t=o}}$ can predict the actual uniaxial flow stress to within about 20% when the simple relation $\sigma_{yield} = \sigma_{ind_{t=o}}/3$ is used. A more detailed explanation for the difference between $\sigma_{ind\,t=0}(TN)/3$ and $\sigma_{yield}(TN)$ which is based upon differences in the operative slip mechanisms is proposed below.

Our observation that $\sigma_{ind\,t=0}(TN)$ is larger than $\sigma_{ind\,t=0}(AN)$ or $\sigma_{ind\,t=0}(RN)$ is in agreement with the common knowledge that the flow stress of Zr-2.5%Nb pressure tube material is significantly larger in the transverse direction than in either the axial or the radial directions. This arises from the fact that the majority of $\{0001\}$ basal pole normals of the hcp α-grains, the primary microstructural constituent of these tubes, are aligned in the transverse direction of the tube. Plastic deformation in the transverse direction must therefore occur by a larger proportion of dislocation glide on the $\{10\bar{1}1\}\langle\bar{1}\,\bar{1}23\rangle$ pyramidal slip system compared to deformation in the axial or radial directions where more of the deformation can occur by dislocation glide on the $\{10\bar{1}0\}\langle\bar{1}2\bar{1}0\rangle$ prismatic slip system. In the case of the indentation tests performed in this study considerable plastic flow must also occur in directions other than the indentation direction in order to accommodate the pyramidal indenter. $\sigma_{ind\,t=0}(TN)$ must therefore reflect a combination of the stress required for plastic flow in the transverse direction of the tube, which could be expected to occur by pyramidal slip, and also the stress necessary for concurrent slip in the axial and radial directions, which occurs by prismatic slip. This would explain why the equivalent yield stress obtained from micro-indentation on the TN plane falls between

the lines describing the uniaxial flow stress in the transverse and the axial directions (Figure 6.7).

Figures 6.5 and 6.7 indicate that the flow stress of the Zr-2.5Nb decreases linearly with increasing temperature to a temperature of about 300°C and then continues to decrease, but at a slower rate, to 400^{o}C. Several mechanisms can account for this observation. A. Akhtar [1] found that the critical resolved shear stress for prismatic slip in Zr single crystals, decreases with increasing temperature until reaching a temperature independent plateau between 327 and 527°C. This may explain the observed decreased rate of softening between 300 and 400^{o}C for indentation made on the AN and RN planes. It has also been reported that, when deformation of polycrystalline Zr occurs by pyramidal slip, deformation above 300^{o}C can occur by a combination of twinning plus <c+a> dislocation glide [2, 5]. The onset of twinning at temperature above 300°C may therefore result in a slower decrease of $\sigma_{ind\,t=0}$ for the indentations made on the TN surface where the majority of the c-axes of the α-grains are aligned parallel to the direction of indentation.

The slower rate of decrease in $\sigma_{ind\,t=0}$ at temperature above 300^{o}C could also be a manifestation of dynamic strain aging, associated with the interaction of dissolved oxygen atoms with the gliding dislocations. Such a phenomenon often occurs in zirconium based alloys at around 400°C [1,8, 20,21]. Dynamic strain aging usually results in large transients appearing in the stress-strain response leading to considerable scatter in the flow stress data. Such anomalous behaviour and scatter are, however, absent in the indentation data at 400^{o}C in our data (Figure 6.3(b)).

6.4.2 Temperature dependence of the activation energy of indentation deformation

The local equivalent stress directly beneath the pyramidal indentations in this study is very high and corresponds to the equivalent flow stress of the indented material. The plastic indentation strain rate during the constant *F* stage of the indentation tests occurs, because of the high stress, by a mechanism of time-dependent, thermally-activated

obstacle-limited dislocation glide. The shear strain rate $\dot{\gamma}$ resulting from the operation of such a mechanism can be expressed in terms of the effective applied shear stress τ_{eff}, the yield stress in shear τ_{yield}, and temperature T as [22]

$$\dot{\gamma} = \dot{\gamma}_p \left(\frac{\tau_{yield}}{\mu(T)} \right)^2 e^{-\frac{\Delta G(\tau_{eff})}{kT}} \tag{6.2}$$

where $\dot{\gamma}_p$ is a constant (we use $\dot{\gamma}_p = 10^{11} s^{-1}$ [23]), μ(T) is the elastic shear modulus at temperature T, k is Boltzmann's constant and $\Delta G(\tau_{eff})$ is the thermal energy required for a dislocation, subjected to τ_{eff}, to overcome the obstacles controlling the creep rate. The constant F indentation creep tests provide data from which σ_{ind} and $\dot{\varepsilon}_{ind}$ can be calculated as a function of time. $\Delta G(\tau_{eff})$ can then be determined by applying Eqs. (6.1 and 6.2) along with the following expressions for the equivalent indentation shear stress τ_{ind}, τ_{eff} and the apparent equivalent indentation shear strain rate $\dot{\gamma}_{ind}$ [23]

$$\tau_{ind} = \frac{\sigma_{ind}}{3\sqrt{3}} \qquad \tau_{eff} = \frac{\sigma_{ind} - \sigma_{ind\,t=300s}}{3\sqrt{3}} \textbf{ and } \dot{\gamma}_{ind} = \sqrt{3}\dot{\varepsilon}_{ind} = \frac{\sqrt{3}}{h}\left(\frac{dh}{dt}\right) \tag{6.3}$$

The apparent activation energy, ΔG_0, required for a dislocation to move past the obstacle can be determined by extrapolating the $\Delta G(\tau_{eff})$ versus τ_{eff} trends, obtained from each indentation creep test, to τ_{eff} = 0. The dependence of the average ΔG_0 upon temperature for indentation creep tests perform on the AN, RN and TN planes is shown in Figure 6.8. The average ΔG_0 increases linearly from 0.72 to 1.33 eV with increasing temperature from 25 to 300°C. Over this temperature range ΔG_0 is of about the same magnitude for indentations performed on any of the planes and is also of the same magnitude as previously reported values for the activation energy of plastic deformation of similar zirconium alloys [1, 8-10, 19, 24, 25]. This confirms that the qualitative data obtained from constant F indentation creep tests when analysed with Equations (6.1 – 6.3) yield

apparent activation energy values for Zr-2.5%Nb that are quantitatively very accurate when compared to data obtained from constant uniaxial stress creep tests.

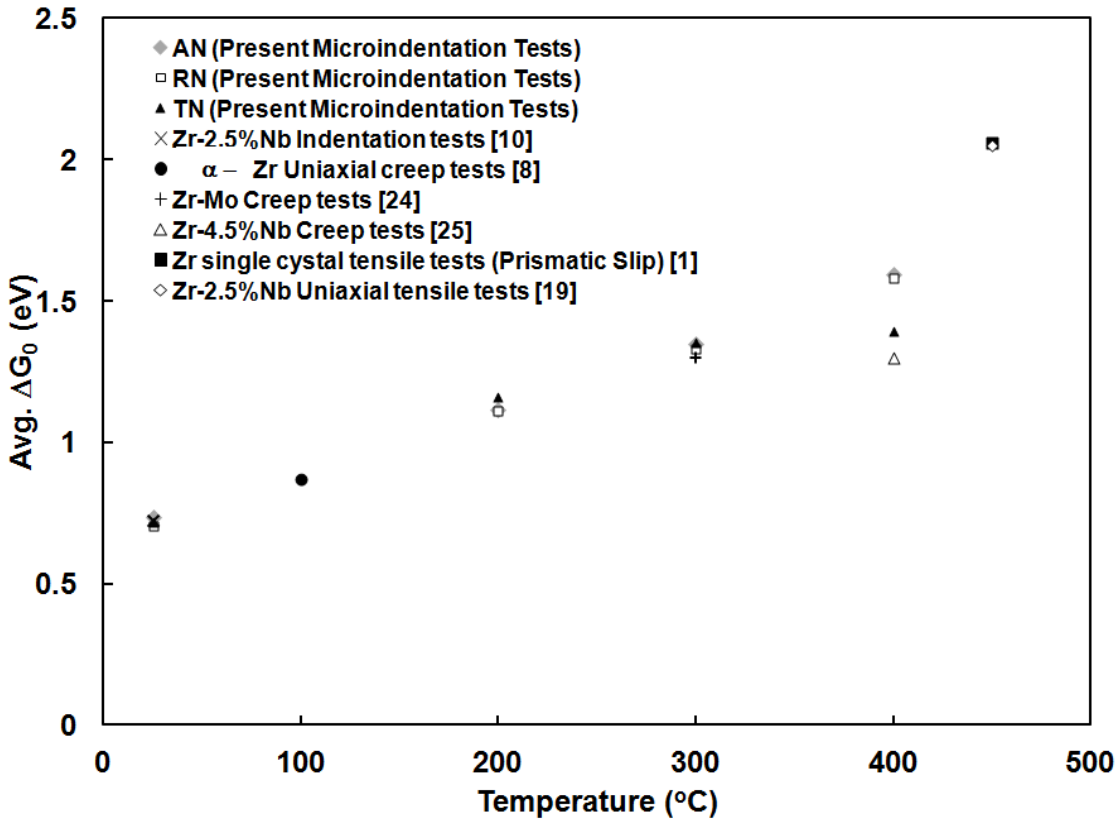

Figure 6.8: Increase in the average ΔG_0 with temperature. This plot shows activation energies from previously published tests along with data from this investigation.

While ΔG_0 continues to increase to 400°C, our data indicate that, at this high temperature, a difference arises between ΔG_0 from tests performed on the TN plane compared with those performed on the AN or the RN planes. The average ΔG_0 for indentation on the TN plane changes from 1.33 eV at 300°C to 1.37 eV at 400°C while

the average ΔG_0 for indentation on the AN and RN planes changes from 1.33 eV at 300°C to 1.64 eV at 400°C.

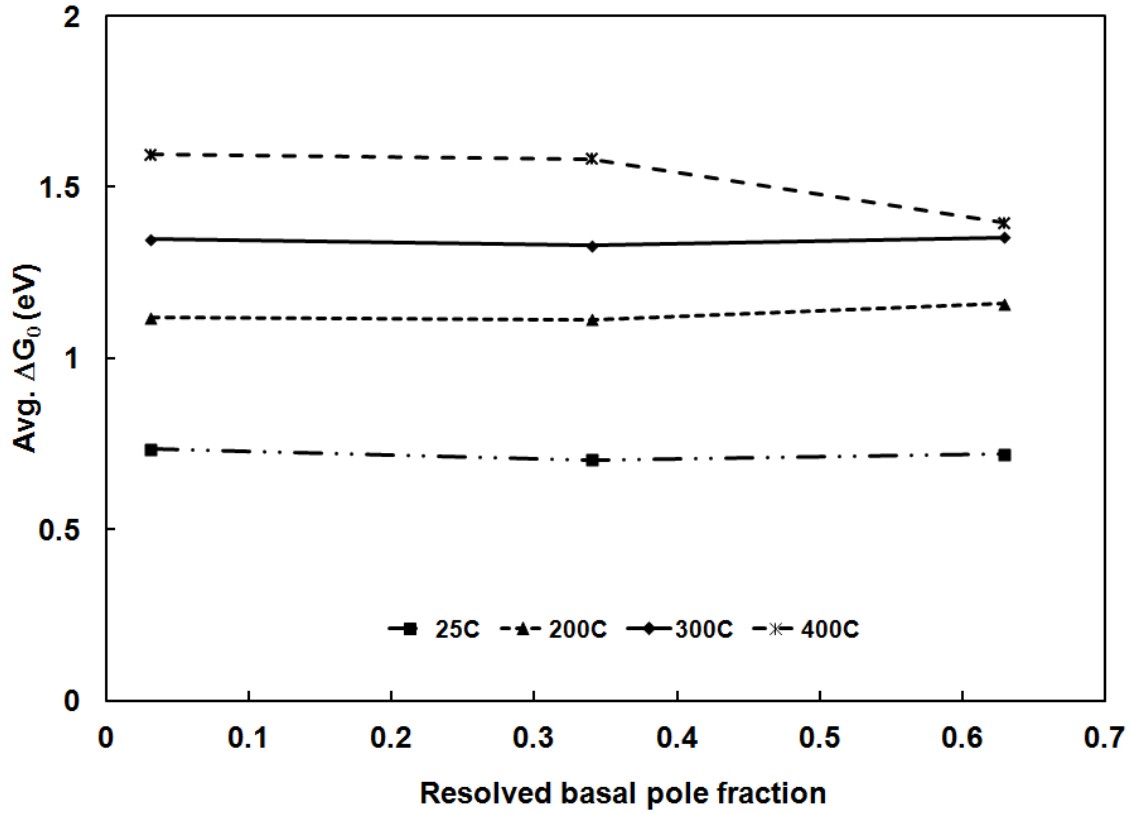

Figure 6.9: Average ΔG_0 versus the resolved basal pole fraction in the direction of indentation. ΔG_0 is independent of the basal pole fraction except at the highest temperature (400°C) where ΔG_0 is significantly lowered when the basal pole fraction is large.

Figure 6.9 shows the average ΔG_0 plotted against the resolved fraction of basal poles in the indentation direction. Since ΔG_0, for a given temperature less than about 300°C, is not dependent upon the resolved basal pole fraction in the indentation direction, the activation strength of obstacles to dislocation glide during the indentation process does

not depend upon whether the deformation occurs by prismatic or pyramidal slip. At temperature greater than 300°C, ΔG_0 does not continue to increase at the same rate when indentations are made in a direction that contains many basal poles. Since plastic deformation in the direction of the basal poles occurs primarily by pyramidal dislocation glide we can deduce that the strength of the obstacles that limit the time-dependent glide of dislocations on the $\{10\bar{1}1\}\langle\bar{1}\,\bar{1}23\rangle$ pyramidal slip system changes between 300 and 400°C relative to the strength of obstacles limiting dislocation glide on the $\{10\bar{1}0\}\langle\bar{1}2\bar{1}0\rangle$ prismatic slip system. This may reflect the increased contribution of twinning to the total plastic deformation during pyramidal dislocation glide as proposed in References [2,5].

6.5 Conclusions

In this paper we report data on the effect of temperature on the micro-indentation stress and the activation energy for indentation creep performed on the AN, RN, and TN surfaces of extruded and cold-drawn Zr-2.5%Nb pressure tubes over the temperature range from 25 to 400°C.

Pyramidal micro-indentation invokes complex triaxial stress and strains within the indented material and thus can provide, at best, qualitative data on the mechanical response of the indented material. We show, however, that the equivalent flow stress and the activation energy of the deformation process obtained from micro-indentation tests of extruded and cold-drawn Zr-2.5%Nb pressure tube material are quantitatively quite accurate, within about 20%, when compared with equivalent data obtained from constant uniaxial stress and constant uniaxial strain rate tests. Having established this quantitative accuracy we are able to interpret the observed temperature dependence of the anisotropic indentation stress and the temperature dependence of the activation energy of the indentation deformation rate in terms of the operation of dislocation slip along the slip systems that are most favourably aligned with the indentation direction with the understanding that considerable amounts of slip must also occur in directions other than the indentation direction.

The ratio of the indentation stress in the transverse direction relative to that in the axial and radial directions was 1.29:1 and 1.26:1 at 25^{o}C but decreased to 1.22:1 and 1.05:1 at 400^{O}C. This represents a difference in only about 3% at 25^{o}C but approximately 11% and 26% at 300^{o}C and 400^{o}C respectively and suggests that the flow stress in the radial direction therefore follows different temperature dependence than that in the axial direction. This finding has not been reported previously because of the dearth of available data on the temperature dependence of the radial flow stress of the Zr-2.5%Nb pressure tube material.

The average activation energy ΔG_0 of obstacles that limit the rate of indentation creep increases from 0.72 to 1.33 eV with increasing temperature from 25 to 300^{o}C. Over this temperature range ΔG_0 is not dependent upon the direction of indentation and compares very closely in magnitude to equivalent data obtained from constant uniaxial stress creep tests performed on similar Zr alloys. We conclude therefore that the activation strength of obstacles that control the dislocation glide during the indentation process does not depend upon the relative proportion of deformation occurring by prismatic or pyramidal slip.

At temperature greater than 300^{o}C, ΔG_0 increase at a slower rate when indentations are made in transverse direction compared to when they are made in the radial or axial directions of the pressure tube. Since plastic deformation in the transverse direction occurs primarily by pyramidal dislocation glide this suggests that the strength of the obstacles that limit the time-dependent glide of dislocations on the $\{10\bar{1}1\}\langle\bar{1}\,\bar{1}23\rangle$ pyramidal slip system changes between 300 and 400^{o}C relative to the strength of obstacles limiting dislocation glide on the $\{10\bar{1}0\}\langle\bar{1}2\bar{1}0\rangle$ prismatic slip system and may reflect the increased contribution of twinning to the total plastic deformation during pyramidal dislocation glide.

The findings presented in this paper provide new insight into: i) the necessary methodology for interpreting micro-indentation test data through direct comparison with conventional constant uniaxial stress or uniaxial strain rate data and ii) the temperature dependence of the anisotropy of the flow stress and the plastic strain rate of Zr-2.5%Nb

pressure tube material. In particular the assessment of the temperature dependence of σ_{yield} and ΔG_0 in the radial direction of the pressure tube is previously unreported. These data will be very useful in the development of new micro-indentation based testing methodologies or validation of generalized constitutive equations to predict the strain response under high-magnitude multiaxial stress loadings of Zr-2.5%Nb pressure tube material at temperature in the range up to the 250 to 300^{o}C service temperature of this material.

6.6 Acknowledgements

The authors wish to thank the Natural Science and Engineering Research Council of Canada (NSERC) and the University Network of Excellence in Nuclear Engineering (UNENE) who provided financial support for this research. The assistance of Dr. T. Simpson of the University of Western Ontario Nanofabrication Laboratory in preparing the TEM foils is gratefully acknowledged. Finally, we offer a special note of thanks to Mr. B. Leitch of the Atomic Energy of Canada Ltd (Chalk River Laboratories) for providing the Zr-2.5%Nb pressure tube material used in this study.

6.7 References

[1] A. Akhtar, Metall. Trans. A, v. 6 (1975), p. 1217

[2] A. Akhtar, J. of Nucl. Mat., v. 47 (1973), p. 279

[3] A. Salinas-Rodriguez., M.G. Akben, J.J. Jonas, E.F. Ibrahim, Canadian Metallurgical Quarterly, v. 24 (1985), p. 259

[4] B.S. Rodchenkov, A.N. Semenov, Nucl. Eng. And Design, v. 235 (2005), p. 2009

[5] J. A. Jensen, W.A. Backofen, Canadian Metallurgical Quarterly, v. 11 (1972), p. 39

[6] K. Kapoor, K. Muralidharan, K.M. Sreedharan, J. of Mat. Eng. and Performance v. 4 (1995), p. 610

[7] V. Ramachandran, R.E. Reed-Hill, Metall. Trans., v. 1(1970), p. 2105

[8] R.D. Warda, V. Fidleris, E. Teghtsoonian, Metall. Trans., v. 4 (1973), p. 1201

[9] B. Bose, R.J. Klassen, J. of Nucl. Mat., v. 399 (2010), p. 32

[10] B. Bose, R.J. Klassen, J. of Nucl. Mat., v. 405(2010), p. 138

[11] B. Bose, R.J. Klassen, MRS Proceedings, v. 1298 (2011), p. mrsf10-1298-q07-02

[12] M. Griffiths, C.K. Chow, C.E. Coleman, R.A Holt, S. Sagat, V.F. Urbanic, Atomic Energy of Canada Ltd Research Report, AECL-10844 (1993), p. 1

[13] N. Christodoulou, P.A. Turner., C.N. Tomé., C.K. Chow, R.J. Klassen, Metall. and Mat. Trans. A., v. 33 (2002), p. 1103

[14] V. Perovic, G.C. Weatherly, R.G. Fleck, Can. Metall. Quart., v. 24 (1985), p. 253

[15] R.A. Holt, M. Griffiths, R.W. Gilbert, J. of Nucl. Mat., v. 149 (1987), p. 51

[16] E. Tenckhoff, J of ASTM Int., v. 2 (2005), p. 119

[17] M. Griffiths, J. of Nucl. Mat., v. 205 (1993), p. 225

[18] D. Tabor, Microindentation Techniques in Material Science and Engineering (edited by P.J. Blau and B. R. Lawn), ASTM special Publ. (1985), p. 129

[19] N. Christodoulou, P.A. Turner., E.T.C. Ho, C.K. Chow, M.R. Levi, Metall. and Mat. Trans. A., v. 31A (2000), p. 409

[20] K. Källström, M. Svenzon, Scand. J. Metallurgy, v. 2 (1973), p. 55

[21] J.S. Ahn, S.W. Nam, Mat. Lett., v. 9(1990), p. 413

[22] U.F. Kocks, A.S. Argon, M.F. Ashby, Prog. Mat. Sci., v. 19 (1975), p. 1

[23] H. J. Frost and M. F. Ashby, Deformation-Mechanism Maps, Pergamon Press, Oxford (1982)

[24] M. Pahutova, J Cadek, J. of Nucl. Mat., v. 68 (1977), p. 111

[25] M. Pahutova, J Cadek, V. Cenry, J. of Nucl. Mat., v. 61 (1976), p. 28

Chapter 7

7 Characterizing the deformation kinetics of Zr-2.5%Nb pressure tube material using micro-indentation strain rate change testing

7.1 Introduction

Micro-indentation testing incorporating high precision strain rate changes (PSRC) can be used to characterize the strain rate sensitivity of the flow stress of a metal under conditions of essentially constant microstructure [1-4]. While this technique has been applied to date on only relatively simple fcc metal systems, it has tremendous potential for obtaining fundamental information on the operative deformation mechanisms of microstructurally complex materials including those used in the nuclear industry.

The most obvious factor that influences the performance of structural components in the core of a nuclear reactor is the high level of fast neutron irradiation. In past studies [5-8], we have used constant-load indentation creep tests to assess the effect of Zr^+ irradiation, as a simulation of neutron irradiation, on the apparent activation strength ΔG_0 of the irradiation induced microstructural obstacles the limit the rate of dislocation glide of extruded and cold-drawn Zr-2.5%Nb CANDU reactor pressure tubes. We observed that Zr^+ irradiation increased ΔG_0 in this material. One of the problems associated with analyzing data obtained from constant-load pyramidal indentation creep tests is that the microstructure around the indentation changes continuously over the course of the test. More fundamental information could be obtained by using PSRC indentation tests to assess the effect of Zr^+ irradiation on the deformation of Zr-2.5%Nb under conditions of essentially constant microstructure. In this paper we present the results of such an investigation. To introduce this work we first briefly describe the underlying principles associated with PSRC micro-indentation tests.

7.1.1 PSRC micro-indentation testing

The PSRC micro-indentation testing technique was developed by Saimoto et al. [1-3] and carries on from high precision strain rate change testing performed in uniaxial tension [9]. The technique involves performing a constant velocity micro-indention test with a pyramidal indenter that is driven with a piezoelectric actuator. Periodically during the test the indentation velocity is suddenly decreased by factor of ten. Superimposed upon this decrease is a sudden indentation displacement that is applied with the actuator. The magnitude of this displacement step is selected to exactly nullify the elastic recovery of the indenter load frame and the specimen that results from the sudden decrease in the sample flow stress due to the decreased indentation strain rate. In this fashion, the plastic indentation depth $h_{plastic}$ does not change despite the factor of ten change in the indentation velocity. This allows the determination of the strain rate sensitivity of the average indentation stress, which is directly related to the flow stress, of the indented material under conditions of essentially constant microstructure. From these data fundamental deformation parameters, such as the apparent activation volume, V', activation area $\Delta a'$ and activation work $\Delta W'$ characteristic of the operative obstacle-limited dislocation glide process can be determined [10].

The following general form of equation is commonly used to express the shear strain rate $\dot{\gamma}$ as a function of the applied stress τ and temperature T of a material that is undergoing plastic deformation by a mechanism of time-dependent, thermally-activated, obstacle-limited dislocation glide [11]

$$\dot{\gamma} = \dot{\gamma}_0 \exp\left(-\frac{\Delta G(\tau)}{kT}\right) \tag{7.1}$$

In this equation $\dot{\gamma}_0$ is a factor related to the mobile dislocation density and the frequency of atomic vibration within the deforming material, $\Delta G(\tau)$ is the stress dependent thermal activation energy necessary to overcome the obstacles that limit the dislocation glide, and k is the Boltzmann's constant. The thermal activation energy $\Delta G(\tau)$ can be expressed in terms of the difference between the total apparent activation energy ΔG_0 of the obstacle

and the work delivered to the dislocation by the applied shear stress τ as the dislocation moves past the obstacle as

$$\Delta G(\tau) = \Delta G_0 - \tau V' \tag{7.2}$$

where $V' = b\Delta a'$ represents the apparent activation volume associated with the dislocation-obstacle interaction, b is the Burgers vector of the dislocation, and $\Delta a'$ is the apparent activation area covered by the dislocation as it overcomes the obstacle.

Substituting Eq. (7.2) into Eq. (7.1) and taking the derivative of $\ln \dot{\gamma}$ with respect to τ under conditions of constant T and microstructure, Σ, gives

$$\left.\frac{\partial \ln \dot{\gamma}}{\partial \tau}\right|_{T,\Sigma} = \frac{V'}{kT} - \frac{1}{kT}\left.\frac{\partial \Delta G_0}{\partial \tau}\right|_{T,\Sigma} + \left.\frac{\partial \ln(\dot{\gamma}_0)}{\partial \tau}\right|_{T,\Sigma} \tag{7.3}$$

Since, under conditions of constant microstructure, the parameters ΔG_0 and $\dot{\gamma}_0$ are not dependent upon the applied stress τ, Eq. (7.3) can be simplified and the apparent activation volume V' can be expressed in terms of the strain rate sensitivity of τ as [11],

$$\frac{V'}{kT} = \left.\frac{\partial \ln \dot{\gamma}}{\partial \tau}\right|_{T,\Sigma} \tag{7.4}$$

When indentation tests are preformed with a perfect three-sided pyramidal, Berkovich, indenter the average indentation stress is expressed as a function of the indentation force F and depth h as

$$\sigma_{ind} = \frac{F}{24.5h^2} \tag{7.5}$$

Although σ_{ind} represents a complex multi-axial stress state within the indented material, it has been demonstrated that, for indentations made in ductile metals, σ_{ind} is equivalent to the application of a uniaxial characteristic shear stress τ as [12]

$$\sigma_{ind} = 3M\tau \tag{7.6}$$

Where, M is the Taylor factor and for hcp materials, such as the Zr-2.5%Nb studied in this paper, has a value in the range from 3.5 to 4 [13,14].

During indentation with a geometrically self-similar pyramidal indenter, the indentation depth h is the only independent length parameter. The average strain rate associated with such an indentation must therefore be proportional to the ratio of the indentation velocity $\dot{h}/h$. Without knowing the exact proportionality constant, we can assign the constant as unity and express the *apparent* average indentation shear strain rate as

$$\dot{\gamma}_{ind} = \frac{\dot{h}}{h} \tag{7.7}$$

Substituting Eqs. (7.6) and (7.7) into Eq. (7.4) allows us to express the V' and $\Delta a'$ of the operative obstacle-limited dislocation glide process during a constant microstructure indentation strain rate change in terms of the change of the average indentation stress $\Delta\sigma_{ind}$ resulting from a change of the natural logarithm of the strain rate $\Delta\ln\left(\dot{h}/h\right)$ as

$$V' = b\Delta a' = 3MkT\left.\frac{\Delta\ln\left(\dot{h}/h\right)}{\Delta\sigma_{ind}}\right|_{T,\Sigma} \tag{7.8}$$

In what follows we describe PSRS micro-indentation tests performed on samples cut from extruded and cold-drawn Zr-2.5%Nb CANDU pressure tube material to assess the dependence of V' and $\Delta a'$ upon indentation depth, and prior Zr^{+} irradiation. This has clear implications for improving our understanding, and our ability to predict, the effect of irradiation on the mechanical properties of this important nuclear material.

7.2 Experimental procedure

7.2.1 Test material

This investigation was performed on extruded and 27% cold-drawn Zr-2.5%Nb CANDU pressure tube material supplied, in the non-irradiated condition, by the Atomic Energy of Canada Ltd (Chalk River laboratories). Rectangular samples, 8.5 mm long, 8.5 mm wide and 4.0 mm thick, were cut from the pressure tube. The Radial-Normal (RN) surface, orthogonal to the radial direction of the pressure tube, of each sample was prepared by mechanical grinding and polishing followed by chemical polishing. The average roughness of the final polished surface was about ± 8 nm as measured with atomic force microscopy.

7.2.2 Zr^+ irradiation

Some of the polished samples were exposed to 8.5 MeV Zr^+ ions to a fluence of 7.07×10^{15} ions/cm^2. The ion irradiation was performed at 25^{o}C in vacuum (10^{-11} Pa) in a 1.7 MV tandem ion accelerator at the Western University in London Ontario Canada. Simulations carried out with the SRIM (Stopping Range of Ions in Materials) software indicate that the maximum interaction of the 8.5 MeV Zr^+ ions within the Zr-2.5%Nb alloy occurs at a depth between 2.0 and 2.5 μm and corresponds, at that depth, to a maximum crystal damage of about 30 displacements per atom (dpa).

7.2.3 PSRC micro-indentation tests

Micro-indentation tests were performed at 25^{o}C with a custom built, computer-controlled, micro-indenter consisting of a Berkovich diamond that was driven by a PZT piezoelectric actuator. A semiconductor-type load cell, with a load capacity of 0.50 N and a ± 2 μN load resolution, was positioned in series with the indenter and the sample. The indentation rate was controlled at a constant 0.05μm/s and the indentation depth and load

were recorded at intervals of 0.02 s over the duration of the micro-indentation test. Each test involved making an indentation of depth greater than 3 μm into the polished RN surface of the Zr-2.5%Nb sample. Sudden indentation velocity changes where performed, at indentation depths of 0.5, 1.0, 1.5, 2.0, 2.5 and 3.0 μm, during each micro-indentation test. The strain rate changes involved suddenly reducing the indentation velocity from 0.05 to 0.005 μm/s. This reduced velocity was maintained for several seconds before returning to 0.05 μm/s. A sudden step increase in the indentation depth was applied via the piezoelectric actuator to superimpose exactly with each indentation velocity change in order to compensate for the changed elastic deflection of the indenter load frame and the sample and result in an indentation strain rate change that occurs at essentially constant $h_{plastic}$. By this method the change in indentation stress $\Delta\sigma_{ind}$ resulting from a sudden factor of ten reduction in $\dot{\gamma}_{ind}$ performed under essentially constant microstructure conditions was measured at six indentation depths, from 0.5 to 3.0 μm, from each micro-indentation test.

7.3 Results and Discussions

A typical indentation force *F* versus indentation depth *h* curve from one micro-indentation PSRC test performed on the RN plane of a non-irradiated Zr-2.5%Nb pressure tube material is shown in Figure 7.1. Changes in the strain rate result in the perturbations in the *F* – *h* curve at depths of *h* = 0.5, 1.0, 1.5, 2.0, 2.5 and 3.0 μm. Figure 7.2 shows the the average indentation stress σ_{ind} and the plastic indentation depth $h_{plastic}$ plotted versus time during the strain rate change performed, at *h* = 1 μm, on the non-irradiated sample shown in Figure 7.1. The figure indicates that $h_{plastic}$ remains essentially unchanged during the strain rate change. This indicates that the strain rate change was performed under conditions of essentially constant microstructure.

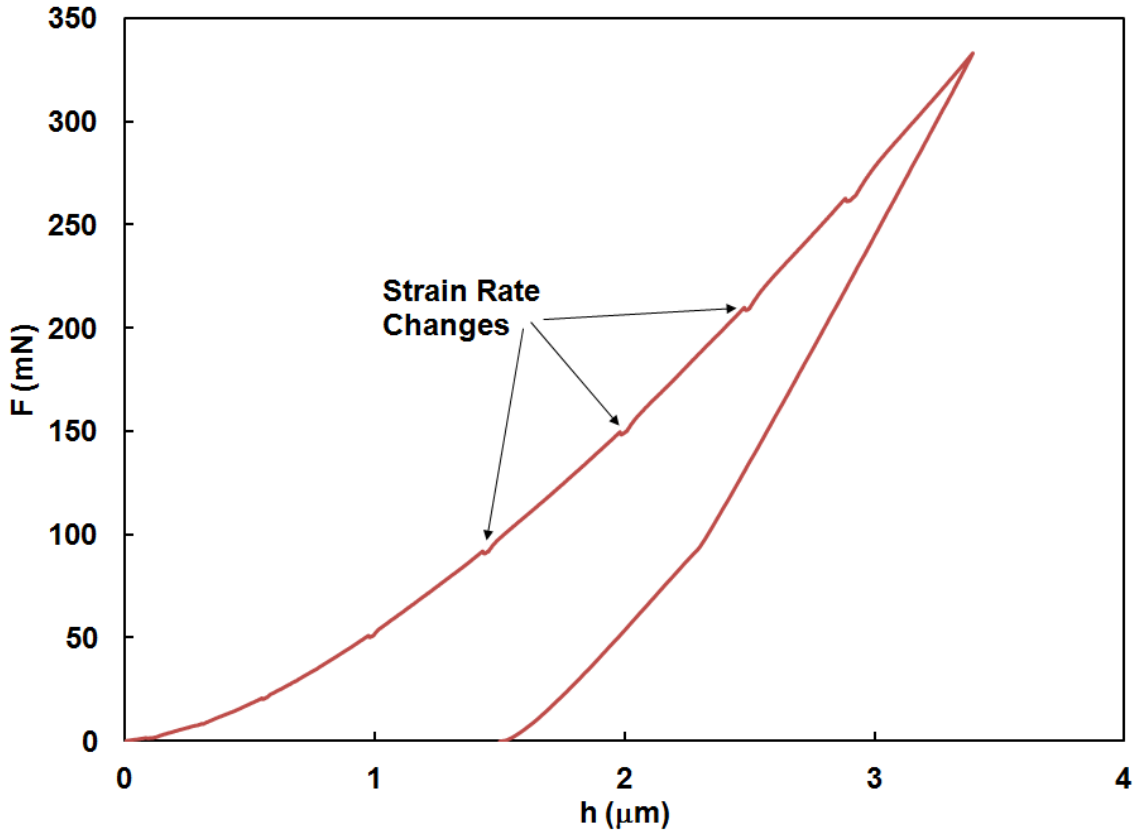

Figure 7.1: Typical indentation force *F* versus depth *h* plot from a PSRC micro-indentation test performed, at 25°C, on the RN plane of a non-irradiated Zr-2.5%Nb sample. The small perturbation of the curve at *h* = 0.5, 1.0, 1.5, 2.0, 2.5, and 3.0 μm indicate where the strain rate changes occurred.

Figure 7.3 shows σ_{ind} plotted versus indentation depth *h* for the non-irradiated and 30 dpa Zr^{+} irradiated Zr-2.5%Nb pressure tube samples. The values of σ_{ind} correspond to the values of indentation stress just before each strain rate change. σ_{ind} decreases with increasing *h* for both conditions but, for a given indentation depth, σ_{ind} is higher for the Zr^{+} irradiated condition. These observations are similar to what was previously reported from constant-load indentation creep tests performed on same material [5]. The dependence of σ_{ind} upon *h* is consistent with the indentation depth dependence of the

hardness of many ductile materials [15-19] and this phenomenon has been well studied and will not be discussed further here.

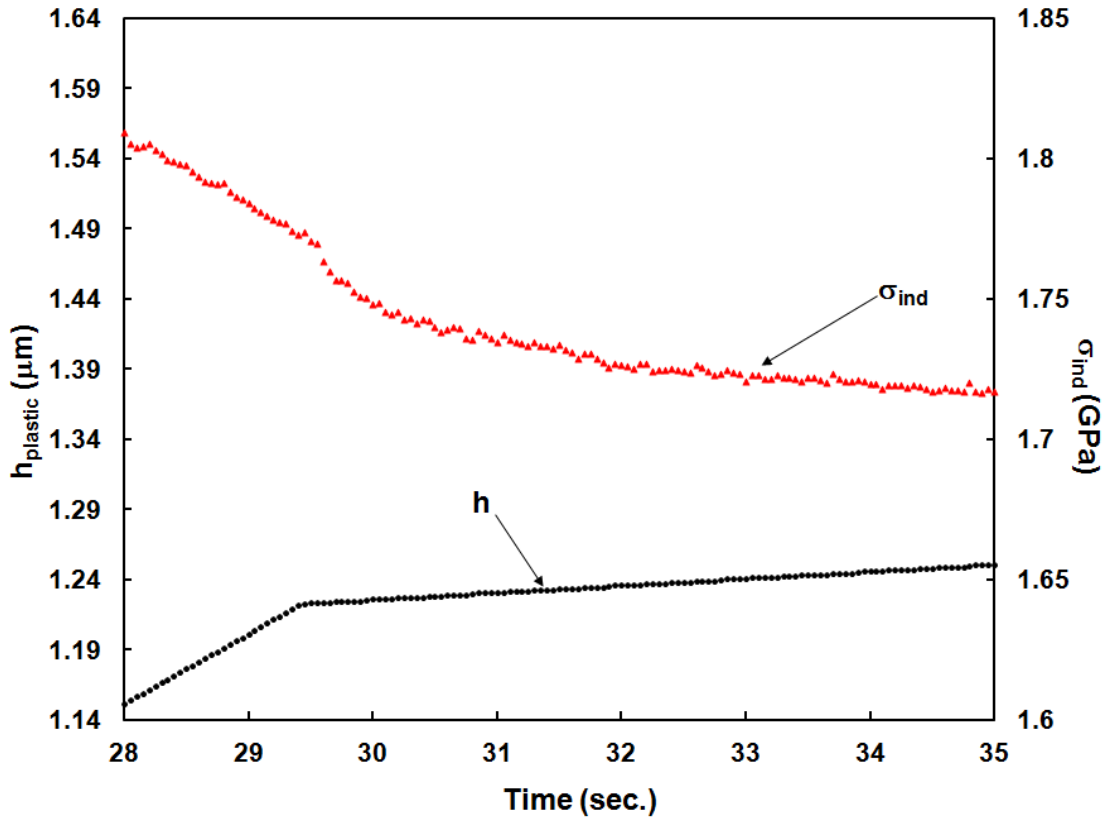

Figure 7.2: Average indentation stress σ_{ind} and plastic indentation depth $h_{plastic}$ versus time for a strain rate change performed at h = 1.0 μm on the sample shown in Fig. 7.1. The figure indicates that $h_{plastic}$ does not change appreciably during the strain rate change indicating that the strain rate was changed under essentially constant strain rate conditions. The change in indentation stress $\Delta\sigma_{ind}$ resulting from the factor of ten strain rate change is indicated on the figure.

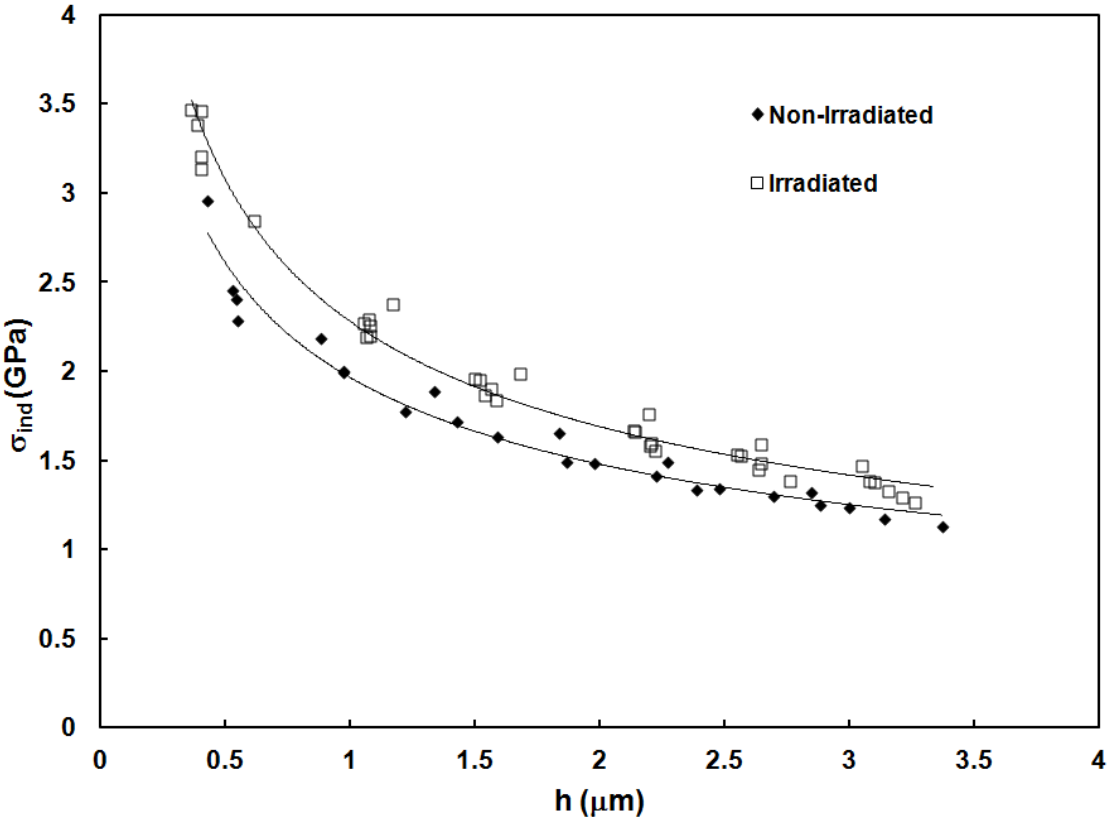

Figure 7.3: Average indentation stress σ_{ind} plotted versus the indentation depth h for the non-irradiated and the Zr^{+} irradiated Zr-2.5%Nb material.

7.3.1 The strain rate sensitivity of σ_{ind} in the Zr-2.5%Nb alloy

The strain rate sensitivity m of $\tau = \sigma_{ind}/3M$ can be determined from the measured $\Delta\sigma_{ind}$ determined from the individual indentation strain rate changes as

$$m = \frac{\Delta \log \tau}{\Delta \log \dot{\gamma}_{ind}} \tag{7.9}$$

Figure 7.4 shows m plotted against the indentation depth for the non-irradiated and the Zr^{+} irradiated Zr-2.5%Nb material. The strain rate sensitivity m increases with decreasing

h. A similar indentation depth dependence of *m* was recently reported by Haghshenas et al [20] who performed micro-indentation tests at various indentation velocities on 6061 aluminum alloy samples such that they were able to determine *m* at specific indentation depths. The depth dependence of *m* suggests that details of the mechanism of time-dependent plastic deformation are indentation depth dependant for the Zr-2.5%Nb material studied here as it is for other materials.

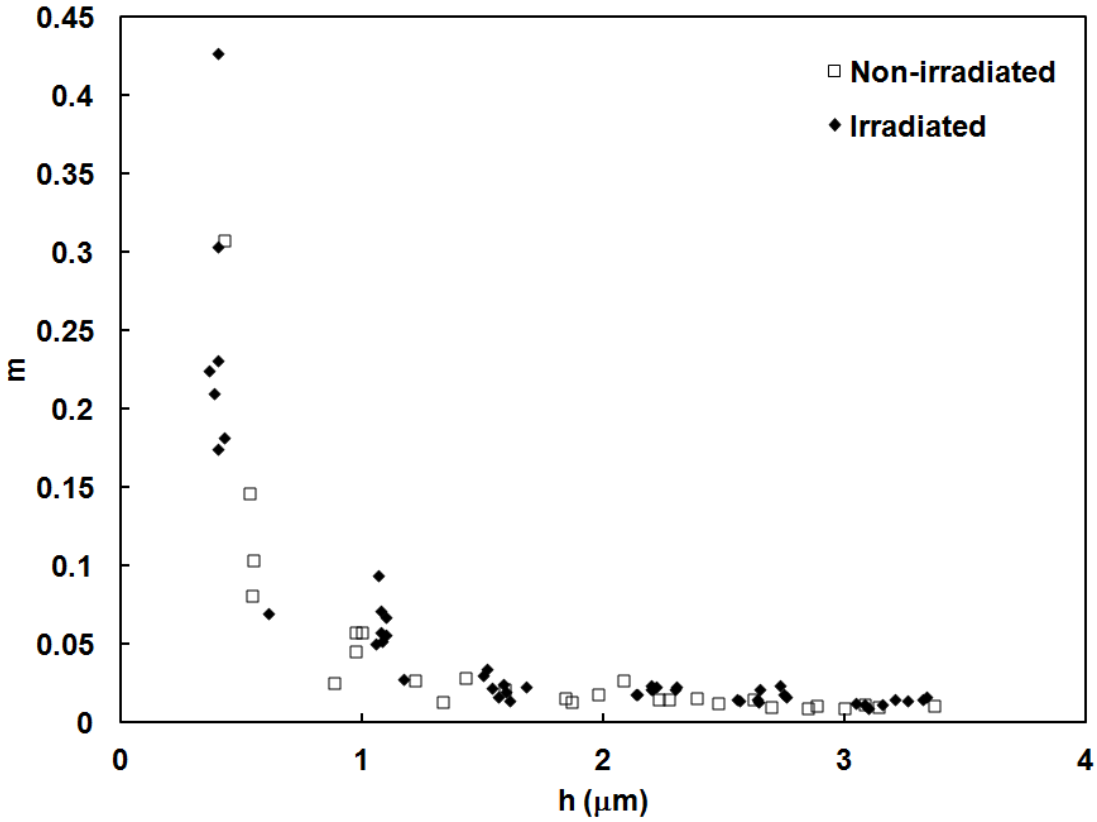

Figure 7.4: Strain rate sensitivity *m* of σ_{ind}, determined from the constant microstructure strain rate change data, versus the indentation depth *h* for the non-irradiated and the Zr^{+} irradiated Zr-2.5%Nb material.

Figure 7.4 indicates that magnitude of m obtained from the deepest indentations this study is about m = 0.01 and 0.013 for the non-irradiated and the Zr^+ irradiated material. These values are of similar magnitude as values of m = 0.011 to 0.02 measured from conventional constant strain rate unixial tensile tests performed on pure Zr and a variety of Zr-Nb alloys of similar composition and hcp crystal structure to the Zr-2.5%Nb studied here [21-23].

7.3.2 Analysis of V' and $\Delta a'$

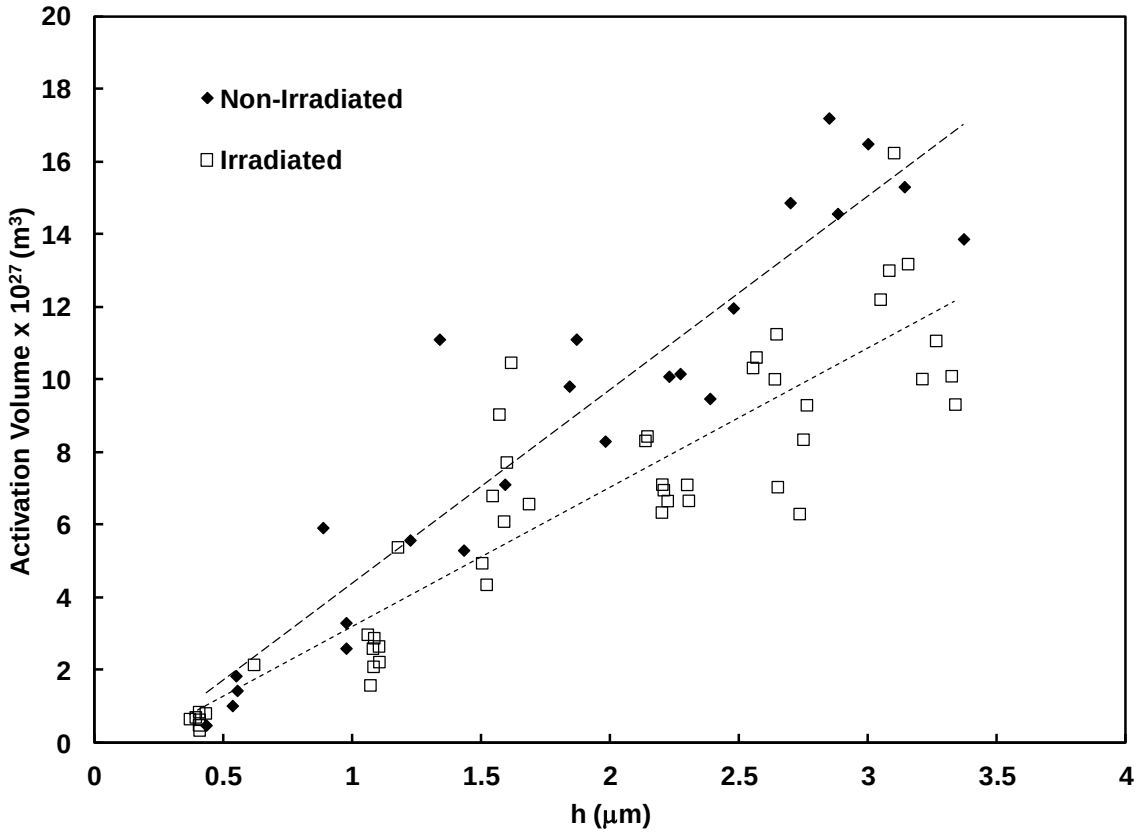

Figure 7.5: Apparent activation volume V' (Eq. 7.8) versus the indentation depth h for the non-irradiated and the Zr^+ irradiated Zr-2.5%Nb material.

The $\Delta\sigma_{ind}$ data obtained from the strain rate changes performed in this study were used, along with Eq. 7.8, to calculate the apparent activation volume V' and the apparent activation area $\Delta a'$ that characterize the indentation deformation process at the various levels of indentation depth from h = 0.5 to 3.0 μm. Figure 7.5 shows V' versus h for both the non-irradiated and the Zr^+ irradiated Zr-2.5%Nb material. For both conditions, V' increases with h and straight lines fitted to the data indicate that the non-irradiated data follow a stronger dependence upon indentation depth. The observation that V' is a function of h is similar to that reported previously for high purity copper [4].

Haasen plots are traditionally used to assess the operative plastic deformation mechanism in metals subjected to constant-uniaxial strain rate loading [24-27]. The Haasen plot is a graph of the experimentally determined inverse activation area, $1/\Delta a'$, versus the applied shear stress τ. Linear trends of $1/\Delta a'$ versus τ indicate that the plastic deformation in the test material occurs by a time-dependent obstacle-limited dislocation glide process (i.e. the Cottrell-Stokes law is maintained). Nonlinear trends in $1/\Delta a'$ versus τ can arise from the cumulative effect of several types of obstacles to dislocation glide or to a changing microstructural state within the deformed test material.

Figure 7.6 shows plots of $b^2/\Delta a'$ versus $\tau = \sigma_{ind}/3M$ for the data from the PSRC micro-indentation tests performed on the non-irradiated and the Zr^+ irradiated Zr-2.5%Nb material. The data from both material conditions result in linear trends with the slope of the non-irradiated sample being larger than that of the Zr^+ irradiated Zr-2.5%Nb sample. This indicates that the operative time-dependent deformation in both materials is an obstacle-limited dislocation glide process. The fact that the two conditions follow linear relationships with τ that are of different slope indicates that the strength of the obstacles that limit dislocation glide is different, and in fact larger, for the Zr^+ irradiated compared to the non-irradiated Zr-2.5%Nb material.

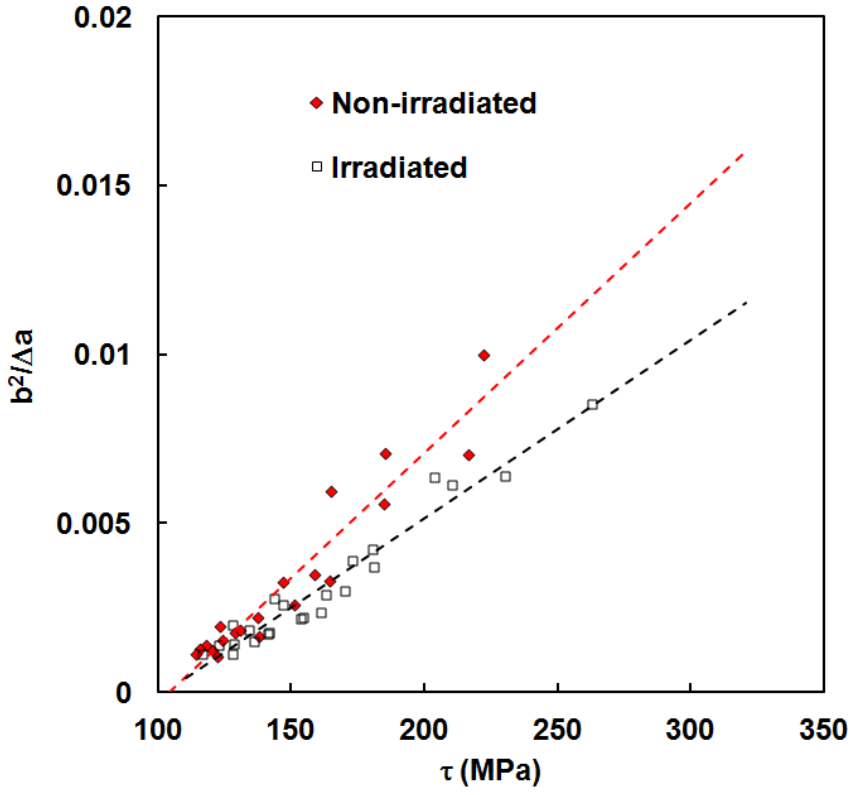

Figure 7.6: **Haasen plot of the inverse apparent activation area, normalized with respect to the square of the Burgers vector, $b^2/\Delta a$ versus the equivalent indentation shear stress $\tau = \sigma_{ind}/3M$ for the non-irradiated and the Zr^+ irradiated Zr-2.5%Nb material.**

7.3.3 Effect of indentation depth and Zr^+ irradiation on the strength of the obstacles that limited dislocation glide during micro-indentation of Zr-2.5%Nb

To quantify the strength of the obstacles that limit the rate of dislocation glide during the micro-indentation of the Zr-2.5%Nb material we calculate the apparent mechanical activation work $\Delta W'$ done by the applied stress in order for the dislocation to overcome the obstacles. The apparent activation work is expressed, using Eq. 7.2 and 7.8 as

$$\Delta W' = \tau V' = \tau kT \frac{\partial \ln \dot{\gamma}_{ind}}{\partial \tau} \tag{7.10}$$

Substituting $\tau = \sigma_{ind}/3M$ and $\dot{\gamma} = \dot{h}/h$ along with the fact that h remains essentially constant but $\dot{h}$ is reduced by a factor of ten during each strain rate change, Eq. 7.10 can be simplified and $\Delta W'$ can be expressed for each strain rate change as

$$\Delta W' = kT\left(\frac{\sigma_{ind}}{\Delta\sigma_{ind}}\right)\ln(10) \tag{7.11}$$

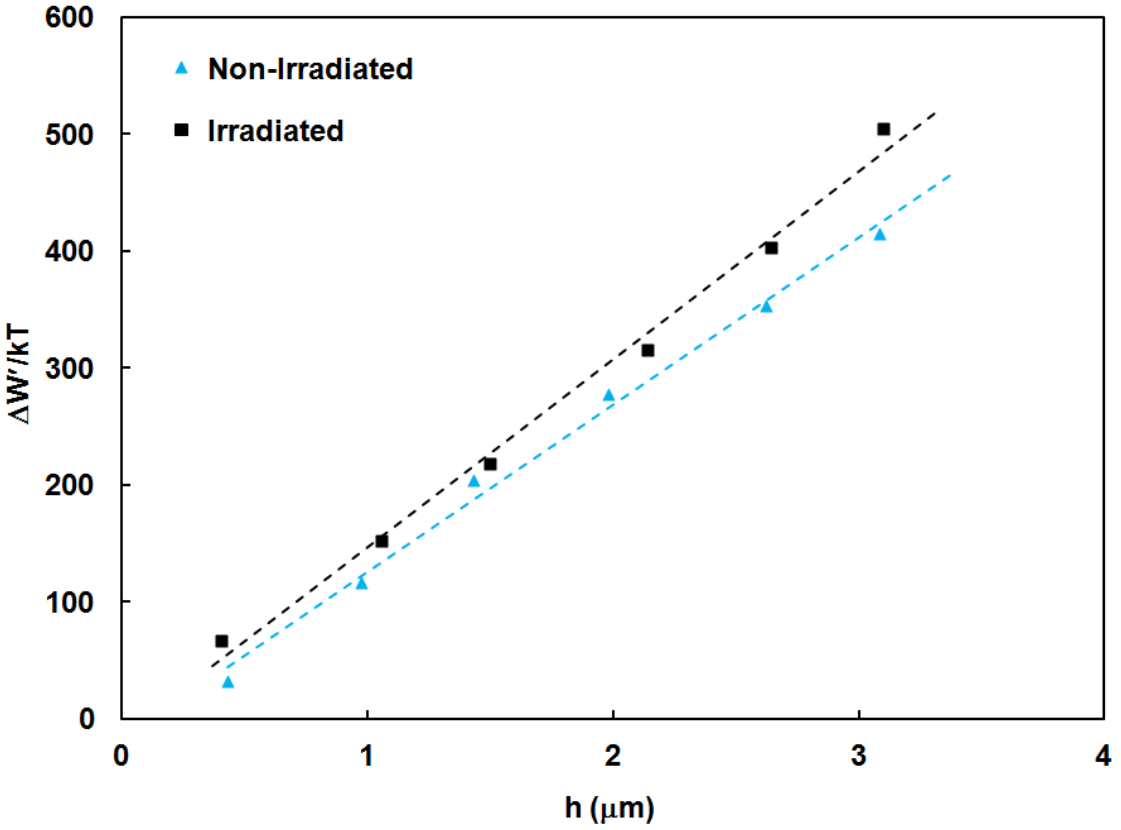

Figure 7.7: **Apparent activation work area $\Delta W'$, normalized with respect to *kT*, of the micro-indentation deformation process versus the indentation depth *h* for one indentation test, involving 6 indentation strain rate changes, on the non-irradiated and the Zr^{+} irradiated Zr-2.5%Nb material.**

Figure 7.7 shows the apparent activation work $\Delta W'$ plotted versus indentation depth h for the Zr-2.5%Nb material in both the non-irradiated and the Zr^+ irradiated conditions. One can clearly see that, for any indentation depth, Zr^+ ion irradiation increases the strength of the obstacles that limit the dislocation glide process in Zr-2.5%Nb.

7.4 Conclusions

Micro-indentation testing incorporating high precision strain rate changes (PSRC) were performed at 25^{o}C on the *RN* surface of non-irradiated and heavily Zr^+ irradiated Zr-2.5%Nb samples to assess the effect of ion irradiation induce crystal damage on the underlying mechanism of plastic deformation of this important nuclear material.

The tests indicate that the magnitude and strain rate sensitivity of the indentation stress, obtained under essentially constant microstructure conditions, increases when the indentation depth is decreased and, for a given indentation depth, increases with Zr^+ irradiation. The indentation stress increases with decreasing indentation depth in a way similar to the previously reported length scale dependence of the indentation stress of many materials [15-19] The data from the PSRC tests describe a linear dependence of the inverse of the apparent activation area versus applied stress (i.e. the Cottrell Stokes law is followed) which indicates that, for both material conditions, indentation deformation occurs by a time-dependent obstacle-limited dislocation glide process however the strength of the obstacles is affected by the Zr^+ irradiation.

In this study the apparent activation volume was measured from indentation strain rate changes that were performed under constant microstructure conditions. This allows us to calculate the apparent activation work of the deformation process as a function of indentation depth and Zr^+ irradiation. The calculated apparent activation work of the deformation process indicates that at any indentation depth the strength of the obstacles that limit dislocation glide during the micro-indentation of Zr-2.5%Nb increased with Zr^+ irradiation.

This study is, to the authors' knowledge, the first use of high precision, constant microstructure, strain rate change tests to characterized the strength of irradiation induced crystal defects in impeding the time-dependent dislocation glide in a zirconium alloy and lays the ground work for further studies of the effects of various levels of irradiation damage, and temperature on the apparent activation volume and activation work of the deformation of various materials that are used in nuclear reactors.

7.5 Acknowledgements

The authors wish to thank the Natural Science and Engineering Research Council of Canada (NSERC) and the University Network of Excellence in Nuclear Engineering (UNENE) who provided financial support for this research. The assistance of Professor B.J. Diak of Queen's University, Kingston, Ontario in designing and performing the research experiments is gratefully acknowledged. We offer a special note of thanks to Mr. B. Leitch of the Atomic Energy of Canada Ltd (Chalk River Laboratories) for providing the Zr-2.5%Nb pressure tube material used in this study.

7.6 References

[1] W.R. Newson, B.J. Diak, S. Saimoto, Thin Films: Stresses and Mechanical Properties VI, MRS Publications,Warrendale, PA, USA, v. 436 (1997), p. 359

[2] S. Saimoto, B.J. Diak, K.R. Upadhyaya, Mater. Sci. Eng. A, v. 234–236 (1997), p. 1015

[3] B.J. Diak, S. Saimoto, Mater. Sci. Eng. A, v. 319–321 (2001), p. 909

[4] R.J. Klassen, B.J. Diak, S. Saimoto, Mater. Sci. Eng. A, v. 387–389 (2004), p. 297

[5] B. Bose, R.J. Klassen, J. of Nucl. Mat., v. 399 (2010), p. 32

[6] B. Bose, R.J. Klassen, J. of Nucl. Mat., v. 405 (2010)**,** p. 138

[7] B. Bose, R.J. Klassen, MRS Proceedings, v. 1298 (2011)**,** p. 73

[8] B. Bose, R.J. Klassen, J. of Nucl. Mat., v. 419 (2011)**,** p. 235

[9] M. Carlone, S. Saimoto, Experimental Mechanics v. 36 (1996), p.360

[10] B.J. Diak, K.R. Upadhyaya, S. Saimoto, Prog. Mater. Sci., v. 43 (1998), p. 223

[11] U.F. Kocks, A.S. Argon, M.F. Ashby, Prog. Mat. Sci., v. 19 (1975), p. 1

[12] D. Tabor, Microindentation Techniques in Material Science and Engineering (edited by P.J. Blau and B. R. Lawn), ASTM special Publ. (1985), p. 129

[13] N. Christodoulou, S. St Lawrence, C.K. Chow, Transactions, SMiRT 19, Toronto, Paper # D03(August 2007), p.1

[14] N. Christodoulou, S.R. MacEwen, J.F. Mecke and O.T. Woo, Proc. of the 2nd Int. Symp. On Environmental Degradation of Materials in Nuclear Power Systems - Water Reactors, 1985, p. 515, Monterey, California.

[15] A. A. Elmustafa, D. S. Stone, J. Mech. Phys. Solids, v. 51 (2003), p. 357

[16] K.W. McElhaney, J.J. Vlassak,W.D. Nix, J. Mater. Res., v. 13 (1998), p. 1300

[17] V. Bhakhri and R. J. Klassen, Scripta Mater., v. 55 (2006), p. 395

[18] B. Bose and R. J. Klassen, Mat. Sci. and Eng. A., v. 500 (2009), p.164

[19] A. A. Elmustafa, J.A. Eastman, M.N. Rittner, J.R. Weertman, D. S. Stone, Scripta Mater., v. 43 (2000), p. 951

[20] M. Haghshenas, L. Wang, R.J. Klassen, Depth dependence and strain rate sensitivity of the indentation stress of the 6061 aluminum alloy, Materials Science and Technology, 2012, In press

[21] N. Christodoulou, P.A. Turner., E.T.C. Ho, C.K. Chow, M.R. Levi, Metall. and Mat. Trans. A., v. 31A (2000), p. 409

[22] A. Akhtar, J. of Nucl. Mat., v. 47 (1973), p. 79

[23] V. Ramachandran, R.E. Reed-Hill, Metall. Trans., v. 1(1970), p. 2105

[24] R.A. Mulford, Acta Metalurgica, v. 27(1979), p. 1115

[25] H. Mecking, U.F. Kocks, Acta Metallurgica v. 29(1981), p. 1865

[26] S. Siamoto, H. Sang, Acta Metallurgica, v. 31(1983), p. 1873

[27] W. Bochniak, Acta Metallurgica, v. 41(1993), p. 3133

Chapter 8

8 Conclusions and Future Scope

8.1 Conclusions

Zr-2.5%Nb CANDU pressure tubes have been much studied over the years yet, despite this, extensive experimentally-based knowledge on the mechanisms by which this material undergoes thermally-activated time-dependent "creep" deformation when in its in the non-irradiated and the neutron irradiated conditions has not been thoroughly studied. This dissertation has attempted to overcome this scarcity of data by providing a series of fundamental investigations involving the use of novel pyramidal micro-/nano-scale indentation test techniques to measure the anisotropic time-dependent plastic response of Zr-2.5%Nb CANDU pressure tube material in the non-irradiated and the Zr^+ irradiated conditions over the temperature range that is characteristic of the operating temperature window of a pressure tube in a CANDU nuclear reactor.

In the first study in this thesis (Chapter 3) pyramidal micro-indentation creep tests were performed at 25^{o}C on non-irradiated and Zr^+ irradiated Zr-2.5%Nb pressure tube material to simulate the low-temperature creep deformation around the scratches in CANDU reactor pressure tubes. The initial average indentation stress, $\sigma_{ind\,t=0}$ increased with decreasing indentation depth and increasing levels of Zr^+ irradiation. TEM images of the indentation plastic zone indicate that the Zr^+ irradiation induces uniform distribution of nanometer sized dislocation loops within the microstructure which is similar to what results from neutron irradiation. This indicates that Zr^+ irradiation is an effective way to simulate the crystallographic damage resulting from neutron irradiation in Zr-2.5%Nb. The activation energy ΔG_0 of the obstacles that limit the rate of dislocation glide during indentation creep did not change with indentation depth for the non-irradiated sample however ΔG_0 increased from 0.185 to 0.215 μb^3 with increasing levels of Zr^+ irradiation

damage and showed a non-linear relationship with the calculated displacements per atom resulting from the Zr^+ irradiation. The magnitude of the measured ΔG_0 was similar to what is expected for the activation energy of "intermediate strength" obstacles to dislocation glide such as dislocation/dislocation interactions. This suggests that the small dislocation loops produced in the irradiated samples become the rate-limiting obstacles controlling the low temperature creep around scratches in Zr-2.5%Nb pressure tube material.

In the subsequent investigation (Chapter 4) one-hour duration constant-load pyramidal indentation creep tests were performed to study the effect of Zr^+ irradiation on the anisotropy of the local plastic deformation of the Zr-2.5%Nb pressure tube material. All tests were performed at 25^{o}C on the radial-normal (RN), axial-normal (AN) and transverse normal (TN) planes of non-irradiated and Zr^+ irradiated material. The average indentation stress, $\sigma_{ind\,t=0}$ increased with decreasing indentation depth and, for any indentation depth, was larger for indentations made on the TN plane compared to those made on either the RN or AN planes. The indentation stress increased with increasing levels of Zr^+ irradiation and the amount of increase was highest for indentations made on the AN plane and lowest for indentations made on the TN plane of the pressure tube. The ratio of $\sigma_{ind_{t=0}}$ on the TN plane relative to $\sigma_{ind_{t=0}}$ on the AN and RN planes was 1.3 and 1.2 respectively before irradiation and decreased to 1.04 and 1.08 respectively after irradiation. This indicates that the anisotropy of the yield stress is decreased as a result of irradiation hardening. The relative change in indentation stress $\Delta\hat{\sigma}$, for any level of irradiation damage, decreased with increasing resolved fraction of basal poles in the indentation direction. This finding suggests that the ion irradiation damage has a greater effect on blocking the movement of dislocations on prismatic compared to pyramidal slip systems. Although the activation energy ΔG_0 did not change with indentation direction, it increased with increasing levels of Zr^+ irradiation damage. This reflects the effect that the crystallographic defects, such as small dislocation loops, that are formed by the Zr^+ irradiation have as obstacles to the dislocation glide process.

Chapter 5 provides a description of the findings related to the effect of Zr^+ irradiation performed at an elevated temperature of 300°C. The increase in the initial indentation stress $\sigma_{ind_{t=0}}$ with increasing levels of Zr^+ irradiation at 300°C was lower than that reported earlier in Chapters 3 and 4 for Zr^+ irradiation performed at 25°C. The ratio of $\sigma_{ind_{t=0}}$ on the TN plane relative to that on either the AN or RN planes decreased significantly with increasing Zr^+ ion irradiation confirming, once again, that the anisotropy of the indentation stress decreased with ion irradiation however the level of the decrease was less than when the Zr^+ irradiation was performed at 25°C. The relative change in indentation stress $\Delta\hat{\sigma}_{ind}$, for any level of irradiation damage, decreased with increasing resolved fraction of basal poles in the indentation direction indicating that, even at 300°C, Zr^+ irradiation has a greater effect on blocking the movement of dislocations on prismatic than on pyramidal slip systems. The apparent activation energy of the obstacles, ΔG_0, did not change with indentation direction but increased with increasing levels of Zr^+ ion damage with values lower than Zr^+ irradiation performed at 25°C. These observed differences in the indentation deformation of Zr-2.5%Nb samples irradiated with Zr^+ ions at 25°C and at 300°C can be attributed to the effect of concurrent thermal annealing on the accumulation of irradiation damage at 300°C.

Chapter 6 presents data on the effect of temperature on the micro-indentation stress and the activation energy for indentation creep performed on the AN, RN, and TN planes of the Zr-2.5%Nb pressure tube material over the temperature range from 25 to 400°C. At 25°C The ratio of the indentation stress in the transverse direction relative to that in the axial and radial directions was 1.29 and 1.26, which decreased to 1.22 and 1.05 at 400°C. This represents a difference in only about 3% at 25°C but approximately 11% and 26% at 300°C and 400°C and suggests that the flow stress in the radial direction follows different temperature dependence than that in the axial direction. The average activation energy ΔG_0 of obstacles that limit the rate of indentation creep increased from 0.72 to 1.33 eV with increasing temperature from 25 to 300°C. Over this temperature range ΔG_0 was not dependent upon the indentation direction and was similar in magnitude to equivalent data obtained from uniaxial tests performed on similar Zr alloys. At temperature greater than

300°C, ΔG_0 increase at a slower rate when tests were performed on TN plane than those performed on RN and AN planes. This suggests that the strength of the obstacles that limit the time-dependent glide of dislocations on the $\{10\bar{1}1\}\langle\bar{1}\,\bar{1}23\rangle$ pyramidal slip system changes between 300 and 400°C relative to the strength of obstacles limiting dislocation glide on the $\{10\bar{1}0\}\langle\bar{1}2\bar{1}0\rangle$ prismatic slip system.

The final investigation (Chapter 7) of this thesis was performed with micro-indentation testing incorporating high precision strain rate changes. The tests were performed at 25°C on the RN surface of non-irradiated and Zr^+ irradiated Zr-2.5%Nb samples to assess the effect of ion irradiation induced crystal damage on the plastic deformation mechanism under essentially constant microstructure conditions. The magnitude and the strain rate sensitivity of the indentation stress increased with decreasing indentation depth and, for a given indentation depth, increased with Zr^+ irradiation. The inverse of the apparent activation area showed a linear dependence on applied stress (i.e. the Cottrell Stokes law is followed) indicating that, for both material conditions, indentation deformation occurred by a thermally-activated time-dependent obstacle-limited dislocation glide process although the strength of the obstacles was affected by the Zr^+ irradiation. The apparent activation volume was measured from indentation strain rate changes that were performed under constant microstructure conditions. The calculated apparent activation work of the deformation process indicated that at any indentation depth the strength of the obstacles that limit dislocation glide during the micro-indentation of Zr-2.5%Nb increased with Zr^+ irradiation.

The findings presented in this thesis are novel and provide direct information on the plastic flow properties of the anisotropic Zr-2.5%Nb pressure tube material under high-magnitude multiaxial stress loadings both in the non-irradiated and the irradiated conditions and at temperatures in the range up to, and slightly beyond, the 250 to 300°C service temperature of CANDU pressure tubes.

8.2 Scope for Future Work

The findings of the investigations reported in this thesis open several avenues for future research. Some of these are described below.

In this research, Transmission Electron Microscopy (TEM) has only been used to observe, in a qualitative fashion, the deformation zone beneath the pyramidal indentation and the dislocation loops formed by the Zr^{+} irradiation. However, a detailed quantitative characterization of the dislocation structures, both deformation- and irradiation-induced, around the indentations under different temperature and irradiation conditions still needs to be done. One important result of such an analysis would be the assessment of the validity of the hypothesis, stated in this research and by others, that Zr^{+} irradiation induces similar crystallographic damage to Zr-2.5%Nb as neutron irradiation.

The findings, presented in this thesis, related to the indentation stress and deformation rate in the radial direction of the Zr-2.5%Nb pressure tube are new and have not been reported previously because of the scarcity of a suitable testing method. The data on the temperature dependence of the radial flow stress of the Zr-2.5%Nb pressure tube material suggests that it follows different temperature dependence than that in the axial direction. The actual reason for this type of behavior is still unknown. Further mechanical testing along the radial direction and microstructural characterization may be able to find a suitable answer.

The research presents in Chapter 7 represents the first use of the high precision, constant microstructure, strain rate change tests to characterize the effect of irradiation induced damage on the time-dependent dislocation glide in a Zr alloy. These tests were, however, only performed on the RN plane of the pressure tube and similar tests need to be performed on the TN and AN planes to completely characterize the mechanical anisotropy of the strain rate sensitivity of the indentation stress, the apparent activation volume and the activation work of the deformation process both in the non-irradiated and the Zr^{+} irradiated conditions. The high precision strain rate change method can also be applied to determine the effects of temperature on these deformation parameters of the Zr-2.5%Nb pressure tube material.

Curriculum Vitae

Name: Bipasha Bose

Post-secondary Education and Degrees:

The University of Western Ontario
London, Ontario, Canada
2005-2007 M.E.Sc. in Mechanical and Materials Engineering

Bangladesh University of Engineering & Technology (BUET)
Dhaka – 1000
Bangladesh
2000 – 2005 B.Sc. in Materials and Metallurgical Engineering

Honours and Awards:

Western Engineering Scholarship (WES)
2005-2012

Dean's Scholarship (BUET)
2001-2005

University (BUET) Merit Scholarship (For top ranking student)
2001-2005

Dhaka Education Board scholarship
1999-2005

Related Work Experience

Teaching Assistant
The University of Western Ontario
2005-2012

Research Assistant
The University of Western Ontario
2005-2012

Refereed Journal and Conference Publications:

1. B. Bose and R. J. Klassen, Temperature dependence of the anisotropic deformation of Zr-2.5%Nb pressure tube material during micro-indentation, Journal of Nuclear Materials, Volume 419, Issue 1-3 (2011), Pages 235–240

2. B. Bose and R. J. Klassen, Assessment of the Effect of Irradiation Temperature on the Mechanical Anisotropy of the Zr^{+} Ion Irradiated Zr-2.5%Nb, Materials Research Society Symposium Proceedings, Volume 1298 (2011), Pages 73-78

3. B. Bose and R. J. Klassen, Effect of Zr^{+} ion irradiation on the mechanical anisotropy of Zr-2.5%Nb pressure tube material, Journal of Nuclear Materials, Volume 405, Issue 2 (2010), Pages 138–143.

4. B. Bose and R. J. Klassen, Effect of irradiation hardening and indentation depth on the kinetics of micro-indentation deformation of Zr-2.5%Nb pressure tube material at 25^{o}C, Journal of Nuclear Materials, Volume 399, Issue 1 (2010), Pages 32-31

5. B. Bose and R. J. Klassen, Effect of copper addition and heat treatment on the depth dependence of the nanoindentation creep of aluminum at 300K, Materials Science and Engineering A, Volume 500 (2009), Pages 164-169

Conference Presentations:

1. B. Bose, R. J. Klassen, Effect of Ion-Irradiation on the Mechanical Anisotropy of Zr-2.5%Nb Pressure Tube Material at 25°C, Nuclear Materials 2010, October 2010, Karlsruhe, Germany

2. B. Bose, R. J. Klassen, Assessment of the Effect of Irradiation Temperature on the Mechanical Anisotropy of the Zr^{+} Ion Irradiated Zr-2.5%Nb, 2010 MRS Fall Meeting in Boston, MA, USA

3. B. Bose, R. J. Klassen, Effect of Ion-Irradiation on the Indentation Creep of Zr-2.5%Nb Pressure Tube Material at 298K, 22nd Canadian Materials Science Conference (CMSC), University of Waterloo, 2010

4. B. Bose, R. J. Klassen, Assessment of Local Plastic Deformation of Zr-2.5%Nb CANDU Pressure Tubes at 298K , 21st Canadian Materials Science Conference (CMSC), Queen's University, 2009

5. B. Bose, R. J. Klassen, Effect of Heat-Treatment on the Deformation Parameters of a 2024 Aluminum Alloy during Nanoindentation at 300K, 19th Canadian Materials Science Conference (CMSC), McMaster University, 2007

Poster Presentation:

Was a co-presenter of a poster titled "Scale dependent properties in polymeric nanomaterials" on "Research Day-2005" at the University of Western Ontario (UWO).